STUDY OF GREEN SOLID STATE LASERS BASED ON MGO:PPLN CRYSTALS FOR LASER DISPLAY APPLICATIONS

STUDY OF GREEN SOLID STATE LASERS BASED ON MGO:PPLN CRYSTALS FOR LASER DISPLAY APPLICATIONS

By YI GAN, B.Sc., M.A.Sc.

A Thesis Submitted to the School of Graduate Studies in Partial Fulfillment of the Requirement for the Degree Doctor of Philosophy

DOCTOR OF PHILOSOPHY (2012) McMaster University

(Engineering Physics) Hamilton, Ontario

TITLE: Study of Green Solid State Lasers based on MgO:PPLN crystals for Laser Display Applications

AUTHOR: Yi Gan,

B.Sc. (Huazhong University of Science and Technologies)

M.A.Sc. (McMaster University)

SUPERVISOR: Professor Chang-qing Xu

NUMBER OF PAGES: xv, 144

ABSTRACT

Laser-based displays have been under active development over the past 50 years. Visible lasers are considered as the “ultimate” light sources for display applications due to their high brightness, high directionality and high color saturation. Unlike commercially available red and blue laser diodes, semiconductor laser diodes that can directly emit green light with sufficient power and efficiency required in laser display are still not ready yet. Significant effort has been paid around the world to overcome this “green bottleneck”.

The aim of this thesis is to investigate a practical solution to build a compact green laser to satisfy the cost/performance requirement for laser display applications. Frequency doubling based on MgO doped periodically poled lithium niobate (MgO:PPLN) is the main research direction of this thesis work.

The thesis focuses on several engineering issues, mainly related to practical applications. Two different approaches have been explored: single-pass frequency doubling and intra-cavity frequency doubling. In the single-pass configuration, an all-fiber Q-switched fiber laser was used as the fundamental laser source because the high peak pump power can increase the conversion efficiency. 3.1%/W/cm nonlinear conversion efficiency was achieved which show good agreements with the theoretical

simulations. The single-pass frequency doubling of a novel annealing proton exchanged (APE) MgO:PPLN ridge waveguide was also investigated. Over 120 mW green laser with a 53.2% conversion efficiency was achieved. The results have shown remarkable improvements comparing with the reported waveguide devices.

On the other hand, in the intra-cavity frequency doubling, Nd:YVO_4/MgO:PPLN microchips for low power (300 mW CW green power and 530 mW modulated green power) applications have been demonstrated experimentally and investigated theoretically. It has been shown that although the plane-parallel cavity structure with discrete components can provide 2.9 W green laser with 29.6% conversion efficiency, it is complex for mass production. One of the important research achievements of this thesis is to study and optimization of a novel monolithically integrated Nd:YVO_4/MgO:PPLN module (namely mGreen module) which combines the advantages of the microchip structure and the discrete plane-parallel cavity structure. 1.28 Watt output green laser has been achieved through a compact configuration based on the optimized mGreen module. Power scaling based on this monolithic green laser module by employing an array concept has also been investigated. The dependence of output power on pump beam gap has been studied both theoretically and experimentally.

Acknowledgements

First, I would like to thank my supervisor, Dr. Chang-Qing Xu, who has offered me enormous support, great encouragement and expert guidance in various aspects throughout my M. A. Sc. and Ph. D. program. His patience, enthusiasm and dedication made my past six years in McMaster University a truly positive and enriching experience. I am fortunate to have him as my supervisor.

Two, special thanks to Dr. Adrian Howard Kitai and Dr. Ignacio Vargas-baca, who gave me a lot of remarkable academic suggestions on my research as my supervisory committee members in the last four years. I also wish to thank Dr Xijia Gu from Ryerson University for his endless support on fiber lasers and FBG research work.

Thanks all the professors in the Department of Engineering Physics for their valuable suggestions on my research work. Thanks Doris V. Stevanovic and Zhilin Peng from CEDT for their training courses about clean room and assistance in the clean room. Thanks also to Fran, Marilyn, Linda, Lori, Samantha, and Peter for all their help in the Engineering Physics office. I would like to express my sincere gratitude to all Engineering Physics members and McMaster staff that has helped me generously during the past four years. Without their help, this work does not exist.

Thanks Dr. Yang Lu, Dr. Jian Yang, and Dr. Qiang-yang Xu for their invaluable advice and discussions on my research topics. I am also appreciative to my colleagues, Jian Sun and Ben Watts. It's been great getting to know you, to learn from you and to work with you.

Last but not least, I would like to thank my parents and other family members for their lifelong encouragement and support. Also, my deep respect to my wife Lucy. Without her support, I would not have come this far.

Table of Contents

List of Figures

List of Tables

CHAPTER 1

INTRODUCTION

1.1 An Overview of Laser Displays

Display technologies have undergone three major advances in development: monochrome display, color display, and digital display [1]. Although every era has its own characteristics, the ultimate goal of display technology has remained static: to present a more real world to people. Experts disagree on exactly what the next generation of display technology will be, but most of them agree that higher resolution and richer color are the two important directions in which technology is moving. Although current technologies can provide a high enough resolution that the human eye is unable to notice pixilation at a typical viewing distance (e.g. the "Retina Display" from Apple [2]), there is great potential to improve in color performance. Thus, laser display is a competitive candidate for the next generation of display technologies.

Since the invention of the first Ruby lasers, color laser display has been a dream of laser societies [3]. Due to the unique optical characteristics they process, visible lasers are generally considered as "ultimate" light sources for display applications.

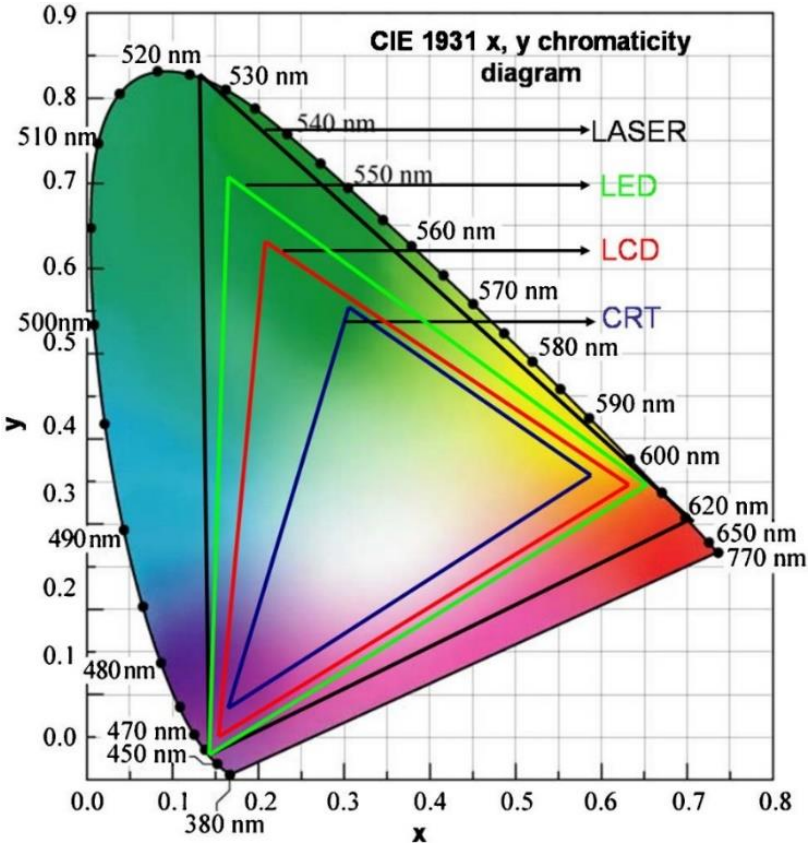

Figure 1.1. Color gamut of different display technologies [4].

Lasers have been attractive to display applications because, from both a theoretical and a practical standpoint, they deliver a significantly better image than any other display technologies. An immediate advantage of lasers is their ability to cover a wide range of color, due to their narrow spectral bandwidth and addressable wavelengths. Based on the most widely used scientific definition of color, the Commission International de l'Eclairage (CIE) color space, the color gamut of different display technologies can be quantified and measured by instrumentation [5]. As shown in Figure 1.1, the cathode ray tube (CRT) display gamut only covers 70% of the National Television Systems

Committee (NTSC) color gamut because of the limited spectral purity of phosphor emissions. In contrast, the use of red-green-blue (RGB) laser sources enables coverage of 120% of the NTSC gamut, which means that laser displays can provide far more life-like images than any other existing technology.

Another benefit of laser sources is their very low intrinsic étendue. The étendue of a light source is determined by the product of the emitting surface and the solid angle of the light emission [6]. A TEM_{00} laser can be seen as a true point source; all light appears to emanate from the same point in space. In contrast, a lamp or light-emitting diode (LED) emits from an extended area or volume over a large solid angle. Thus, lasers have a very small étendue in comparison to other light sources. The performances of today's projection systems are limited by the Law of Étendue: in a perfect optical system, étendue may be conserved, but may never be reduced without the loss of light. Only part of the light from the source that fits inside the étendue of the light valve may be used [7]. Thus, by using low étendue light sources, such as lasers, one can produce images with less complex, more efficient, smaller, and more powerful optical systems.

The limited lifetime of lamps has a serious impact on a system's cost of ownership, and places the reliability/lifetime of light sources on the list of priorities for future development. Compared with the ~5,000-hour lifetime of lamps, lasers offer lifetimes in the order of tens of thousands of hours (usually around 20,000) [8]. Moreover, lasers maintain the same emission wavelength over their entire lifetime which means they can provide an image that never changes with time.

1.2 The Development of Compact Green Lasers

Although the idea of using lasers for display applications was proposed in the 1960s, it is only recently that laser display systems have been developed. This is primarily due to the recent availability of lasers emitting red, blue, and green colors [9]. Traditional gas- and dye-based visible lasers are not suitable for mass production due to their large size, inefficiency, and maintenance difficulty [10]. The invention of semiconductor laser diodes (LDs) has enabled the laser to be shrunk down to a microelectronics scale, making the mass-production of these lasers more tractable [11]. They are an obvious first choice for building commercial laser display systems, due to their compact and low-cost features. Red LDs based on aluminum indium gallium phosphide (AlGaInP), which emit around 635 nm, have been well developed [12 – 14]. In addition, the introduction of powerful blue LDs based on gallium nitride (GaN) are becoming more common since their first demonstration in 1995 [15, 16]. The present wall-plug efficiency (WPE) values of red and blue LDs are not very far from their theoretical maximum. In contrast to red and blue LDs, semiconductor chips that directly emit green light with sufficient power and efficiency are not currently available on the market. Recently, a significant research effort has been conducted to overcome this “green bottleneck”.

1.2.1 Direct-emitting Semiconductor Laser Diodes

A semiconductor laser diode normally uses inter-band transitions within active layers which are often quantum wells (QWs) inside a semiconductor heterostructure. The

materials useful for constructing semiconductor LDs have been widely investigated since the 1960s [16, 17]. A high quality semiconductor material with a bandgap corresponding to the energy of around 2.34 eV is required for green lasing [18]. Thus, group-III nitrides are a promising candidate.

The first GaN-based LD was demonstrated by Nichia Corporation in 1995 [15]. The lasing wavelength was approximately 400 nm. Since then, the performance of blue LDs has been steadily improved by Nichia, and the lasing wavelength has been increased to ~450 nm [19, 20]. Although violet and blue LDs are now commercially available, the lasing wavelength of GaN LDs did not reach 500 nm until 2009.

There are several technical challenges involved in developing green laser diodes. First, shifting the lasing wavelength towards green involves reducing the active region material bandgap. This is accomplished by increasing the indium concentration in the QWs. However, material growth by the metal organic chemical vapor deposition (MOCVD) is challenging due to the high level of stress caused by the high molar fraction of indium needed. The second challenge is substrate choice. GaN single-crystals is an ideal substrate, however, the growth of GaN crystals is expensive. Moreover, attaining a high concentration p-doping in the GaN material is difficult [21].

The research and development of green laser diodes is rapidly progressing. Many groups (Nichia, Osram, Sumitomo, Corning, Soraa, and UCSB) have been racing in developing practical green lasers for display applications since 2009 [22 – 32]. Further studies on potential materials and growth technology for In-rich GaN QWs should continue to achieve high-power commercial green LDs.

1.2.2 Green Lasers based on Nonlinear Frequency Conversion

Traditional solid-state laser materials do not fit the wavelength range of blue-green light generation. An alternative - nonlinear optical technology - gives an indirect method of obtaining wavelengths that are not within the range of solid-state lasers. The first nonlinear optical phenomenon, namely, second harmonic generation (SHG) or frequency doubling through crystalline quartz, was first observed by Franken in 1961 soon after the invention of laser [33]. However, due to the second or higher-order nonlinear effect, the optical frequency conversion efficiency is relatively low. Inserting a nonlinear optical crystal into the laser cavity is a highly efficient frequency conversion method in comparison to the single-pass frequency conversion [34].

1.2.2.1 Single-pass SHG

As shown in Fig 1.2, a single-pass configuration may be the simplest approach to generate green light using nonlinear frequency conversion. Using this method, the beam emitted by an infrared laser is focused directly into a suitable nonlinear crystal so that a green laser is produced by SHG in single pass.

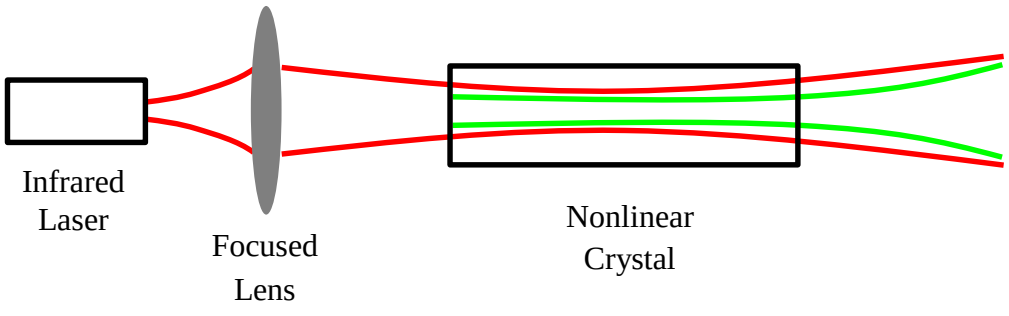

Figure 1.2. Schematic of single-pass SHG configuration.

In principle, semiconductor LDs would be the ideal infrared source for the single-pass arrangement, since they are compact, strong, and reliable. For an efficient single-pass SHG with bulk nonlinear crystals, high power and high brightness semiconductor LDs are required. Traditional index-guided narrow-stripe LDs have been found to be unsuitable because their output power is restricted by facet damage to several hundred milliwatts. On the other hand, broad-area LDs can emit infrared lasers to the order of several watts, but their poor spatial and spectral mode characteristics lead to inefficient frequency conversion. The most practical method is to use an abroad-area LD as an amplifier to boost the power of a low output power LD with a stable, single-frequency spectrum, and a good spatial mode, as shown in Figure 1.3. Testing with this configuration, called a master oscillator power amplifier (MOPA), as the pump source for single-pass SHG, has been under active development in recent years. Using a 30 mm long MgO:PPLN crystal, a green output power of up to 1.5 W was achieved with a fundamental infrared power of 7 W [35].

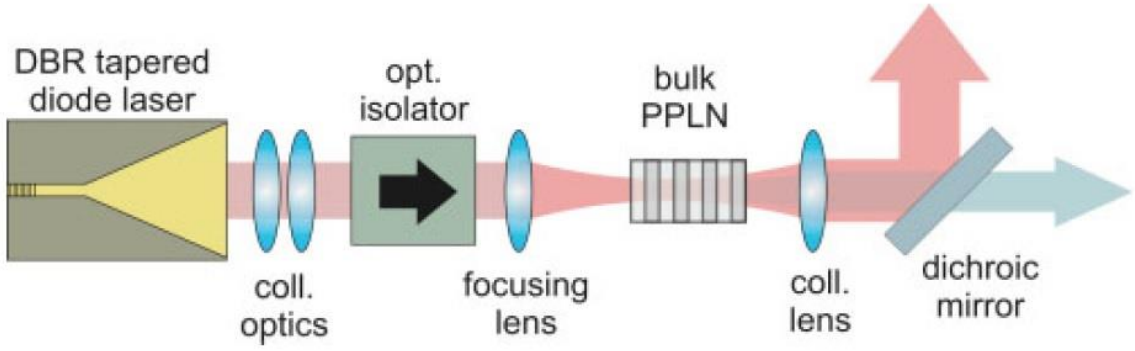

Figure 1.3. Single-pass SHG configuration of MOPA [35].

Diode-pumped solid-state lasers and fiber lasers are also frequently used as the infrared source for single-pass SHG. The first reported CW green light generation via the single-pass frequency doubling method was reported by Milller *et al.*. The authors reported a power of 2.7 W at 532 nm and a 42% conversion efficiency [36]. Kontur *et al.* also reported that high powers (1.7 W) can be obtained in PPKTP through the single-pass arrangement [37]. Most recently, Goutam *et al.* achieved a 13 W green laser output based on the simple single-pass SHG of a CW Yb-fiber laser with a conversion efficiency up to 55% [38].

1.2.2.2 Guided-wave SHG

In the single-pass SHG based on bulk nonlinear crystals, the Law of Diffraction forces a compromise between two necessary conditions for efficient conversion: a small spot size and a long interaction length. A loose focus yields a long interaction length but a low power intensity, while a small spot cannot be maintained over a long distance due to diffraction. In contrast, a waveguide structure can overcome the tendency of diffraction of a tightly-confined wave, so that high intensity may be maintained over the entire length of the nonlinear medium.

The most significant results have been obtained using Quasi Phase Matching (QPM) in periodically poled ferroelectric materials. This success is likely due to the absence of the walk-off effect. Planar waveguide SHG devices are attractive to couple with the MOPA lasers because both of them confine beams in a one-dimensional manner. Many QPM planar waveguides are fabricated by the proton exchange, ion implantation,

and direct bonding methods [39 – 43]. A record-high SHG power from a planar waveguide was achieved by Sakai *et al.* from Mitsubishi [44]. These authors demonstrated a green-light laser with a power of 1.6 W and a conversion efficiency of 40%. This was accomplished using a 7 mm long MgO:PPLN and a 1.2 W SHG with 60% efficiency using an 18 mm long sample. Compared with the planer waveguide structure, a buried channel or a ridge waveguide structure can provide a stronger light confinement. Despite of this, traditional buried channel waveguides suffers from photorefractive damage and weak light confinement. In the past few years, an alternative - ridge nonlinear waveguides - have been extensively studied. Due to the properties of ferroelectric materials, dry etching and wet etching techniques are not suitable for fabricating waveguide [45 – 47]. A practical solution to this problem is precisely-machined ridge waveguides. The Corning Green Laser G-1000 modules uses a distributed Bragg reflector (DFB) laser, which operates at 1060 nm followed by frequency doubling in a MgO:PPLN ridge waveguide (see Figure 1.4). Both a 222 mW SHG power laser with a 58% conversion efficiency, and a 304 mW output power laser with a 72.9% conversion efficiency have been reached using MgO:PPLN ridge waveguides [48, 49].

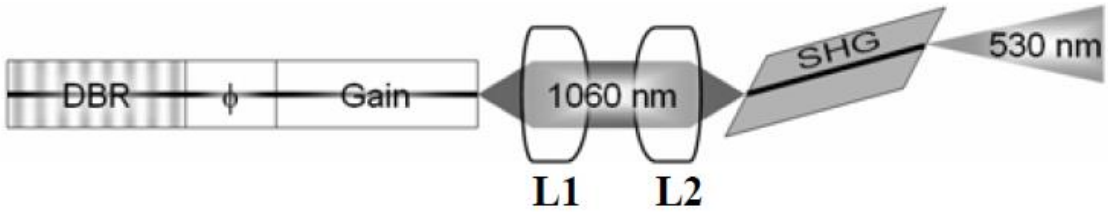

Figure 1.4. Operation of the G-1000 laser from Corning [49].

1.2.2.3 Intra-cavity SHG

When examining the basic theory of lasers, one quickly observes that the intra-cavity power density is much higher than the output power. Since the SHG conversion efficiency relies on the fundamental pump power density, it would be logical for one to ask: "Why not place a nonlinear crystal ***inside*** a laser cavity to achieve a higher conversion efficiency?" Indeed, inclusion of the nonlinear crystal within the resonator of an infrared laser is the basic idea behind intra-cavity SHG. The research on intra-cavity frequency doubling can be catalogued by the type of infrared pumping lasers, and is detailed below.

Diode-pumped Solid State Lasers (DPSSLs)

Intra-cavity frequency doubling of solid state lasers has been pursued since the mid – 1960s. Rare earth doped solid state lasers emitting at 1064 nm, such as Nd:YAG and Nd:YVO_4, have been investigated widely for green light generation based on intra-cavity SHG. Frequency doubling crystals, such as KTP, LBO, and PPLN have also been studied extensively. Currently, the major challenge associated with using green DPSS lasers in display systems is the size and cost of doing so. The green light source in Mitsubishi's laser television is a 15-emitter array of lasers emitting frequency doubled 532 nm light. The air-cooled module, with a volume of 5 cc, can generate about 3.8 W of green light [50]. Panasonic also demonstrated a 1 W 532 nm green laser with a volume of only 2 cc [51].

Vertical-cavity Surface-emitting Lasers (VCSELs)

First demonstrated by Soda *et al.* in 1979, VCSELs use a vertical-cavity surface-emitting structure to provide better beam quality than edge-emitting LDs do [52]. Another advantage of VCSELs is that, unlike edge-emitting LDs, they can be fabricated as monolithic arrays. In their early development, the output power of VCSELs was limited. But after many years of development, they can now provide enough power for display applications.

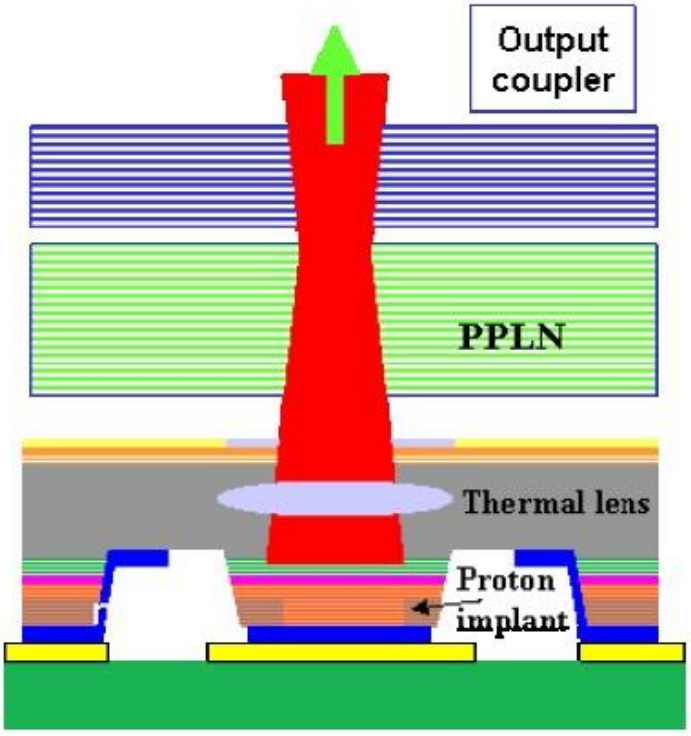

Figure 1.5. A schematic diagram of the Necsel structure [53].

Novalux has developed a high power green laser array of extended cavity surface-emitting lasers, which is called the Novalux Extended Cavity Surface-Emitting Laser (Necsel) [54]. As shown in Figure 1.5, Necsel uses intra-cavity frequency doubling of infrared light from VCSELs with an InGaAs active region to produce visible light at 532 nm. The cavity is stabilized by a thermal lens or by an intra-cavity lens to form a simple, semi-confocal cavity with the SHG crystal inside the resonator. A glass volume Bragg grating (VBG) is used to control the operating wavelength. Each single emitter can generate a power of around 100 mW. The biggest advantage of Necsel, claimed by Novalux, is that it can be mass produced at a low cost. This is because all components can be wafer produced and fully tested at the wafer level.

Optically-pumped Semiconductor Lasers (OPSLs)

The third configuration of green lasers is based on the intra-cavity SHG of OPSLs, as shown in Figure 1.6. This concept combines the merits of solid-state lasers and semiconductor lasers, by using a bulk semiconductor quantum well as a gain medium, in combination with a solid-state laser cavity. This class of lasers can deliver high optical power with good beam quality. More than 8 W of optical power was produced at 1000 nm with an M^2 value of <1.8 by Lutgen *et al.* [55]. Specially designed periodically resonant gain (PRG) results in an extremely high absorption of the pump light with a micron-thick gain region. The quantum well structure of the PRG absorbs the pump light with a rather large wavelength tolerance while the bulk cavity structure functions similar to traditional solid-state lasers.

Today, intra-cavity frequency doubling of OPSLs has developed lasers that demonstrate up to 13 W in blue (using LBO), 7 W in green (using BBO), and 5 W in yellow (using LBO) [56 – 58]. Osram leveraged the optical pumping concept to produce efficient and compact green lasers with powers of up to 50mW [59]. Another examples is the Genesis series of high-power lasers from Coherent, Incorporated, which uses OPSL technology to produce wavelengths of 639 nm, 532 nm, 577 nm, 480 nm, and 460nm with power levels ranging from 500 to 8000 mW [60, 61]. Disadvantages of OPSL structures include a critical PRG design and growth, a very high DBR mirror reflectivity growth, and heat dissipation in the active region under high power operation.

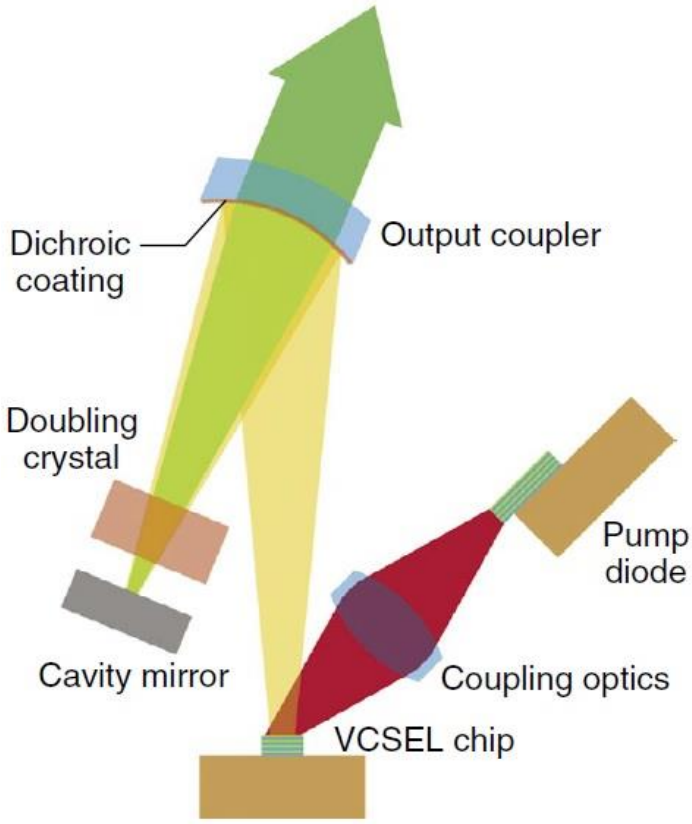

Figure 1.6. A schematic diagram of an OPS laser structure [61].

1.3 Lithium Niobate

Due to the emerging demands of wavelength conversion devices in many science and engineering fields, many nonlinear optical crystals that can be used to obtain high efficient conversion, such as Lithium Niobate ($LiNbO_3$), Beta Barium Borate (Beta-BaB_2O_4 / BBO), Potassium Titanium Oxide Phosphate ($KTiOPO_4$/KTP), Lithium Triborate (LiB_3O_5/LBO), Potassium Dihydrogen Phosphate (KDP), and Lithium Tantalate ($LiTaO_3$), have been developed [62]. Among them, $LiNbO_3$, often referred to as 'the silicon of nonlinear optics', is one of the most versatile and well-developed nonlinear optical materials. The basic material properties of $LiNbO_3$ are promising for practical applications. Lithium niobate, which is not present in nature, is grown in the laboratory in large crystals through low cost techniques. This culturing method has resulted in a volume of over 100 tons per year. In other words, this is a non-expensive starting material for devices.

Lithium niobate is a solid crystalline material, which is stable at room temperature and is also stable to environmental fluctuations, including humidity. Single crystals of this material were first fabricated using the Czochralski technique (i.e. pulling from the melt) by Remeika in 1965 [63]. To date, the crystal growth industry provides homogeneous crystals of several kilograms and three or four inches in diameter each. Table 1.1 shows a summary of the main properties of lithium niobate crystals.

Table 1.1. A properties summary of lithium niobate crystal [64, 65].

General Properties:	
melting point:	1260 ℃
crystal symmetry:	trigonal, point group 3m
hardness	5 Mohs
stoichiometry	nonstoichiometric, ~6% Li deficiency easy to dope in high concentration
ferroelectricity	Curie temperature T_C = 1150 ℃ Spontaneous polarization $P_S(RT) \sim 96\ C/m^2$ 180 °domains
Optical related properties:	
transparency region	VIS/NIR (~350 nm to ~5 μm)
optical anisotropy	uniaxial, c-axis
refractive indices	$n_o = 2.286$, $n_e = 2.203$ (632.8 nm)
optical homogeneity	
optical effects	acousto-optic, electro-optic second order nonlinearity bulk photovoltaic effect photorefractive effect

Lithium niobate is a ferroelectric material with a very high Curie temperature. The combination of excellent electro-optical, acoustic-optical and non-linear optical properties makes $LiNbO_3$ an attractive host material for various useful applications. It is used mostly in radio frequency surface acoustic wave filters due to its large piezoelectric coefficient. The electro-optic effect, with a moderately high coefficient, is a very useful property when manufacturing high-speed digital modulators for telecommunication systems. This pure material is transparent from a band-gap edge absorption of about 320 nm (~3.9 eV) up to the infrared vibrational absorptions at a wavelength of about 5 μm (0.25 eV) [65]. The material also provides low loss of all UV, as well as visible and mid-infrared light propagating, which are both very important for photonic applications.

It is well known that only those crystals without the inversion symmetry in their crystal structures possess the second-order nonlinearity. The crystalline structure of this material at room temperature corresponds to the trigonal 3m point group. The crystal is optically uniaxial, with two refractive indices: ordinary and extraordinary. Both indices have values greater than 2.0 over the entire transparency window, which often makes it necessary to fit antireflection coating layers on the optical surfaces in many cases. As with most of niobium oxides, lithium niobate belongs to the ferroelectrics. In the high temperature (para-electric) phase, the crystal has inversion symmetry. When the crystal is cooled below the phase transition temperature, or Curie temperature, it undergoes a phase transition to the ferro-electric phase. Consequently, no further phase transition occurs below the Curie temperature, and there is no structural mismatch between neighbouring domains. As shown in Figure 1.7, in the lithium niobate crystal structure, the oxygen

planes are represented by lines with the cations between the plans. The cations are displaced from the center position, defining the direction of the polar Z-axis. The phase transition is caused by the different displacement of the cations. Thus, a uniform crystal with a spontaneous polarization pointing to the same direction can be achieved by a poling step after growth. An electric field is applied while the crystal is cooled through the Curie temperature. At that point, the developed spontaneous polarization aligns itself along the polarization induced by the applied field, resulting in a single-domain crystal. Within a domain, all of the cations are displaced in unison in one direction, giving rise to a spontaneous polarization (at no applied field) in that direction. This property makes lithium niobate crystals suitable for fabrication of domain inversion gratings.

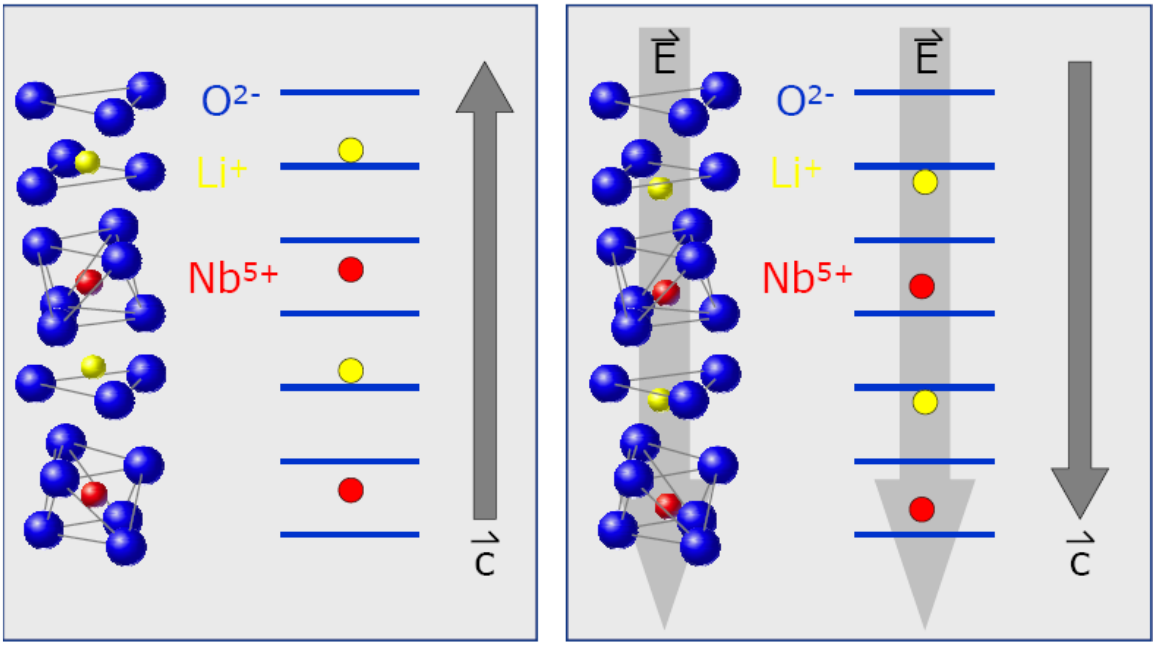

Figure 1.7. Atomic lattice structure of lithium niobate [66].

1.4 Research Motivation and Objective

In order to make laser displays commercially successful, green lasers must be made with sufficient power, compact in size, and low-cost. As is seen from the review in the above sections, none of existing green laser technologies are satisfactory at fulfilling all of these demands for laser display applications simultaneously. It is therefore of great interest to explore new practical solutions that improve the quality and simplicity of green laser technology.

The objective of this thesis is to investigate practical solutions for building a compact green laser that satisfies the cost/performance requirement for laser display applications. Frequency doubling based on MgO doped periodically poled lithium niobate (MgO:PPLN) is the main research direction of this thesis work.

1.5 Thesis Outline

This thesis is organized into five chapters. The first chapter provides a brief introduction into laser display and the development of green lasers, including the current state of technology. The introduction also describes the motivation and objective of this research in the context of the history of laser technology.

Starting from the Maxwell equations, Chapter Two provides a general introduction to the theoretical background of nonlinear frequency conversion. Moreover, a numerical model is provided in Chapter Two in order to simulate and optimize the intra-cavity

frequency doubling configuration design. This chapter also details the thermal effect analysis.

Chapter Three describes the single-pass experiments conducted for this thesis based on two major experimental schemes. First, a Q-switched fiber laser is used as the pump source to improve conversion efficiency, due to the high peak pump power that this approach allows. Second, a MgO:PPLN waveguide is investigated for use as the wavelength conversion device.

Chapter Four emphasizes intra-cavity frequency doubling technique used in this thesis to build compact low-cost green lasers. Nd:YVO_4/MgO:PPLN microchips are first investigated for their application in generating several hundred mW green power outputs. Plane-parallel cavity structures intra-cavity frequency doubled DPSS lasers are also constructed in order to generate Watt-level green lasers. Then, a novel monolithic Nd:YVO_4/MgO:PPLN integrated module which combined the advantages of the microchip and the separated plane-parallel cavity is introduced and optimized for Watt-level applications. Power scaling based on this monolithic green laser module through the employment of an array concept is also investigated.

Chapter Five concludes with a summary of the most important achievements of this research, as well as suggestions for future work.

CHAPTER 2

THEORETICAL BACKGROUND

2.1 Introduction

This chapter provides a basic theoretical background for the green laser generation. We first described the basic information of diode-pumped solid-state lasers, which are used as the fundamental 1064 nm laser sources for green light generation. Then, the basic theory of nonlinear optical interaction is reviewed, including the concept of quasi-phase matching (QPM) in ferroelectric materials, single-pass second harmonic generation (SHG), and intra-cavity frequency doubling.

2.2 Diode-Pumped Solid-State Lasers

Diode-pumped solid-state lasers have made rapid progress since 1990 [67, 68]. Thanks to development of pump laser diodes, pumping efficiency is improved several times higher and generated heat is much less than the lamp-pumped solid-state lasers. Moreover, with the development of pumping configurations and pump beam reshaping, laser diodes now can emit specific pump wavelength with specific beam modes. These advantages pushes extensive applications of solid state lasers in industry, biomedicine and military fields.

A laser oscillator is composed of three basic parts: a laser crystal, a pumping unit and an optical resonator [69]. To generate green laser at 532 nm by frequency doubling, we here consider a neodymium (Nd) doped bulk laser crystal pumped by laser diodes. A traditional optical resonator in a DPSS laser may be composed of either standing-wave linear cavity, a traveling-wave linear cavity or a traveling-wave ring cavity. In this work, in order to build a compact and low cost green laser, we just consider a simple standing wave linear cavity, which is composed of two plane mirrors, also called Fabry-Perot resonator, including intra-cavity frequency doubling.

2.2.1 *Laser Crystals*

The most popular solid-state lasers are lasers based on rare-earth-doped crystals or glasses. In most cases, these trivalent (have a triple positive charge) rare earth ions replace other ions of similar size and same valence in the host medium. A common property of these trivalent rare earth ions is that their electronic transitions usually occur within the 4f shell, which is shielded from the host lattice by the optically passive outer electronic shells. Different rare earth ions have different emission line. Table 2.1 shows the most frequently used rare earth ions and host material together with typical emission wavelength ranges [70].

To achieve green laser at 532 nm by frequency doubling, fundamental lasers emit at 1064 nm is required. For trivalent Nd, the transition from the $^4F_{3/2}$ upper energy level to the $^4I_{11/2}$ lower energy level is the main stimulated emission at 1064 nm. The strongest pump absorption wavelength is centered at 808 nm. Since the lower energy level $^4I_{11/2}$ is

above the ground state, the threshold condition can be easily obtained with relatively low pump rate in this four-level system.

Table 2.1. Common rare earth ions, host material and typical emission wavelength

Rare earth ion	Host material	Emission wavelength
neodymium (Nd^{3+})	YAG, YVO_4, YLF, silica	1.03–1.1 μm 0.9–0.95 μm 1.32–1.35 μm
ytterbium (Yb^{3+})	YAG, tungstate, silica	1.0–1.1 μm
erbium (Er^{3+})	YAG, silica	1.5–1.6 μm 2.7 μm, 0.55 μm
thulium (Tm^{3+})	YAG, silica, fluoride glasses	1.7–2.1 μm 1.45–1.53 μm 0.48 μm, 0.8 μm
holmium (Ho^{3+})	YAG, YLF, silica	2.1 μm, 2.8–2.9 μm
praseodymium (Pr^{3+})	silica, fluoride glasses	1.3 μm, 0.635 μm 0.6 μm, 0.52 μm 0.49 μm
cerium (Ce^{3+})	YLF, LiCAF, LiLuF, LiSAF, and similar fluoride	0.28–0.33 μm

There is a wide range of crystalline material which can be used as host media. Frequently used crystal materials are certain oxide (YAG), vanadate (YVO_4, $GdVO_4$), tungstate (KGW, KYW), fluoride (YLF, CaF). For Nd-doped crystals, yttrium aluminum garnet (YAG) is the most commonly used in DPSS lasers in industrial fields. YAG is chemically stable, has good thermal and mechanical properties, and has an isotropic structure. These properties make Nd:YAG the most versatile solid-state laser crystal [71, 72].

Nd-doped yttrium vanadate (Nd:YVO_4) is another promising material for DPSS lasers. It has several advantages over Nd:YAG including a higher gain cross-section, lower threshold, a wider Nd absorption peak and polarized output [73]. The absorption coefficient of Nd:YVO_4 crystal is five times higher than that of Nd:YAG crystal with the same dopant concentration at a pump wavelength of 808 nm. The high absorption coefficient makes it easy to obtain TEM_{00} mode operation by using a short cavity with high slope efficiency. The wider Nd absorption peak means that the laser output power is less sensitive to any drift of pump wavelength. Polarized output is extremely important for many applications such as nonlinear frequency conversion. With Nd:YVO_4 laser crystal, the cavity design is hence simplified for maintaining a polarized beam inside the cavity. Moreover, the polarized output has the advantage that it can avoid thermally induced birefringence. However, Nd:YVO_4 crystals are not suitable for high power because their thermal conductivity is much lower than that of Nd:YAG crystals. Thus, at high power operation, a large amount of thermal energy converted from absorbed pump power is accumulated near the pump region and the high absorption coefficient also

results in a large temperature gradient. Consequently, a large amount of stress produced at the pump end of the crystal. Theoretical and experimental studies show that the maximum laser output power for end-pumped solid state lasers is limited by thermal fracture of laser crystals. Another shortcoming is low fluorescence lifetime (100 μs), which renders it unsuitable for pulsed lasers. In summary, we can see that for compact DPSS lasers with several watts laser output power, Nd:YVO_4 is actually a good choice [74, 75].

Ytterbium (Yb) -doped gain media is another candidate for 1 micron near infrared laser emission. The most common Yb-doped lasers are fiber lasers, which are a special kind of solid-state lasers [76] . Fiber lasers have a high potential for high average output power, high power efficiency, high beam quality, and broad wavelength tunablity. Frequency doubling configurations based on Yb-doped fiber lasers are investigated in next Chapter.

2.2.2 *Pumping Scheme*

In most DPSS laser configurations, two kinds of pumping schemes are used: end pumping (axial) and side pumping (lateral). The pumping light can be transmitted directly from diodes to a laser crystal through reshaping optics or delivered through a fiber. Applying a laser diode or diode array as a pump source in a DPSS laser, one needs to consider wavelength, absorption coefficient, spot size, beam divergence, and incident angle of pump beam.

The goal of end pumping geometry is to couple as much of the pumping power as possible into the fundamental mode volume of the cavity. End-pumped DPSS lasers offer

highly efficient energy extraction form the gain medium due to good spatial overlap between pump beam and lasing beam [77]. This is not only for producing high quality output beam, but also leads to the most efficient harmonic conversion, such as green and UV light generation. In contrast, the aim of side pumping is simply to efficiently couple as much power as possible into the laser with low cost (laser diodes suitable for end pumping are twice as expensive as diode arrays at same output power). State-of-the-art end-pumped DPSS lasers can provide power up to tens of watts, while side-pumped DPSS lasers offer raw power as high as several kilowatts. In consideration of polarized pump for Nd:YVO_4 and better overlap with intra-cavity Gaussian beam, the end-pumping method is the best choice for developing compact and low cost green DPSS lasers.

2.2.3 *Resonator*

A laser resonator oscillates in an eigen mode, which is the transverse intensity distribution that occurs when a roundtrip through the cavity ends with the same distribution with which it stated except for various amplitude losses, such as diffraction loss, reflection loss, and scattering loss [78]. To analyze an optical resonator, we should start from a passive resonator, in which the distribution of electromagnetic (EM) field amplitudes and phases reproduce themselves upon repeated reflections between the two mirrors. In most lasers, either a stable or unstable cavity is employed with a single-mode or multi-mode output.

A large amount of research has been devoted to the design of optical resonators that can maximize energy extraction from the active material while producing a diffraction-

limited beam or a low-order mode beam. The following general criteria can be established for the design of an efficient and practical laser system with a high-quality output beam:

- The TEM_{00} lasing mode should be confined in the gain medium;
- The resonator should be dynamically stable, i.e., insensitive to pump-induced fluctuation of the rod focal length;
- The resonator modes should be fairly insensitive to mechanical misalignment.

Most commonly used laser resonators are composed of two spherical or flat mirrors facing each other. In order to eliminate the diffraction losses caused by aperture effect, the mirror sizes and crystal apertures should be large enough compared to the oscillated beam diameter. Moreover, in consideration of intra-cavity nonlinear frequency conversion, a small diameter TEM_{00} mode is preferred since nonlinear conversion efficiency is approximately proportional to fundamental beam intensity. However, a laser operating in the fundamental TEM_{00} mode usually requires the insertion of an aperture in the resonator to prevent higher-order modes oscillation [79]. In this case, the efficiency of the laser is lower as compared with multimode operation because of the small volume of active material involved in the lasing process. Larger-diameter TEM_{00} modes can be obtained using special resonator configurations. Efficient exploitation of the active material of a solid-state laser operating in the fundamental mode causes two conflicting problems: the TEM_{00} mode volume in the laser crystal has to be maximized, but the resonator should remain as insensitive as possible to focal length and alignment perturbations. Early solutions were purposed to compensate the thermal lens by a convex mirror, or by negative lenses ground at the end of the rod that exactly eliminates the

focusing effect in the gain medium [80]. With these methods high power in a single-mode beam can be obtained; however, the compensation is effective only for one particular value of the focal length. Large fundamental mode volume and good stability against thermal lens fluctuations have been achieved by a particular selection of mirror curvatures or by insertion of a telescope in the resonator.

To obtain good dynamic stability, the mode size must be small and the power must be extracted from a relatively small volume of gain medium. Thus, to produce high output power, one must intensely pump this small volume of gain medium and/or increase the length of the gain medium. However, in addition to the potential problem of crystal fracture, intense optical pumping will result in increased thermal birefringence, focusing, and distortion, which will decrease the efficiency and degrade beam quality. Increasing the length of the gain medium will increase the round-trip losses, thereby decreasing efficiency, and may compromise the spatial overlap of the laser mode and pumped region of the gain medium. Many of the problems cited above can be avoided by changing from stable to unstable resonators. The useful properties of these resonator were first discussed by Siegman in 1965. [81] Since then, they have been used extensively in high-gain chemical and gas lasers, where it has been demonstrated that unstable resonators can simultaneously produce diffraction-limited beams and efficiently extract power from extended gain media. It has also been shown that in an unstable resonator, the beam quality is largely insensitive to changes in the refractive power of a thermal lens as compared to a stable resonator [82, 83]. There has also been considerable effort devoted to understanding the mode structures of these resonators. A particularly useful feature of

unstable resonators is that output coupling fraction depends only on the magnification of the resonator and thus the mode size can be adjusted to fill the gain medium by merely increasing the mirror size. For our application with tens of watts power, we can just focus on stable resonators.

To obtain good beam quality, one may need to adjust the cavity parameters carefully, such as curvatures of mirrors, distances of components, and angles of alignments. Therefore, in optimization procedure, many merit functions can be used with respect to practical requirements, such as conversion efficiency, beam quality, heat dissipation, tolerance of opto-mechanical and assembly, compactness of cavity, temperature tolerance, fabrication and packaging costs, etc. In most cases, these requirements or variables cannot be optimized to reach their optimal values simultaneously, many trade-offs hence must be compromised in analyses and modeling.

2.2.4 *Thermal effects in end-pumped DPSS lasers*

Nowadays, the thermal effects are by far the most critical issue in the development of reliable solid-state lasers with useful beam quality and is addressed in worldwide intense research. In most cases, thermal management includes the following aspects [84, 85]:

1) The increased temperature in the gain media will cause the increasing of the fluorescence spectral line-width and decreasing of the quantum efficiency. These may lead to a higher threshold and a reduction of laser efficiency.

2) The ununiformed distribution in the laser crystal can cause thermal tress, thermal birefringence, and thermal lensing.

Due to the thermal expansion, the radial temperature distribution generates thermal stress. High stress may cause fracture. Thermal fracture limits the maximum operation power of a DPSS laser.

On the other hand, the stress can cause changes in refractive index via the photo-elastic effect and an isotropic crystal may become anisotropic one. This thermal birefringence effect will depolarize polarized light. This is not very important in applications that the light does not have to be polarized. However, nonlinear crystals demand polarized light for optimum frequency conversion. There are several approaches to compensate this thermally induced birefringence. One direct approach is to reduce the stress by either increasing the pump beam diameter or decreasing the doping level of laser crystal. An indirect method is to implement a quarter-wave plate into the cavity which will corrects for the depolarization.

When a laser crystal is pumped by a light source, the temperature in the crystal axis reaches maximum and decreases gradually to its edge. Figure 2.1 shows a finite element simulation of a $3 \times 3 \times 2$ mm^3 Nd:YVO_4 crystal with 3 W absorbed in a 200 μm diameter spot. The crystal is cooled from the surrounding copper holder and therefore shows a temperature distribution that is centrosymmetric around the pump spot. Since the thermal-optic coefficient of Nd:YVO_4 crystal is a constants, which means the temperature dependent refractive index would exhibit the same distribution as the temperature

distribution, which has a focusing effect (positive temperature coefficient) or a diverging effect (negative temperature coefficient).

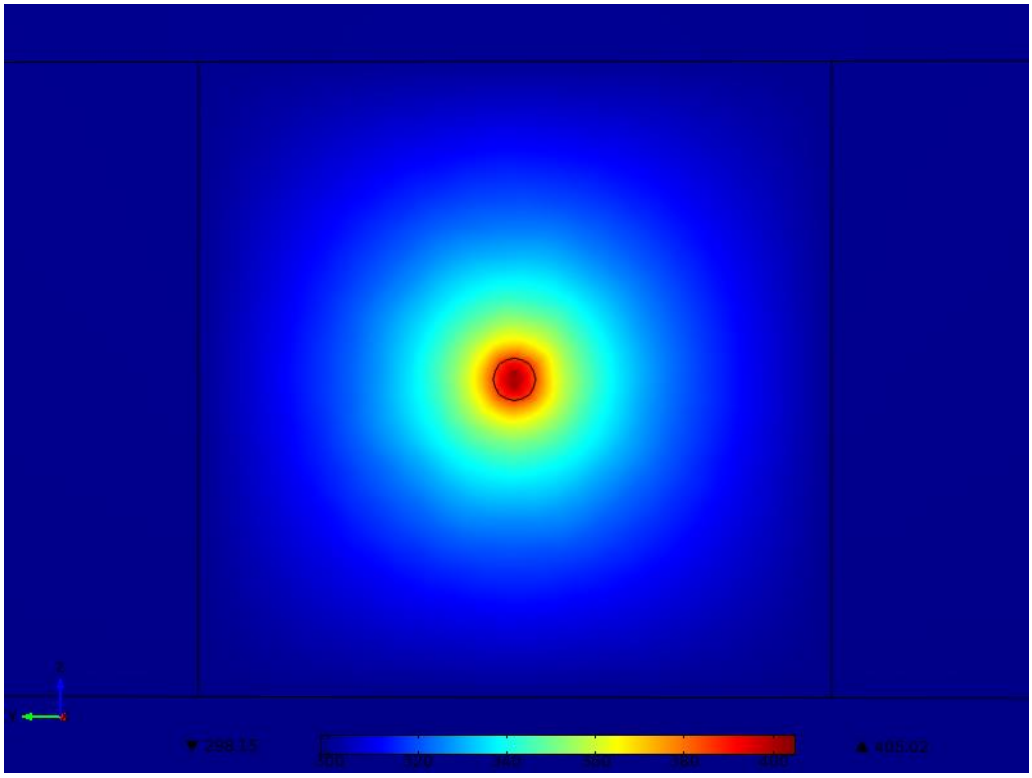

Figure 2.1. Finite element simulation of an end pumped Nd:YVO_4 crystal.

Figure 2.2 shows the 3-D and 2-D normalized refractive index distribution along the light propagation direction. This uneven temperature distribution causes curvature of an originally flat facet, which is also plays a focusing component. Innocenzi et al. derived a simple equation to calculate the focal length of such a thermal lens:

$$f = \frac{\pi K_\omega \omega_P^2}{P_\omega \left(\frac{dn}{dT}\right)} \left(\frac{1}{1 - e^{-\alpha l}}\right) \tag{2.1}$$

where K_ω is the thermal conductivity, ω_P is the pump beam diameter, P_ω is the heat power, and α is the absorption coefficient at the pump wavelength [86]. Perturbation of the thermal lens of the laser crystal leads mainly to changes in the mode structure and beam divergence.

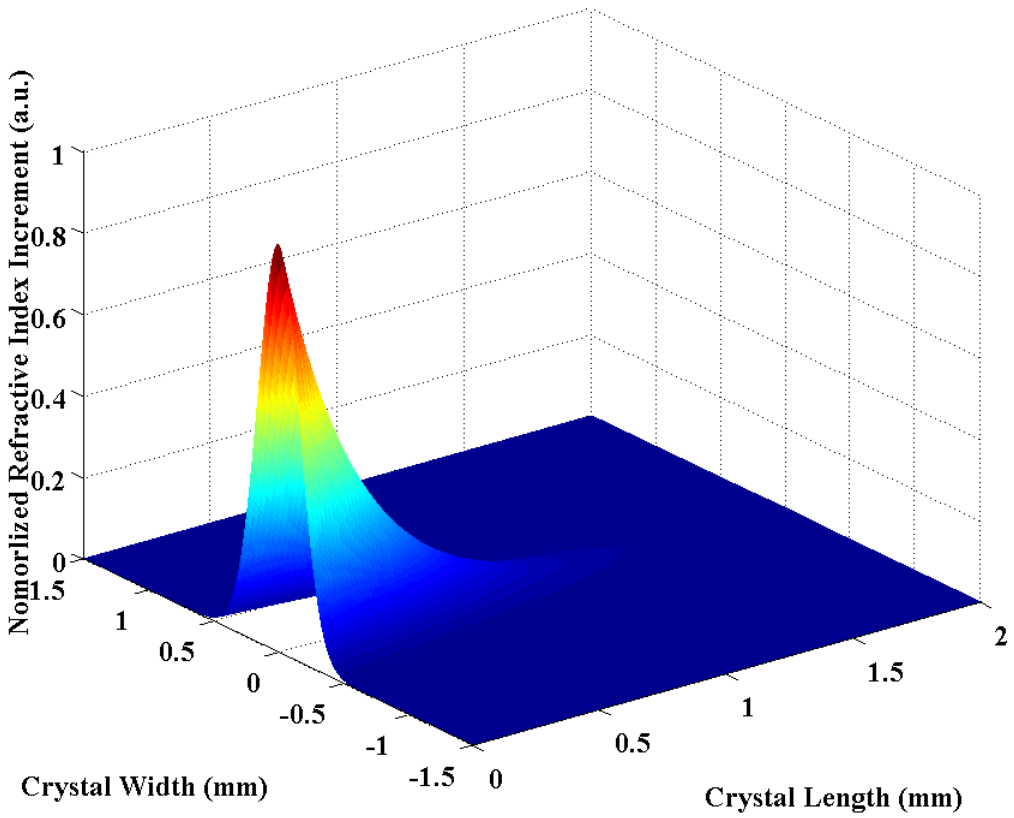

(a)

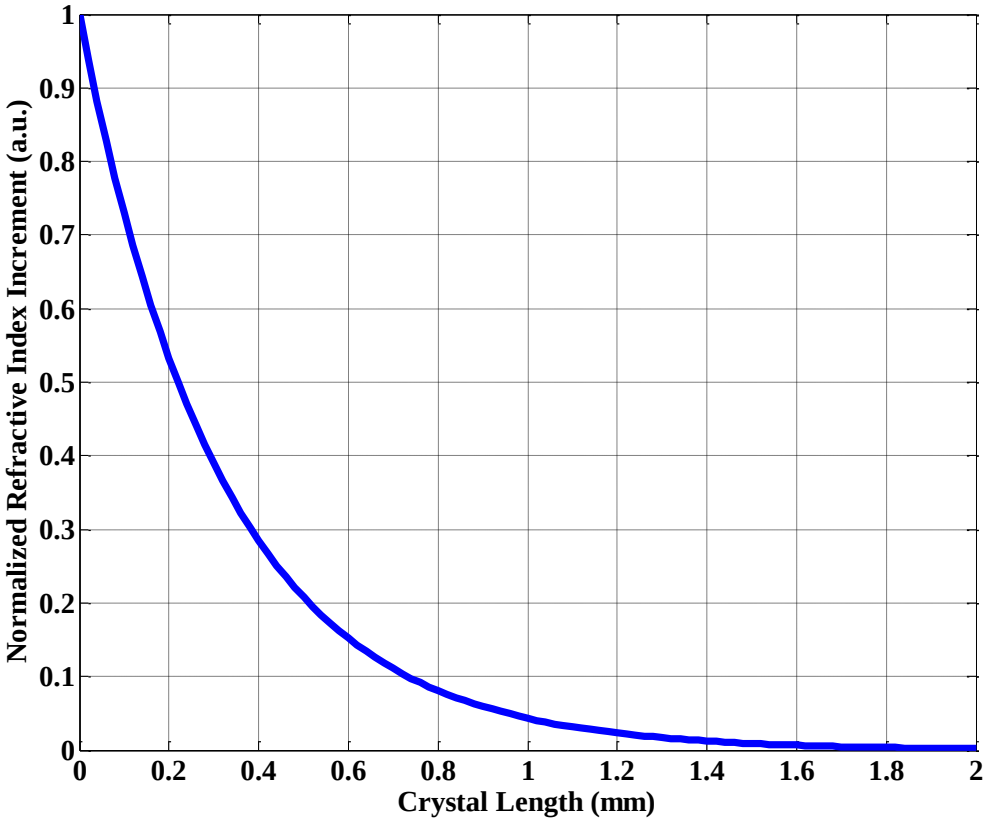

(b)

Figure 2.2. 3-D (a) and 2-D (b) refractive index increment distribution of an end pumped Nd:YVO_4 crystal.

A lot of valuable work have been done to eliminate thermal effects in powerful DPSS lasers, such as selecting a laser crystal with high thermal conductivity, reshaping the laser crystal, increasing pump and laser beam diameters, reducing the absorption coefficient, and using intra-cavity thermal compensated component.

2.3 Second-Order Nonlinear Interaction

2.3.1 *Nonlinear Interaction with Medium*

Optical mixing type wavelength conversion is based on the nonlinear optical properties of certain dielectric materials. A dielectric material is made up of atoms comprising a positively charged nucleus surrounded by an electron cloud (Figure 2.2). In equilibrium conditions, the positive and negative charges form a symmetrical structure. When an external electric field is applied on the material, the electric force distorts the electron cloud. This distortion causes a separation of the centers of positive and negative charges. The displacement of negative charge center from positive charge center is called polarization [62].

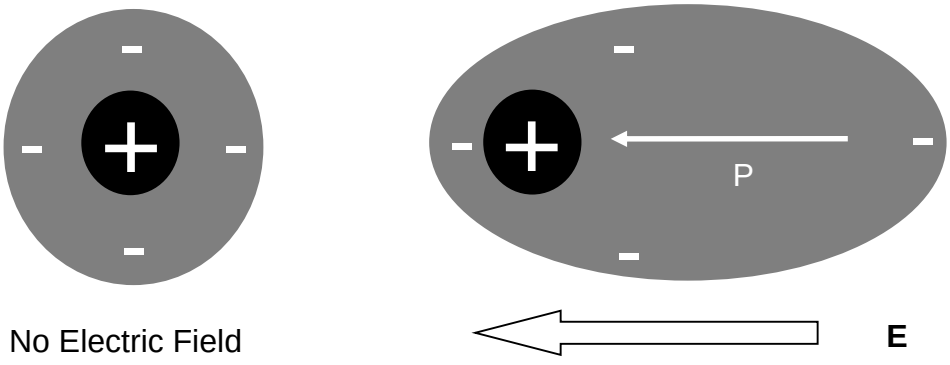

Figure 2.3. Schematic of charge displacement caused by an external electric filed.

All dielectric materials have a macroscopic electric polarization density (***P***) which can be mathematically described as a power series of the applied electric field (***E***):

$$\boldsymbol{P} = \varepsilon_0\chi^{(1)}\boldsymbol{E} + \varepsilon_0\chi^{(2)}\boldsymbol{E}^2 + \varepsilon_0\chi^{(3)}\boldsymbol{E}^3 + \ldots \quad (2.2)$$

where ε_0 is the dielectric permittivity of the vacuum, χ is known as the dielectric susceptibility. $\chi^{(1)}$ and $\chi^{(n)}$ is the linear and n-th order nonlinear susceptibility, respectively [87]. In the case of conventional linear optics, since $\chi^{(1)} \gg \chi^{(2)}$, and the applied electric field strength is not that strong, the high order part can be ignored. The induced polarization depends linearly upon the electric field strength:

$$\boldsymbol{P} = \varepsilon_0\chi^{(1)}\boldsymbol{E} \quad (2.3)$$

this first term does not produce new frequency components, and is only responsible for the linear optical phenomena such as refraction, diffraction, and dispersion.

When studying the interaction between a laser beam and a certain medium, the electric field strength is so strong that the high order terms cannot be ignored. For most materials, $\chi^{(2)} \gg \chi^{(3)}$, so the second order nonlinear phenomenon is easy to observe in these materials when interacting with lasers. The second order term in equation (2.2):

$$\boldsymbol{P^{(2)}} = \varepsilon_0\chi^{(2)}\boldsymbol{E^2} \quad (2.4)$$

is so called second order nonlinear polarization. Generally, three-wave mixing takes place through the second-order nonlinear polarization.

The nonlinear polarization acts as the source of new frequency components of the electromagnetic field. If we consider two light fields with two different frequencies, ω_1 and ω_2, impinging on the crystal:

$$\boldsymbol{E} = \boldsymbol{E_1}\cos(\omega_1 t) + \boldsymbol{E_2}\cos(\omega_2 t) \quad (2.5)$$

then the second order nonlinear polarization becomes:

$$\boldsymbol{P}_2 = \varepsilon_0\chi^{(2)}[\boldsymbol{E}_1^2\cos^2(\omega_1 t) + \boldsymbol{E}_2^2\cos^2(\omega_2 t) + \boldsymbol{E}_1\boldsymbol{E}_2\cos(\omega_1 t)\cos(\omega_2 t)]$$

$$= \varepsilon_0\chi^{(2)}[\frac{1}{2}(\boldsymbol{E}_1^2 + \boldsymbol{E}_2^2) + \frac{1}{2}\boldsymbol{E}_1^2\, cos(2\omega_1 t) + \frac{1}{2}\boldsymbol{E}_2^2\, cos(2\omega_2 t)$$

$$+\varepsilon_0\chi^{(2)}[\boldsymbol{E}_1\boldsymbol{E}_2\, cos[(\omega_1 + \omega_2)t] + \boldsymbol{E}_1\boldsymbol{E}_2\, cos[(\omega_1 - \omega_2)t]] \qquad (2.6)$$

From the above equation, we can find that the output consists of a time independent DC term (optical rectification, OR) and four terms involving new frequencies:

$2\omega_1, 2\omega_2$: Second Harmonic Generation (SHG)

$\omega_1 + \omega_2$: Sum Frequency Generation (SFG)

$\omega_1 - \omega_2$: Difference Frequency Generation (DFG)

Theoretically, all the four nonzero frequency components should be present in the nonlinear polarization if there are two different frequency incident radiations. However, typically no more than one of these components will be present in the nonlinear optical interactions. That is because the nonlinear polarization can efficiently generate an output radiation only if a certain phase-matching condition is satisfied, and usually this condition cannot be satisfied for more than one frequency component of the nonlinear polarization. The phase-matching condition will be discussed in the third section of this section.

SHG is the simplest three-wave mixing interaction. It can be treated as a special case of SFG, such that $\omega_1 = \omega_2$. In other words, there is only one incident radiation at frequency ω. Then for the equation 2.6, the output only has the second harmonic term 2ω left. That is the reason why SHG is also called frequency doubling. In SHG process, two photons at frequency ω are destroyed and one photon at frequency 2ω is simultaneously created in a single quantum-mechanical process. The whole process satisfies energy conservation [88].

Under proper SHG experimental conditions, nearly all of the incident radiation power can be converted to radiation at the second harmonic generation frequency. Moreover, SHG is commonly used as the first practical nonlinear frequency conversion process when developing a new nonlinear optical material or device. Preliminary SHG demonstrations also indicate a design's practicality for other conversion techniques such as difference and sum frequency generation or optical parametric oscillation and amplification.

2.3.2 Maxwell Equations and Coupled Wave Equation

In this section, we first examine how Maxwell's equations describe the generation of new frequency components of the field, and see how the various frequency components of the field become coupled by the nonlinear interaction. At first, we write Maxwell's equations in SI units as:

$$\nabla \cdot \boldsymbol{D} = \rho \tag{2.7}$$

$$\nabla \cdot \boldsymbol{B} = 0 \tag{2.8}$$

$$\nabla \times \boldsymbol{E} = -\frac{\boldsymbol{\partial B}}{\boldsymbol{\partial} t} \tag{2.9}$$

$$\nabla \times \boldsymbol{H} = \boldsymbol{J} + \frac{\partial \boldsymbol{D}}{\partial t} \tag{2.10}$$

where is $\boldsymbol{E}$ the electric field, $\boldsymbol{H}$ is the magnetic field, $\boldsymbol{D}$ is the electric flux density, $\boldsymbol{B}$ is the magnetic flux density, $\boldsymbol{J}$ is the free current density, and ρ is free charge density. Since we are dealing with a dielectric material, we have:

$$\boldsymbol{J} = 0 \tag{2.11}$$

$$\rho = 0 \tag{2.12}$$

we also assume that the material is nonmagnetic, so that:

$$\boldsymbol{B} = \mu \boldsymbol{H} = \mu_0 \boldsymbol{H} \tag{2.13}$$

where μ is permeability of material and μ_0 is the permeability of free space. Then we consider the nonlinear polarization:

$$\boldsymbol{D} = \varepsilon \boldsymbol{E} = \varepsilon_0 \varepsilon_r \cdot \boldsymbol{E} + \boldsymbol{P} \tag{2.14}$$

where ε is the permittivity, ε_0 is the permittivity of free space, ε_r is the relative permittivity.

Taking the curl of both side of equation (2.9):

$$\nabla \times \nabla \times \boldsymbol{E} = -\frac{\partial}{\partial t}(\nabla \times \boldsymbol{B}) \tag{2.15}$$

Combining equations (2.10), (2.11), (2.13), and (2.15), we can get the following equation:

$$\nabla \times \nabla \times \boldsymbol{E} = -\mu_0 \frac{\partial^2}{\partial t^2} \boldsymbol{D} \tag{2.16}$$

Using (2.14) and the vectorial identity ($\nabla \times \nabla \times \boldsymbol{E} = \nabla\nabla \cdot \boldsymbol{E} - \nabla^2 \boldsymbol{E}$) in the case of no sources ($\nabla \cdot \boldsymbol{E} = 0$), we can get the inhomogeneous optical wave equation under the slowly varying amplitude approximation is derived as:

$$\left(-\nabla^2 + \frac{1}{c^2}\frac{\partial^2}{\partial t^2}\right)\boldsymbol{E}(\boldsymbol{r}, t) = -\mu_0 \frac{\partial^2}{\partial t^2}\boldsymbol{P}(\boldsymbol{r}, t) \tag{2.17}$$

where the polarization vector $\boldsymbol{P}$ is often split into its linear and nonlinear parts as:

$$\boldsymbol{P}(r, t) = \boldsymbol{P}^{(1)}(\boldsymbol{r}, t) + \boldsymbol{P}^{NL}(\boldsymbol{r}, t) \tag{2.18}$$

Both $\boldsymbol{E}(\boldsymbol{r}, t)$ and $\boldsymbol{P}(\boldsymbol{r}, t)$ can be decomposed into a set of finite plane waves:

$$\boldsymbol{E}(\boldsymbol{r}, t) = \sum_n \boldsymbol{E}_n e^{-i(\omega_n t - k_n \cdot \boldsymbol{r})} \tag{2.19}$$

$$\boldsymbol{P}^{(1)}(\boldsymbol{r}, t) = \sum_n \chi^{(1)}(\omega_n) \cdot \boldsymbol{E}_n(\omega_n, k_n) \tag{2.20}$$

$$\boldsymbol{P}^{NL}(\boldsymbol{r},t) = \sum_{n} \boldsymbol{P}^{NL}(\boldsymbol{r}) e^{-i(\omega_n t - k_n \cdot \boldsymbol{r})} \tag{2.21}$$

where $\boldsymbol{E}_n$ is the spatially slowly varying amplitude of the electric field. Substituting (2.18), (2.19), (2.20) and (2.21) into (2.17), the wave equation now becomes as:

$$\left(-\nabla^2 + \frac{\omega_n^2}{c^2}\right)\boldsymbol{E}_n = -\mu_0 \omega_n^2 \boldsymbol{P}^{NL} \tag{2.22}$$

then, for n fields $\boldsymbol{E}$, there should be a set of $n+1$ couple wave equations.

In a second order nonlinear process, we only focus on the second order polarization, which is given in the form as:

$$\boldsymbol{P}^{(2)} = \varepsilon_0 \chi^{(2)} \boldsymbol{E}^2 \tag{2.23}$$

In technical literatures, rather than $\chi^{(2)}$, it is more common to see the 'nonlinear coefficient' d, which is defined as

$$d = \frac{\chi^{(2)}}{2} \tag{2.24}$$

Then, for the SHG process, the component of the second order polarization can be written as:

$$\boldsymbol{P}_{\omega}^{(2)} = 2d\varepsilon_0 \boldsymbol{E}_{2\omega} \boldsymbol{E}_{\omega}^{*} \tag{2.25}$$

$$\boldsymbol{P}_{2\omega}^{(2)} = d\varepsilon_0 \boldsymbol{E}_{\omega}^2 \tag{2.26}$$

then we can reach the following coupled mode equations for SHG process:

$$\frac{\partial \boldsymbol{E}_{\omega}(z)}{\partial z} = -i\kappa^{*} \boldsymbol{E}_{2\omega}(z) \boldsymbol{E}_{\omega}^{*}(z) e^{-i\Delta k z} \tag{2.27}$$

$$\frac{\partial \boldsymbol{E}_{2\omega}(z)}{\partial z} = -i\kappa \boldsymbol{E}_{\omega}(z) \boldsymbol{E}_{\omega}^{*}(z) e^{i\Delta k z} \tag{2.28}$$

where Δk is the phase velocity mismatch due to material dispersion, which is defined as:

$$\Delta k = k_{2\omega} - 2k_{\omega} = \frac{4\pi}{\lambda_{\omega}}(n_{2\omega} - n_{\omega}) \tag{2.29}$$

where $k_{2\omega}$ and k_{ω} are the propagation constants of pump and SHG light.

The parameter κ is the coupling coefficient for the SHG process, which is defined in the form of:

$$\kappa = \varepsilon_0 d_{eff} \sqrt{\frac{(2\omega)^2}{2n_{\omega}^2 n_{2\omega} A_{eff}} \left(\frac{\mu_0}{\varepsilon_0}\right)^{\frac{3}{2}}} \tag{2.30}$$

where, ε_0 and μ_0 is the permittivity and permeability of free space, respectively, n_{ω} and $n_{2\omega}$ are the refractive index of pump and SHG light. A_{eff} is the effective area. In waveguide devices, it is convenient to assume the A_{eff} close to the area of guided mode profiles. d_{eff} is the effective SHG coefficient. When we assume the interaction optical beam having uniform cross sections in a homogeneous medium, d_{eff} can be considered equalling nonlinear coefficient d.

With boundary condition: $E_{\omega}(0) = E_0$ and $E_{2\omega}(0) = 0$, where E_0 is the amplitude of the incident pump light, the coupled-mode equations (2.27) and (2.28) can be solved under two different assumptions:

1) Pump nondepletion solution: If the conversion efficiency is low, therefore there is a very small depletion of the pump light power. We can approximate that $\boldsymbol{E}_{\omega}(z) = \boldsymbol{E}_0$. Then, combining the coupled-mode equations (2.27) and (2.28), we can get:

$$E_{2\omega}(z) = -i\kappa E_0^2 \exp\left(\frac{i\Delta kz}{2}\right)\left(\frac{sin\Delta kz/2}{\frac{\Delta kz}{2}}\right) \tag{2.31}$$

$$P_{2\omega}(z) = \frac{8\pi^2}{n_\omega^2 n_{2\omega} \lambda_\omega^2 c\varepsilon_0} d_{eff}^2 z^2 \frac{sin^2(\Delta kz/2)}{(\Delta kz/2)^2} \frac{P_\omega^2(0)}{A_{eff}} \tag{2.32}$$

and the SHG conversion efficiency is defined as:

$$\eta = \frac{P_{2\omega}(z)}{P_\omega(0)} = \frac{8\pi^2}{n_\omega^2 n_{2\omega} \lambda_\omega^2 c\varepsilon_0} d_{eff}^2 L^2 \frac{sin^2(\Delta kz/2)}{(\Delta kz/2)^2} \frac{P_\omega(0)}{A_{eff}} \tag{2.33}$$

The normalized conversion efficiency η_{nor}, another commonly used parameter to represent the conversion performance, is given in the form as:

$$\eta_{nor} = \frac{P_{2\omega}(L)}{P_\omega^2(0)L^2} = \frac{8\pi^2}{n_\omega^2 n_{2\omega} \lambda_\omega^2 c\varepsilon_0} d_{eff}^2 \frac{sin^2(\Delta kz/2)}{(\Delta kz/2)^2} \frac{1}{A_{eff}} \tag{2.34}$$

It is only depends on the nonlinear properties of the medium and the overlap of the interacting waves.

2) Pump depletion solution: If the conversion efficiency is high enough that the pump amplitude cannot be treated as a constant. The coupled-mode equations (2.27) and (2.28) must be solved with the boundary condition ($E_\omega(0) = E_0, E_{2\omega}(0) = 0$) and the power conservation relation:

$$\frac{d}{dz}(|\boldsymbol{E}_\omega(z)|^2 + |\boldsymbol{E}_\omega(z)|^2) = 0 \tag{2.35}$$

The solutions to these equations are available in literatures. The SHG output power under pump depletion assumption is given by:

$$P_{2\omega}(z) = P_\omega(0)\tanh^2\left[C\sqrt{\frac{P_\omega(0)}{A_{eff}}}z\right] \tag{2.36}$$

where

$$C = \frac{8\pi\omega d_{eff}}{c^2\sqrt{\varepsilon}}\sqrt{\frac{2\pi c}{\sqrt{\varepsilon}}} \tag{2.37}$$

This function is plotted in Figure 2.3. We can see that the conversion efficiency approaches 100% asymptotically with increasing the crystal length. As we discuss before, only at low conversion efficiency, power nondepletion assumption can be applied. From Figure 2.3, we can see that the low efficiency approximation is adequate to around 10% conversion efficiency.

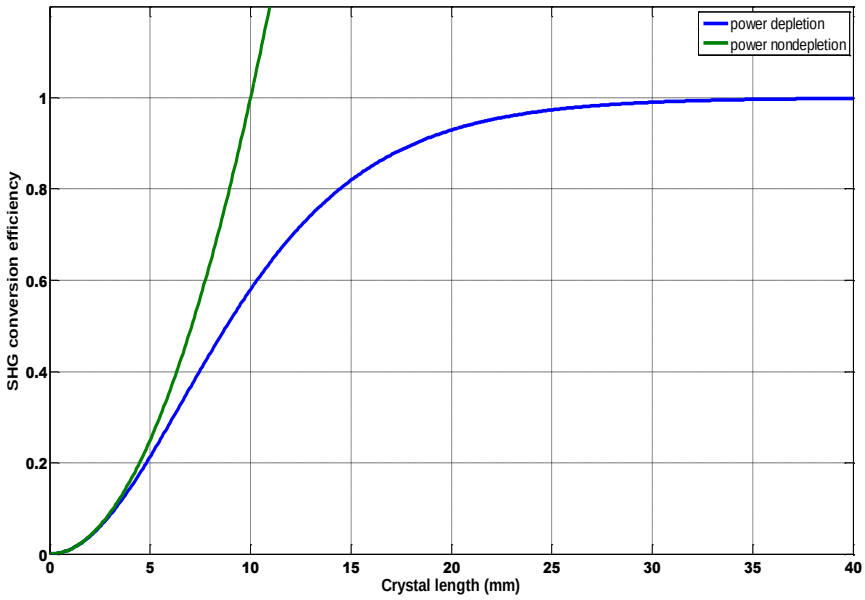

Figure 2.4. SHG conversion efficiency as a function of crystal length (pump depletion assumption and pump nondepletion assumption).

2.3.3 Phase Matching

Equation (2.33) shows all the factors which will affect the SHG output power. Apparently, using longer devices based on higher second nonlinear coefficient and

confining the incident beam and generated beam within a small cross-section area will lead to higher SHG conversion efficiency. Moreover, the major factor affecting the output power shown in (2.33) is the wavevector mismatch $\Delta k = k_{2\omega} - k_{\omega} = \frac{4\pi}{\lambda_{\omega}}(n_{2\omega} - n_{\omega})$, which is called the phase matching condition. It is easy to draw the relationship between SHG conversion efficiency and phase mismatch (Figure 2.4).

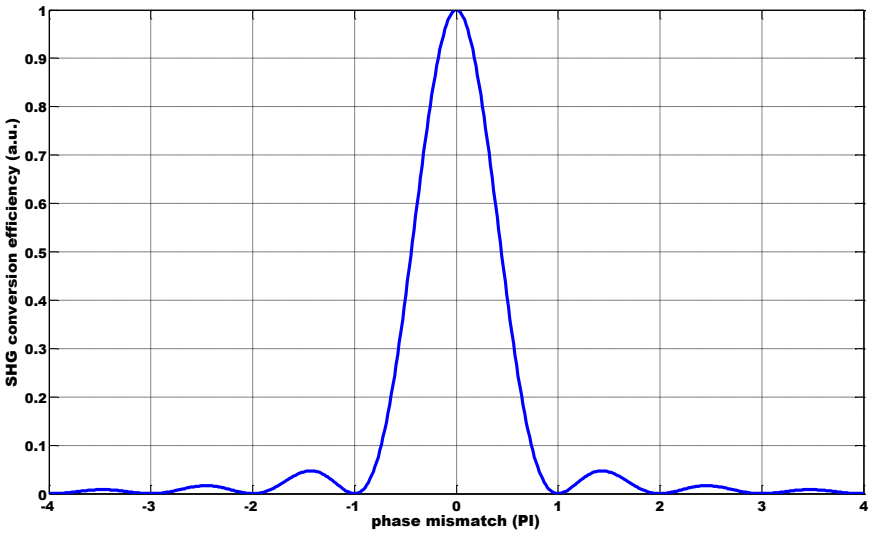

Figure 2.5. Effects of phase mismatch on the SHG conversion efficiency.

Obviously, only when the $\Delta k = 0$, or perfect phase matching, will the output power achieve the maximum value. In the meantime, on the wave propagation direction, SHG power can continuously increase only when the phase perfect matched. Otherwise, the SHG output power oscillates between zero and its maximum value, which leads a dramatic decrease in the conversion efficiency (Figure 2.5).

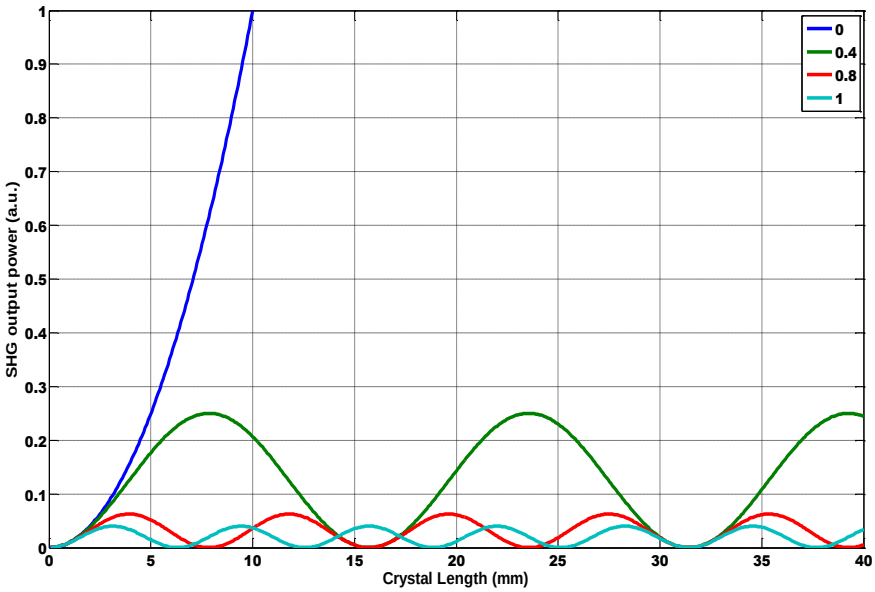

Figure 2.6. Growth of SHG power along the propagation direction with different phase mismatch.

The phase matching condition usually is difficult to achieve because the refractive index of the material is an increasing function of frequency in the normal dispersion range. For example, in SHG process, to satisfy phase matching condition, $n_{2\omega}$ and n_{ω} has to be equal, which is impossible while $2\omega > \omega$. In principle, it is possible to achieve the phase-matching condition by making use of abnormal dispersion, in which the decrease in refractive index with increasing frequency occurs near an absorption feature. However, the most typical method for achieving phase matching is to make use of the birefringence property of many nonlinear optical crystals.

Birefringence is the dependence of the refractive index on the direction of polarization of the light. By carefully choosing the polarizations of fundamental light and generated light, the phase matching condition will be satisfied.

For instance, in a negative uniaxial crystal, the category which most common nonlinear optical crystals belong to, the extraordinary axis has a smaller refractive index than the ordinary axes. Then, to achieve the phase matching condition for SHG process, we have two methods:

$$n_e(2\omega) = n_o(\omega) \tag{2.38}$$

$$\boldsymbol{E}_o(\omega) + \boldsymbol{E}_o(\omega) \longrightarrow \boldsymbol{E}_e(2\omega) \tag{2.39}$$

or

$$n_e(2\omega) = \frac{1}{2}[n_o(\omega) + n_e(\omega)] \tag{2.40}$$

$$\boldsymbol{E}_o(\omega) + \boldsymbol{E}_e(\omega) \longrightarrow \boldsymbol{E}_e(2\omega) \tag{2.41}$$

the condition specified by equations 2.38 & 2.39 is called "Type-1 phase matching" and the condition given by 2.40 & 2.41 is called "Type-2 phase matching". BPM is usually achieved by a method called angle tuning. This method involves precise angular orientation of the crystal with respect to the propagation direction of the incident light. However, the angle tuning method has one serious drawback. If there is an angle with any value other than 0 or 90 degree between the propagating direction of extraordinary wave and the optical axis, the Poynting vector $\boldsymbol{S}$ and the propagation vector $\boldsymbol{k}$ will not be parallel. As a result, the ordinary and extraordinary rays with parallel propagation vectors will quickly diverge from each other. This walk-off effect decreases the overlap of fundamental waves and generated waves, which limits the nonlinear optical conversion efficiency.

For some crystals, the amount of birefringence is strongly temperature-dependent. As a result, it is possible to achieve phase matching in these crystals by controlling the device at a certain temperature. This method is called temperature tuning.

BPM methods are limited by many factors, such as angle, wavelength and temperature. There is another method known as quasi-phase matching (QPM) that can be used to achieve phase matching. The idea of QPM was first proposed by Armstrong in 1962 [89]. But there was no practical technique to realize QPM for wavelength conversion until 1980's [90].

QPM does not depend on birefringence of materials, but instead, on creating a periodic domain inverse structure in the nonlinear optical material. This periodic domain inverse structure periodically inverts one of the crystalline axes, often the optical axis of a ferroelectric material. This inversion leads the sigh of the nonlinear coupling coefficient d_{eff} ($d_{eff} = \chi^{(2)}/2$) periodically inverting. The inversion period Λ is carefully chosen as twice of the coherent length l_c ($l_c = \frac{\pi}{\Delta k}$). Thus, each time the amplitude of the generated electric field is about to decrease due to the phase mismatch, the reversal of the sign of polarization occurs which allows the amplitude to continue increasing. Through this mean, the nonzero wave-vector mismatch can be compensated. Figure 2.6 illustrates the comparison effect of three phase matching conditions.

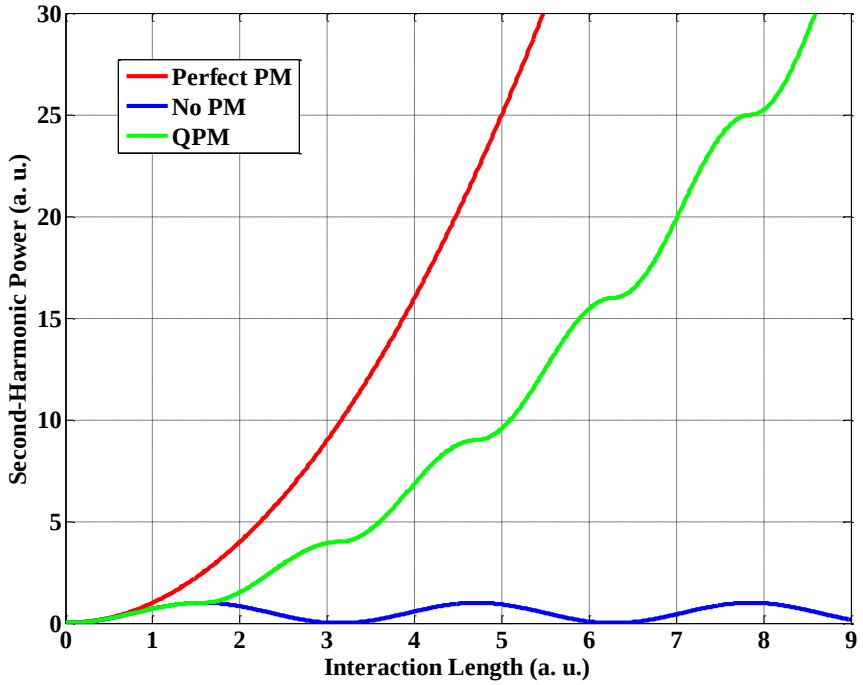

Figure 2.7. Comparison of the growth of SHG power for three different phase matching condition (phase-matched, non-phase-matched, quasi-phase-matched).

Compared to other phase matching methods, the QPM technique has many advantages. Table 2.2 shows a brief comparison between QPM and BPM. Although the conversion efficiency of QPM is theoretically lower than the perfect phase matching, using QPM technique usually dramatically enhances the conversion efficiency in practical applications because QPM can use the largest nonlinear coefficient while usually it is impossible for BPM. Moreover there is no limitation for QPM method, so wavelength conversion in the whole transparent window of the crystal can be achieved simply by choosing the appropriate QPM structure period.

Table 2.2. Comparison of QPM and BPM

Quasi-Phase Matching	**Birefringent Phase Matching**
Noncritical phase matching, no walkoff	Mostly critical phase matching, walkoff
Larger diagonal nonlinear coefficients can be used	Only smaller, non-diagonal coefficients can be used
Phase matching any wavelength combinations within crystal transparency	Limited phase matching wavelength (e.g. no blue SHG for $LiNbO_3$)
Tuning via temperature, multiple or continuous fan-out type grating periods	Tuning via temperature and angle
Wide acceptance bandwidth/angle, easy to align	Limited acceptance bandwidth/angle, difficult to align
User design friendly criteria	

A number of different technologies have been developed for the fabrication of quasi-phase matched structures in past decades, including direct writing by electron beams, titanium indiffusion, electric-field poling and techniques based on wafer bonding [91]. Some of them are already matured and cost efficient. The detail of the fabrication of QPM structure will be introduced in next chapter.

2.4 Intra-cavity Frequency Doubling

Placing the nonlinear crystal inside the laser cavity removes the need of complex feedback electronics and potentially a much smaller and less complex laser can be constructed. Thus, intra-cavity frequency doubled lasers are the most attractive scheme for constructing visible wavelength CW solid state lasers.

We will now consider the effect of including a nonlinear crystal within a laser cavity to generate the second harmonic wave. Intra-cavity frequency doubling is attractive for CW systems, to take advantages of the high intensity within the cavity. Carrying forward the assumptions made in the preceding sections concerning the use of the small signal approximation, the intra-cavity frequency doubling of a solid state laser can be modelled by examine the loss and gain of such a laser.

Considering a laser crystal and a nonlinear crystal, the polarized fundamental and second harmonic electric field at time t and position r can be written as

$$\tilde{E}_1(\vec{r},t) = \frac{1}{2}\left[E_1^+(r,z)e^{jk_1 z} + E_1^-(r,z)e^{-jk_1 z}\right]e^{-j\omega_1 z} + c.c. \qquad (2.42)$$

$$\tilde{E}_2(\vec{r},t) = \frac{1}{2}\left[E_2^+(r,z)e^{jk_2 z} + E_1^-(r,z)e^{-jk_2 z}\right]e^{-j\omega_2 z} + c.c. \qquad (2.43)$$

where $E_1^+(E_1^-)$ is the forward (backward) fundamental envelop field (V/cm) and $E_1^+(E_1^-)$ is the forward (backward) second harmonic envelop field, k_1 and k_2 are the wave vector of the fundamental and second harmonic wave, ω_1 and ω_2 are the frequency of the fundamental and second harmonic wave, $r = (x, y)$ is the transverse coordinate, z is the longitudinal coordinate. By using slow varying envelop approximation, the electrical

fields are reduced to plane waves. In the laser crystal section, forward and backward fundamental waves in the propagation direction z are

$$\pm\frac{dE_1^{\pm}}{dz}=\left[\frac{1}{2}g-\frac{1}{2}\alpha_1-\frac{jk_1(n^2-n_0^2)}{n_0}\right]E_1^{\pm} \tag{2.44}$$

the saturated gain in the laser crystal g is

$$g=\frac{g_0}{1+I_1/I_{sat}} \tag{2.45}$$

where I_1 is the total intensity of the fundamental wave in the cavity which relates to the forward and backward fundamental intensities by $I_1(z)=I_1^+(z)+I_1^-(z)$. g_0 is the small-signal gain, and is related to the population inversion density ΔN (cm^{-3}) through $g_0=c\sigma\Delta N$.

The rate equation for population inversion density ΔN is written as a spatial dependant rate equation for a single transvers mode and an ideal four-level laser

$$\frac{d\Delta N(r,z)}{dt}=R_P(r,z)-\frac{\Delta N(r,z)}{\tau}-c\sigma\Delta N(\phi_1^+ +\phi_1^-) \tag{2.46}$$

where R_P is the pump rate, ϕ_1 is the fundamental photon density in the cavity (cm^{-3}). The photon densities are related to the envelop fields

$$\phi_i^{\pm}=\frac{I_i^{\pm}}{chv_i}=\frac{\frac{1}{2}\varepsilon_0 cn\left|E_i^{\pm}\right|^2}{chv_i}=\frac{\varepsilon_0 n}{2hv_i}\left|E_i^{\pm}\right|^2 \tag{2.47}$$

where h is Plank's constant, v is the frequency of the fundamental wave, n is the reflective index of the active material, ε_0 is the permittivity in vacuum.

For end pump scheme, considering a uniform pump beam profile along z direction, the pump rate is

$$R_P(z) = \frac{P_{in}}{h v_P} \frac{2\alpha \exp(-\alpha z)}{\pi \omega_{P0}^2 [1 - \exp(-\alpha l_1)]} \tag{2.48}$$

where P_{in} is the incident pump power, α is the absorption coefficient at the pump wavelength, v_P is the pump frequency, ω_{P0} is the pump beam waist radius, l_1 is the laser crystal length.

The nonlinear interactions for the forward and backward fundamental and second harmonic waves in the QPM crystal reads

$$\pm \frac{dE_1^{\pm}}{dz} = -jk_{12}^2 \chi^{(2)} E_1^{\pm *} E_2^{\pm} e^{\mp j\Delta_{SH} z} - \frac{1}{2}\alpha_1 E_1^{\pm} \tag{2.49}$$

$$\pm \frac{dE_2^{\pm}}{dz} = -jk_{12}^2 \chi^{(2)} E_1^{\pm 2} e^{\pm j\Delta_{SH} z} - \frac{1}{2}\alpha_2 E_2^{\pm} \tag{2.50}$$

where Δ_{SH} is the QPM mismatch factor

$$\Delta_{SH} = \frac{2\pi n_2}{\lambda_2} - \frac{4\pi n_1}{\lambda_1} - \frac{2\pi}{\Lambda} \tag{2.51}$$

in which, Λ is the period of periodical domain inversed structure.

Right facet boundary conditions for the fundamental is

$$E_i^-(L) = E_i^+(L)\sqrt{R_2} \tag{2.52}$$

and the left planar facet boundary condition is

$$E_i^-(L) = E_i^+(L)\sqrt{R_1} \tag{2.53}$$

where R_1 and R_1 are the power reflectivity.

A simple difference method is used to solve the coupled mode equations and the rate equation of population inversion. The gain/loss and nonlinear interaction terms in the cavity are solved by the 4-order R-K method. The two direction traveling electrical

fields are linked by the certain boundary condition. Convergence is reached after several round-trip interactions.

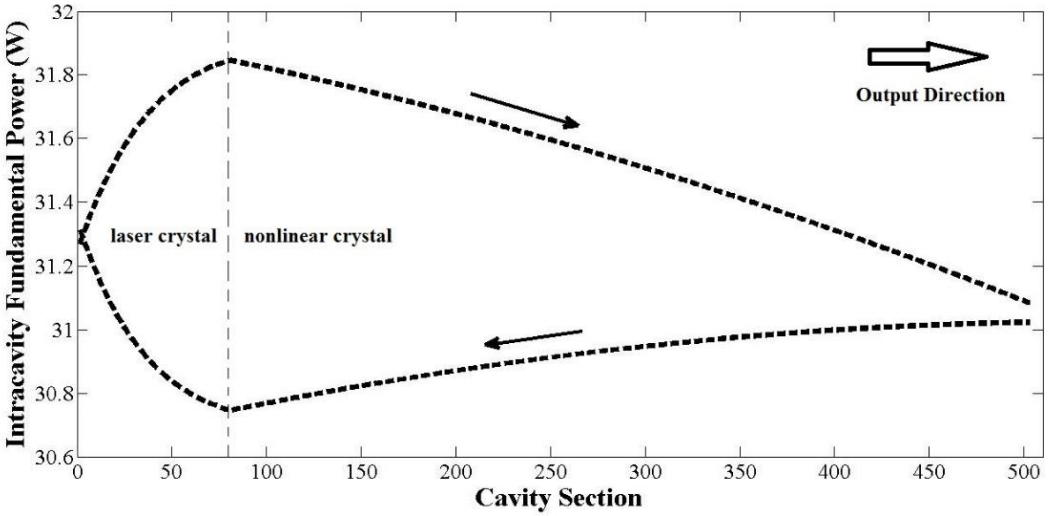

Figure 2.8. Calculated intra-cavity power distribution of fundamental wave.

Figure 2.7 shows the power distribution of fundamental 1064 nm laser light when pump power is 3 Watt and length of PPLN is 2 mm. We can find that the distribution in not uniform in both the laser crystal and the nonlinear crystal which cause the non-uniform of heat generation due to the linear absorption in the crystal.

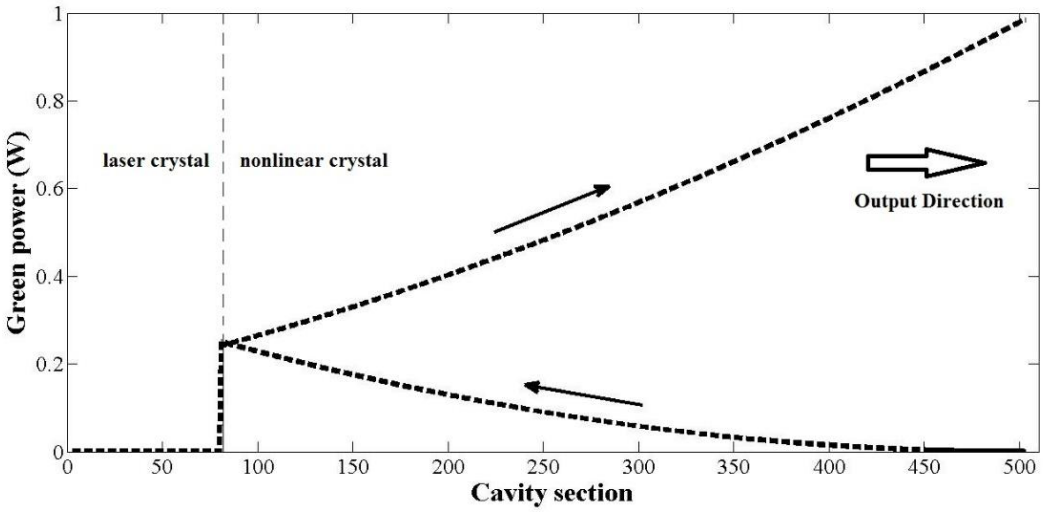

Figure 2.9. Calculated intra-cavity power distribution of second harmonic wave.

Figure 2.8 shows the power distribution of second harmonic wave in the cavity. As the same situation of fundamental wave, non-uniform distribution is also found for second harmonic wave. Since the fundamental wave and second harmonic wave distribution trend are opposite, the heat generated by absorption is compensated along the propagation direction inside the nonlinear crystal. In our calculation, we find the temperature gradient is less than 0.1 ℃ for 2 mm long PPLN crystal. Thus, the longitudinal phase mismatch chirp introduced by non-uniform heat distribution can be negligible with proper heat sink design.

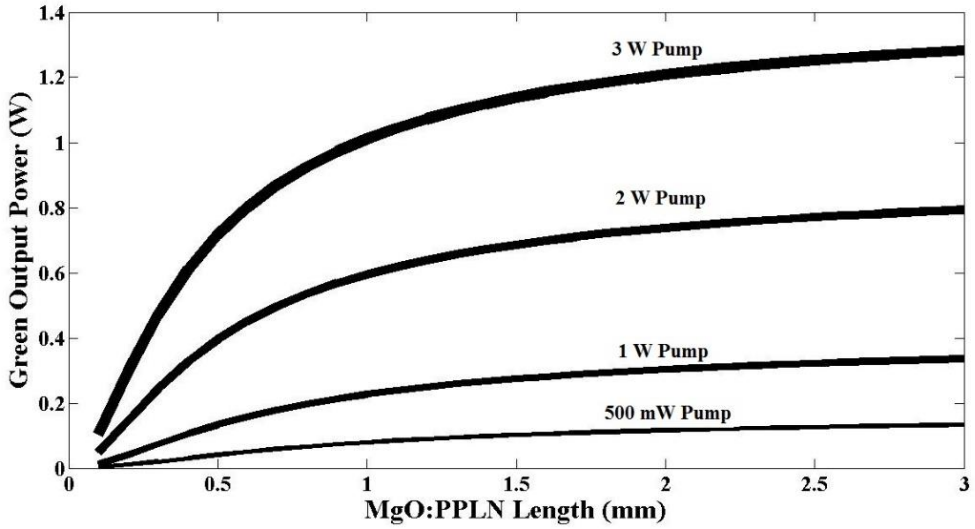

Figure 2.10. Calculated result of green output power of the IC-SHG DPSS laser as a function of MgO:PPLN length under the various pump power.

Figure 2.9 shows the simulated result of green output power of the IC-SHG DPSS laser as a function of MgO:PPLN length under various pump power. This result is used to help us to design the nonlinear crystal for different applications. In this paper, we choose 1.6 mm long MgO:PPLN in order to achieve over 1 Watt green output with pump power close to 3 Watt.

CHAPTER 3

GREEN LASERS BASED ON SINGLE-PASS FREQUENCY DOUBLING

3.1 Introduction

The most straightforward method to generate green light is to employ single-pass frequency doubling of 1064 nm light. Compared with intra-cavity and resonant enhanced frequency doubling, the single-pass process has the most simple and stable configuration. Moreover, high beam quality, low noise, and single frequency output can be more easily achieved by the single-pass method. But the single pass SHG in normal BMP nonlinear crystals, such as KTP and LBO, is limited by low second order nonlinearity and walk-off effect. Using PPLN crystals in single pass SHG process is superior to others since the d_{33} coefficient in lithium niobate is the largest among commonly used ferroelectrics and there is no walk-off effect in QPM nonlinear crystals.

The fundamental 1064 nm light can be generated by traditional DPSS lasers, fiber lasers, and semiconductor lasers. Among these configurations, single-pass frequency doubling of fiber lasers has superior qualities over others, including high EO efficiency, low noise, high beam quality, compactness and low cost, which is especially suitable for laser display applications.

Based on the theory described in Chapter Two, for a certain nonlinear crystal, single-pass conversion efficiency depends on two parameters: pump power and overlap

beam area of fundamental light and SHG light. The conversion efficiency is proportional to the square of pump power and inversely proportional to the overlap beam area. In this chapter, two single-pass configurations based on fiber lasers and PPLN crystals are studied. In order to increase the fundamental power, a Q-switched fiber laser is used at first. PPLN waveguide devices are also used to achieve high conversion efficiency due to the small beam size and high overlap factor between fundamental pump light and SHG light.

3.2 Second Harmonic Generation using an All-Fiber Q-switched Yb-Doped Fiber Laser and a Mgo:PPLN crystal

Visible fiber lasers have attracted a lot of attention recently due to potential applications in the fields of industrial processing, bio-instrumentation, and large screen display. Comparing with the conventional rare earth doped solid-state lasers, the ytterbium (Yb)-doped fiber lasers have strong potential for the systems where air-cooling, long term stability and maintenance-free operation are required. Using Yb-doped fiber lasers and nonlinear crystals to generate green light have already been reported [92 – 94]. Most of these experiments used long nonlinear crystals to achieve high efficiency. But for laser display applications, high repetition rate pulse input is more attractive for SHG process. Because the nonlinear conversion efficiency is proportional to the square of input power, under the same average input power, the SHG conversion efficiency of a pulsed input is much higher than that of a CW input.

3.2.1 All-Fiber Q-switched Yb-Doped Fiber Laser

Compact Yb-doped Q-switched fiber lasers have attracted significant interests as they could be used as high power, high efficiency and low cost sources for many applications. There are different technologies for Q-switch fiber lasers including active Q-switching using piezoelectric modulator [95], electro-optic modulator [96] and acoustic modulator [97], and passive Q-switching using a saturable absorber (SA) in the laser cavity, which offers a much simple design compared to the active Q-switching. Recently, Huang *et al.* reported a passively Q-switched Yb-doped fiber laser with Cr^{4+}: YAG as a SA and achieve a high peak power of 20 kW [98]. However their laser cavity design is complicated. It consists of a Cr^{4+}: YAG slab, three collimating and focus lenses and a mirror. Dvoyrin *et al.* reported pulsed Yb-doped fiber lasers with Bismuth-doped fiber as a SA [99]. They succeeded in Q-switching in a wide wavelength range from 1050 to 1200 nm with a pulse width from 1 to 1.5 μs at a repetition rate from 10 to 100 kHz. Nevertheless, stable pulse operation was only obtained in double-cavity design and the peak power was limited to 40 W at 1064 nm. Fotiadi *et al.* described the dynamics of an all-fiber self-Q-switched Yb-doped fiber laser with a Samarium absorber [100]. Regular pulse operation was observed at discrete pump levels and the dynamics was attributed to polarization mode switching. It appears that though saturable absorbers have been successfully employed in Q-switching solid-state lasers, it is still an interesting research topic to achieve high repetition rate, high peak power Q-switching in Yb-doped fiber laser.

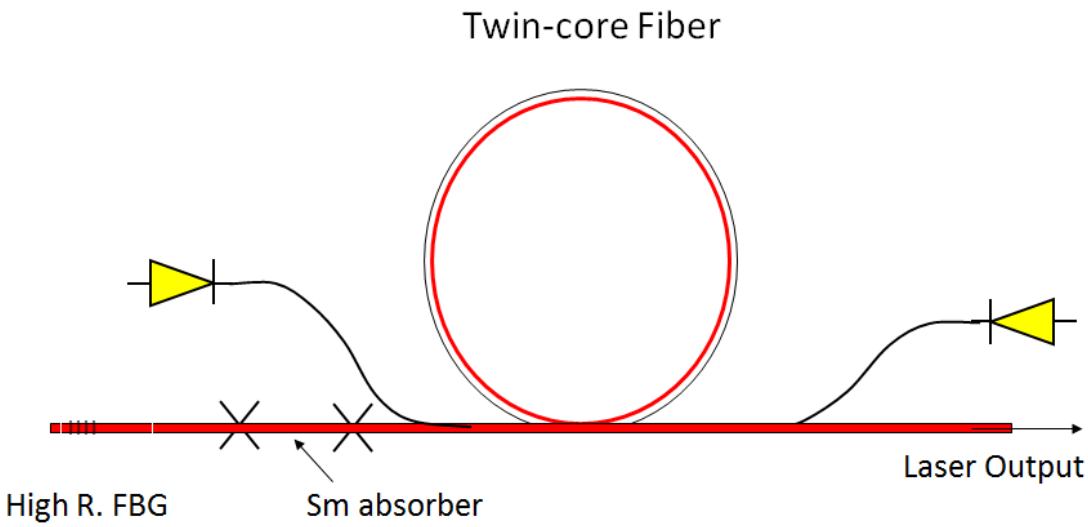

Figure 3.1. Schematic of an all-fiber Q-switched fiber laser design.

The schematic of the fiber laser configuration is shown in Figure 3.1. It consists of two pump lasers of 975 nm to provide bidirectional pump, 10.5 meters of twin-core fiber, a piece of Sm-doped fiber as an absorber and one highly reflective fiber Bragg grating (FBG). The twin-core fiber has two optically contacted large cores, coated with a low refractive index polymer as shown in Figure 3.2. The single-mode Yb-doped active core has a diameter of 6.7 μm and an NA of 0.13. The multimode core has a diameter of 118 μm with a multimode absorption coefficient of 0.77 dB/m at the pump wavelength. The advantage of this coupling method is the ability to increase the output power from the fiber laser by coupling multiple pump sources at both ends, or by exploiting the physical separation between the pump and active paths in which the independent access to the pump path allows for power scaling by adding the pump power along the fiber length. Coupling between two parallel fiber waveguides can be described by interference or

beating of the symmetric and antisymmetric modes of the two-waveguide system. All the energy of the pump core is transferred to the lasing core in half the beat length. This light exchange oscillates along the length of the two-core guiding strcture until all energy is absorbed by the lasing core. The physical mechanism for this crosstalk between two fiber cores is frustrated total reflection. The efficient light coupling between the pump and active cores has been described recently [101]. The single mode Sm-doped SA was obtained from CorAcitve (Sm119) with an NA of 0.14 and a core diameter of 6.3 μm. Its peak absorption near 1064 nm was measured to be 8 dB/m.

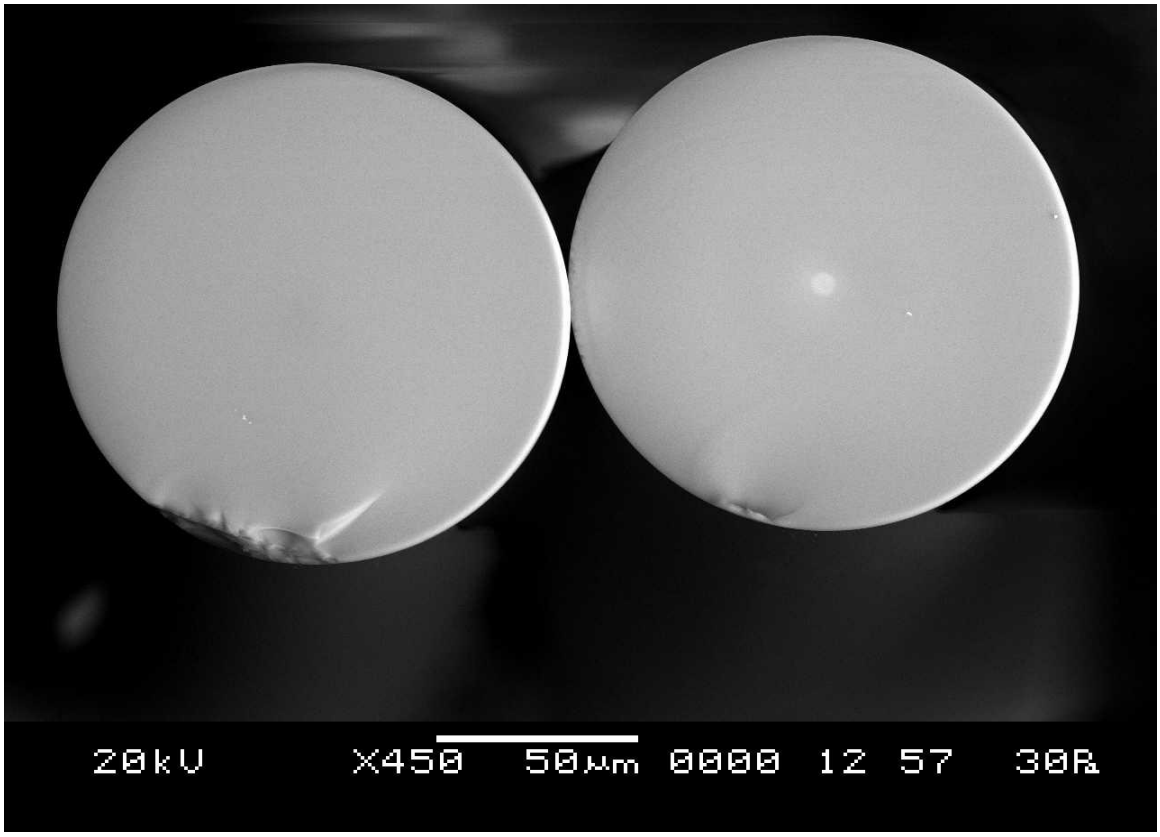

Figure 3.2. SEM image of the cross-section of the twin-core fiber coated with lower index polymer.

We selected Sm-doped absorber for its fast response time [102]. In its near IR absorption band, the lifetime of the upper energy level is less than 5 ns, which is essential to achieve narrow pulse width and high repetition rate in Q-switching.

The pump diode laser has a fiber-coupled output though a multimode fiber of 105/125 μm core/cladding diameter, capable of delivering up to 6.5W of optical power at 975 nm. The high reflectivity FBG was fabricated in house with a reflectivity of > 99.9% and a -3 dB bandwidth of 0.6 nm centered at 1063.37 nm. The cleaved end of the active fiber served as a 4% output coupler.

The temporal behavior of pulse train was recorded with an InGaAs photodiode with a bandwidth of 80 MHz (New Focus, model: 2117) and a digital oscilloscope (Tektronix, model: TKD 3032B). The rise time of the InGaAs photodiode is about 3 ns. Optical spectra were recorded with an optical spectral analyzer (OSA) (Ando Corp. model: AQ-6315E). A power meter (Coherent, model: FieldMaster-GS) was used to measure CW laser power or average power of a Q-switched pulse train.

In our laser configuration, no active cooling was required for all fiber components. Two pump diode lasers were mounted on heat dissipate plates and fiber assembly used a standard anodized aluminum fiber tray mounted on an aluminum metal plate, which separated the electrical and optical compartments in the system. The power supply, providing up to 10A of current, used a conventional fan for convection cooling.

3.2.2 SHG Experiments

Single-pass wavelength conversion by a nonlinear optical (NLO) crystal becomes one of the most attractive methods to generate coherent radiation in various spectral domains from ultraviolet to mid-infrared since QPM was first proposed in the early days of nonlinear optics, especially, after when periodically poling technology became commercially available. Compared with other phase matching methods such as birefringent phase matching (BPM) technique, QPM technique allows us to use the largest nonlinear coefficient over the whole transparent spectral range of the crystal without the walk-off effect.

Among all the periodically poled crystals, periodically poled lithium niobate (PPLN) is one of the most attractive materials due to its large second-order nonlinear coefficient, wide transparency band width covering UV to IR, mature and low cost fabrication process. However, PPLN suffers from pointing instability at medium powers and permanent photorefractive damage at high power. Usually PPLN crystals have to be heated to over one hundred degrees to reduce these effects. This effect can also be reduced by doping some magnesium oxide (MgO) into the crystal during growth. Compared to pure $LiNbO_3$ crystals, 4% - 5% MgO:c-PPLN crystals can increase the resistance against optical damage hundred times higher, which allows devices to work under high input and output power at room temperature [65].

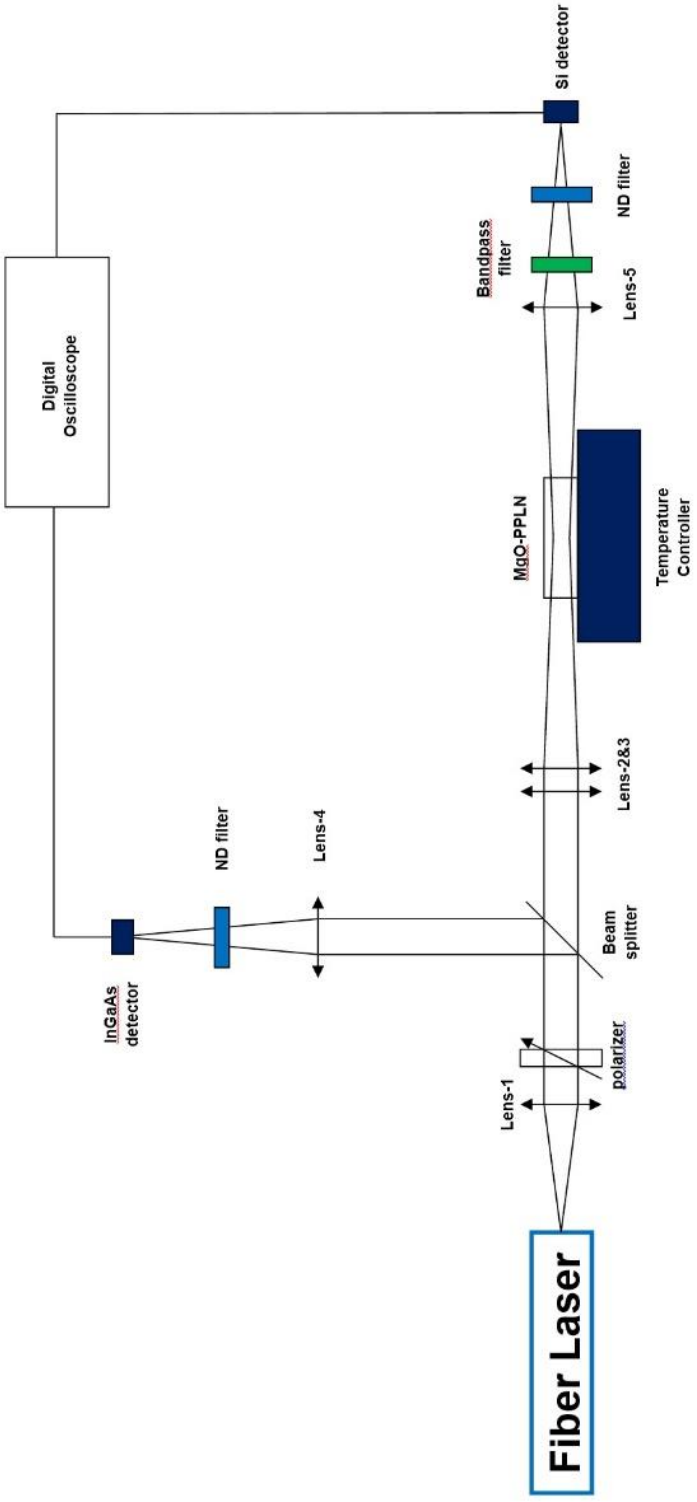

Figure 3.3. Single-pass frequency doubling experimental setup.

The experimental setup is schematically shown in Figure 3.3. Fundamental light from Q-switched fiber laser is collimated by a 10x objective lens (Lens-1). Since only the TM-polarization can satisfy the QPM condition, a polarizer is used to make the fundamental light's polarization parallel with the Z-direction of PPLN. A small part of fundamental light is separated by a beam splitter and focused by Lens-4 onto an InGaAs detector (Thorlabs, model: PDA10CS). The main stream of fundamental beam is focused by two lenses (Lens-2&3). These two lenses can adjust the beam diameter to satisfy the optimum confocal condition for different sample length. In this project, the sample length is 15 mm so the beam is focused to a 50 μm spot radius in the center of the sample.

The sample was mounted in a temperature-controlled oven (Thorlabs, model: TC200) and the temperature was set to 34.5 ℃ which optimized the QPM condition of the sample. SHG light was focused by Lens-5 and a bandpass filter is used to block the fundamental light. A Si detector (Thorlabs, model: PDA10A) is used for the measurement of the pulses trains. Both two detectors were connected to a digital oscilloscope (LeCroy, Model: LT224) for recording the pulse trains. In this way, we can record the fundamental pulses and SHG pulses synchronously in order to accurately compare each other. The responsivities of two detectors were calibrated by two CW DPSS lasers at 1064 nm and 532 nm, respectively.

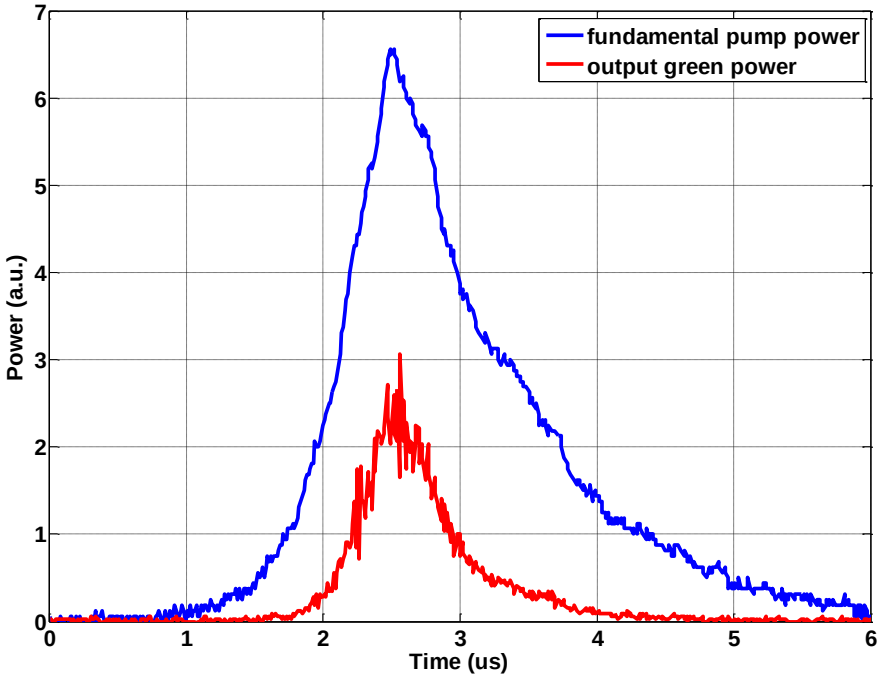

Figure 3.4. Fundamental laser pulse and SHG light pulse.

Figure 3.4 shows the comparison of a fundamental pulse and a SHG pluse. The fiber laser used in SHG experiments is connected with 0.45m Sm-absorber, so as describe before, the fundamental pulse width is about 1.1 μs. Because the SHG power is proportional to the square of fundamental pulse, the SHG pulse FWHM width should be 0.707 of the fundamental pulse. As shown in the Fig.3.4, the SHG pulse width is about 0.75 μs.

Figure 3.5 shows the output spectrum of SHG light at 531.64 nm. The -3dB bandwidth is about 0.09 nm which is slightly narrower than that of the fundamental light at 1063.25 nm.

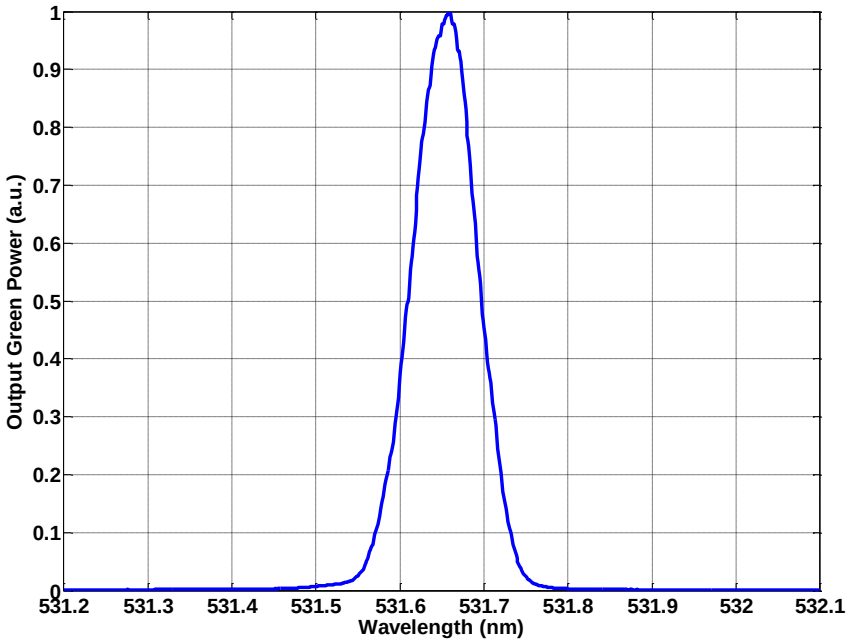

Figure 3.5. Spectrum of output SHG laser.

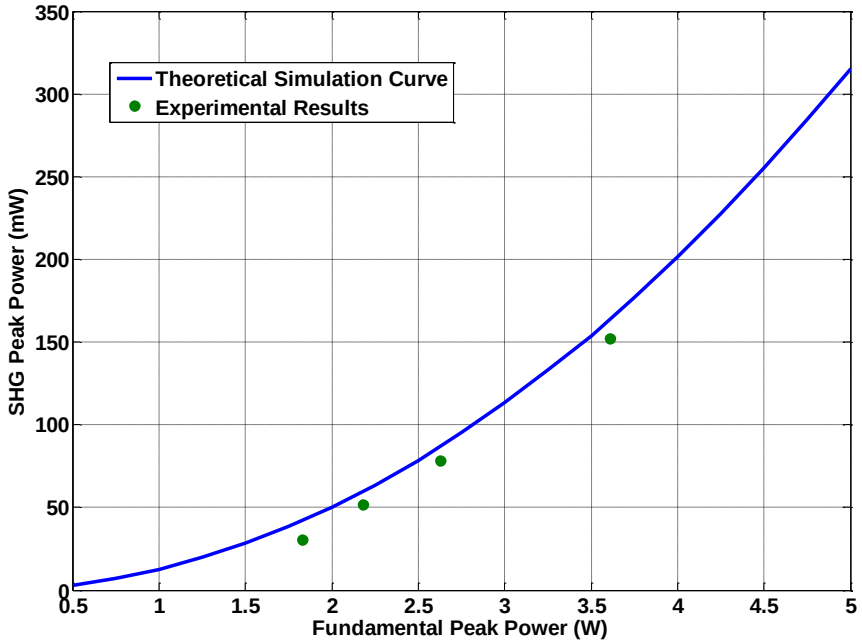

Figure 3.6. SHG Peak Power versus Fundamental Peak Power.

The SHG peak power is plotted against the incident fundamental peak power as shown in Figure 3.6. The SHG peak power of 152 mW was achieved when the fundamental peak power was 3.6 W (average power is 1 W). The conversion efficiency (SHG pulse power / fundamental pulse power) was 4.2% which agrees with the theoretical simulation result. The conversion efficiency can be expected to be above 90% when the input fundamental peak power is in kW level.

3.2.3 Discussion and Conclusion

We have demonstrated an all-fiber, high repetition rate and high peak power passively Q-switched Yb-doped fiber laser using Sm-doped fiber as an SA. With a pump power of 8.4 W, the fiber laser output stable pulses with a pulse width of 1.1 μs at a repetition rate of 250 kHz, producing a peak output power of 3.4 W. All fiber connections were fusion spliced and fiber was looped in a $15 \times 12 \times 0.8$ cm^3 compact fiber tray. This laser design showed significant improvement as compared with other Q-switched fiber lasers and has the following features: (a) All fiber components were splice connected that avoided the use of any bulk optics; (b) Realized bi-directional pumping using a twin-core fiber that separated pump path from the active signal path; (c) Demonstrated high repetition rate in the order of 200 kHz.

Using this novel fiber laser and an MgO-PPLN wavelength conversion device, we have obtained the green laser with peak power of 150 mW at room temperature. The conversion efficiency is 4.2% which agrees well with the theoretical value. The MgO:c-PPLN sample is 15 mm long and the temperature is controlled at 34.5 ℃ to satisfy QPM

condition. The conversion efficiency would be higher if we can achieve high peak power for fundamental light form fiber laser. Further increasing the peak power is currently limited by the non-linear effects in fiber laser and will be improved by the use of larger core active fiber. The all-fiber configuration provide a simple, low cost and easy manufacturing solution for high power Q-switched pulse laser that should be attractive to micro-machining, medical treatment and other applications. Because Q-switched fiber lasers can provide high beam quality with low amplitude noise. The fiber lasers are more ease of cooling in long fiber for high power applications. Moreover, the all-fiber configuration has high stability and reliability. Compared to the intra-cavity frequency doubling structure, green laser based on the single-pass configuration and fiber lasers can generate high quality green beam with low noise and narrow bandwidth, which is attractive to many medical applications.

3.3 Green Laser Generation based on MgO:PPLN Ridge Waveguide

In order to achieve strong SHG, the interacting fields of the fundamental and second harmonic wave should be well confined and overlapped inside the structure. A nonlinear waveguide present a way to achieve high conversion efficiency at fairly low power levels because it makes it possible to maintain a small mode area (high intensities for a given power level) over a greater length than in a bulk medium,

Fabricating high quality optical waveguide on lithium niobate crystals has attracted intense interests in the past decades due to its good prospection in many applications such

as wavelength converters and high-speed modulators. Periodically poled lithium niobate waveguides are of great interest in generating green laser by QPM SHG because of the combined advantages of a large nonlinear coefficient, high power intensity and enhanced nonlinear interaction length.

3.3.1 Annealed Proton-Exchanged MgO:PPLN Ridge Waveguide

Although the fabrication techniques of semiconductor optical waveguide are quite mature, fabrication of high quality lithium niobate waveguides has always been a challenging topic over the past decades. Due to the material properties, dry etching and wet etching techniques are not suitable for fabricating lithium niobate waveguide. But traditional ion doping fabrication techniques including titanium in-diffusion or annealed proton-exchange are not suitable for high power SHG operation. Ti in-diffused waveguides suffer from severe photorefractive damage, which deteriorates the waveguide characteristics under high power density [41]. Although APE method has largely solved the issue, the achievable SHG efficiency and power of is still limited due to the weak light confinement of APE channel waveguides [103]. Nevertheless, APE method still remains a popular way of making $LiNbO_3$ waveguides today, for its convenient and matured fabrication techniques.

In recent years, wafer bonded $LiNbO_3$ ridge waveguides have attracted more and more attention for their ability to provide strong light confinement as well as low propagation loss [104, 105]. The fabrication procedure mainly consists of $LiNbO_3$ wafer bonding, wafer grinding and polishing, and precise diamond blade dicing. Successful

results have been found in green, blue, UV and mid-infrared generations. However, several issues still remain with the wafer bonded waveguides. First, an additional $LiNbO_3$ or $LiTaO_3$ wafer is needed to carry out the bonding, as a supporting substrate, which increases waveguide material costs. Second, during grinding and polishing, the PPLN wafer has to be reduced to about 1% of its original thickness with sub-micron thickness control accuracy, which is challenging, and adds to the process complexity. Third, bonding strength between the ridge waveguide and the supporting substrate may deteriorate over time, due to different thermal expansion coefficients, and the residual stresses caused during wafer thinning. Such deterioration may cause waveguide peel-off, and provide a threat to device stability.

By combining the advantages of both APE and precise diamond blade dicing method, a novel APE MgO:PPLN ridge waveguide structure has been developed in our group. As shown in Figure 3.7, the vertical light confinement is achieved by APE method, while lateral confinement is accomplished by precise diamond blade dicing. By combining the advantages of both APE and precise matching techniques, this ridge waveguide structure features a greatly simplified fabrication process and high conversion efficiency simultaneously.

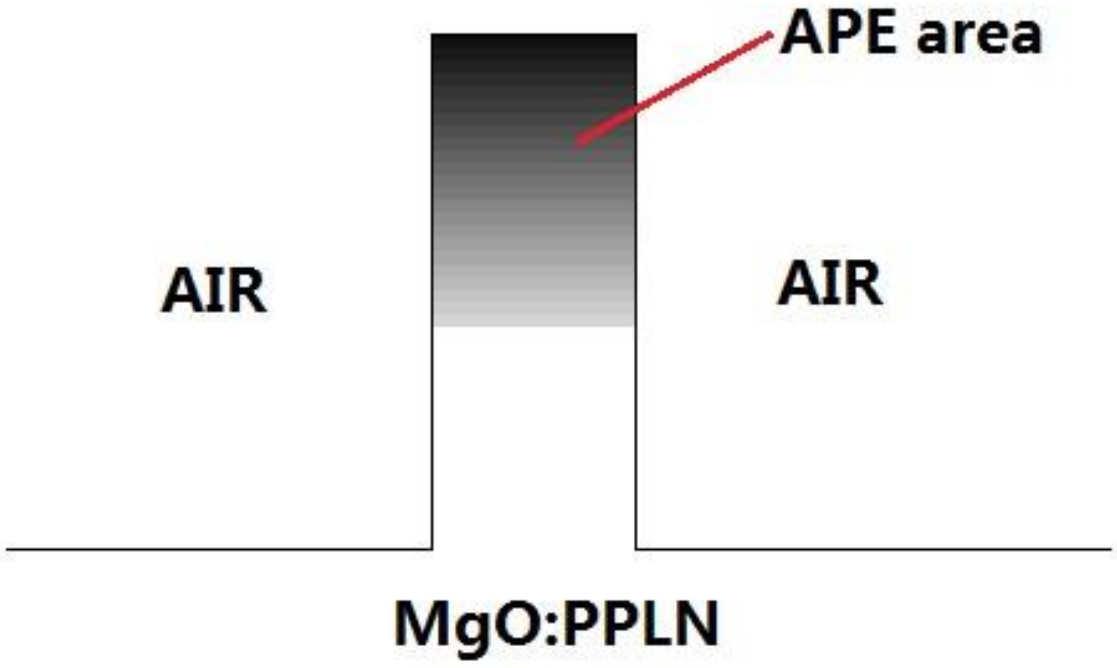

Figure 3.7. A schematic diagram of APE MgO:PPLN ridge waveguide cross-section.

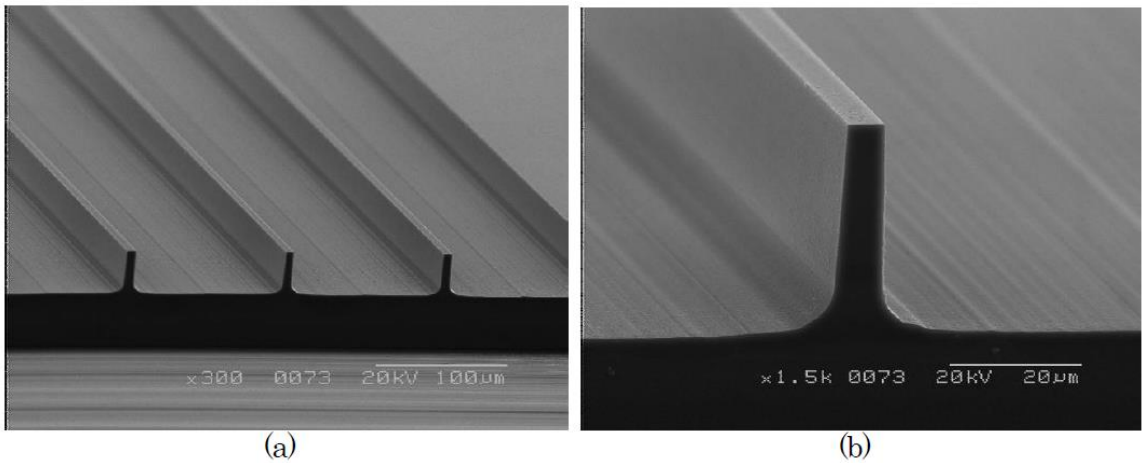

Figure 3.8. SEM photo of a ridge waveguide chip.

Figure 3.8 shows the SEM image of a fabricated waveguide chip, showing three ridge waveguides. In order to achieve low loss waveguide with single transmission mode, the proton-exchange condition, annealing time and the ridge width must be optimized.

3.3.2 Linearly Polarized Yb-doped Fiber Laser

Quasi phase matched second harmonic generation is a polarization depend nonlinear process. In order to achieve high overall conversion efficiency, high power, single-polarization fiber lasers are necessary for single pass PPLN SHG. These lasers should possess a stable output with a narrow bandwidth, high extinction ratio and high optical signal-to-noise ratio.

Various fiber laser configurations have been proposed in the last few years. Walton et al. reported a fiber laser with an extinction ratio of 20 dB using a Polarization Maintaining (PM) Yb-doped double-cladding active fiber and a Single-Polarization (SP) fiber for polarization selection [106]. Although SP fiber was very effective in polarization discrimination; its elliptical core had introduced a 1.3 dB loss when spliced to the active fiber with a circular core. The bandwidth of the laser was not reported. Liu et al. reported a high power single-polarization fiber laser using tightly coiled high-birefringence large-mode-area fiber to select a single polarization, and achieved an extinction ratio of 19 dB [107]. The bandwidth of the laser output was about 1.9 nm, rendering it too broad for SHG. Shirakawa et al. used two cross-spliced fiber Bragg Gratings (FBG), inscribed on PM fibers, to form the laser cavity and achieved an extinction ratio of 18 dB and a bandwidth of 20 pm [108]. However the laser requires a temperature controller for its

output coupler FBG for wavelength matching and has a narrow operation temperature range of 8 ℃, within which a stable output was obtained. All fiber lasers described above used bulk optics to couple the pump light into active fiber and to couple the laser emission out. The use of bulk optics and temperature controller would significantly complicate the package design and make it challenging to maintain a stable laser output and therefore are not truly all-fiber designs.

An all-fiber design using GT-Wave fiber was reported by Paramonov et al., in which two FBGs, one inscribed on a PM fiber as a highly reflective mirror and the other on a single-mode fiber as an output coupler, were fusion spliced to a non-PM Yb-doped fiber [109]. The polarization selection was realized by aligning the wavelength of the output coupler FBG to one of two PM FBG wavelengths. An extinction ratio of 17 dB and a bandwidth of 70 pm were obtained, respectively. An in-line polarization controller was required that made the laser susceptible to any environmental change. Recently a single-polarized fiber laser in an all-fiber configuration was reported with the laser cavity made of a FBG inscribed on a SP fiber as a high reflective mirror and a piece of end-cleaved SP fiber as an output coupler [110]. The fiber laser achieved a polarization extinction ratio of 700:1 or 28 dB, an optical signal- to-noise ratio of 70 dB and a narrow bandwidth of 54 pm at 1.7 W of output. However, the splice loss at the splicing point, resulting from the mismatching between the elliptical core of the SP fiber and circular core of the PM active fiber, caused the heat building up, which prevented this laser from further scale up the output power beyond 3.0 W. Clearly, it is still necessary to find a better fiber laser design to overcome the drawbacks listed above.

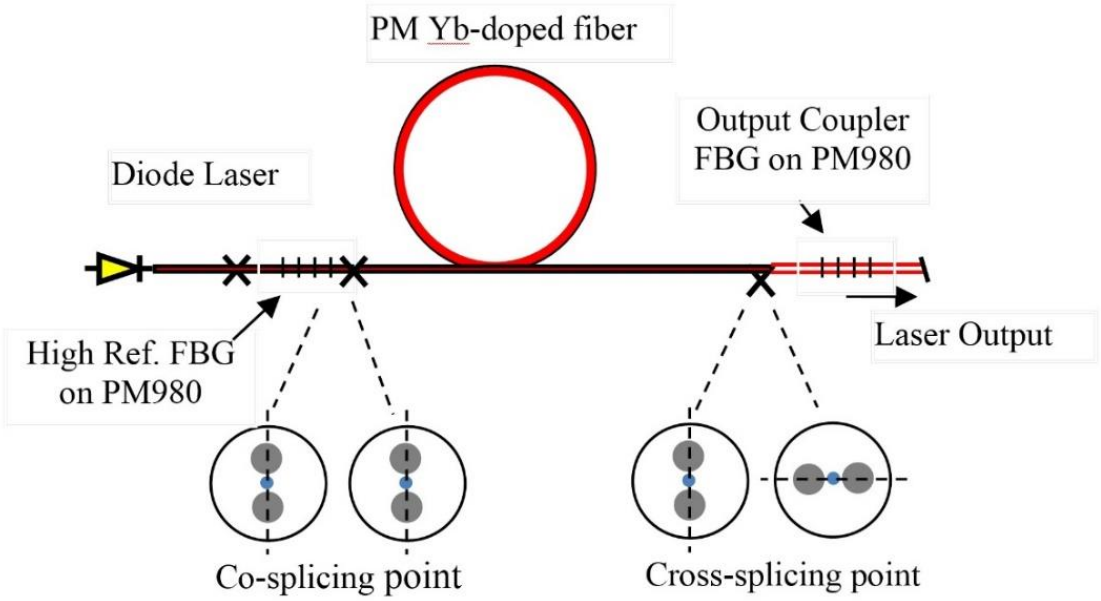

Figure 3.9. A schematic diagram of the polarized Yb-doped fiber laser.

In order to build a single pass green fiber laser with high overall conversion efficiency, an all-fiber laser design in order to achieve high power, high extinction ratio narrow bandwidth and very stable power output is developed. The schematic diagram of the fiber laser, with all fiber connections fusion spliced, is shown in Figure 3.9. A diode laser with a multimode fiber output of 10 W was used as a pump source. A PM single-mode Yb-doped double-cladding fiber of 5 m long, with a core diameter of 5 μm and an NA of 0.13, was used as an active fiber (Nufern: PM-YDF-5/130). The fiber has a quoted multimode absorption coefficient of 0.65 dB/m at 915 nm; so its absorption at 975 nm is estimated to be of 1.96 dB/m. The highly reflective FBG, written on the PM980 fiber, has one end spliced to the multimode output fiber of the pump laser and the other end of the

FBG was spliced to the PM active fiber with its axes aligned as shown in Fig.1. The buffer of the FBG fiber of about 20 cm was stripped so the pump laser can propagate in its cladding. The weak reflection FBG was cross-spliced to the other end of the active fiber as an output coupler of the laser.

In this FBG cavity design, the highly reflective FBG was written on a piece of PM980 fiber with its FBG wavelength at fast axis, λ_{Hf} =1063.45 and slow axis, λ_{Hs} =1063.71 nm, respectively. The FBG has a flat-top bandwidth of 0.18 nm, defined as the bandwidth at -0.5 dB from its maximum reflectivity of 99.5%, as shown in Fig. 1. The output couple FBG, also made on PM980 fiber, has a reflectivity of 10% with its slow axis FBG wavelength at λ_{OCs} =1063.42 nm, almost matching the center of the flat-top band of the highly reflective FBG at fast axis as illustrated in Fig. 3.10. This cavity has two features that are different from previous reported configuration. One is the flat-top reflective FBG to ensure that its wavelength always matches that of the output coupler. The other is the fast roll off of the highly reflective FBG on slow axis to ensure a high isolation between the λ_{OCs} and the tail of λ_{Hs} reflection peak.

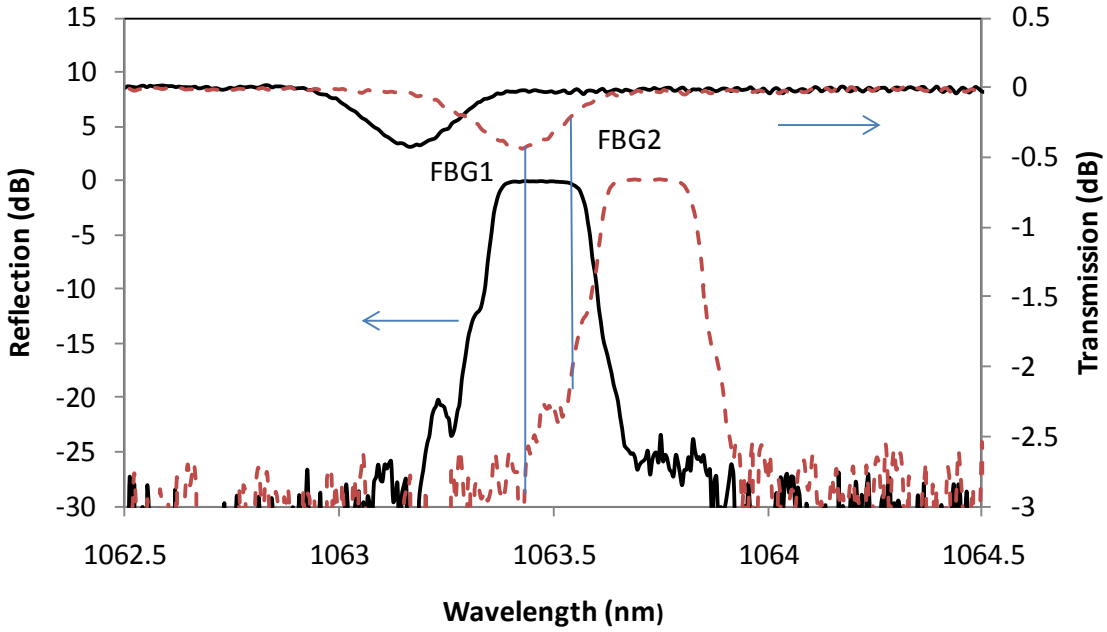

Figure 3.10. The transmission spectrum of the output coupler FBG and the reflection spectrum of the strong FBG (solid lines: fast axis FBGs; dash lines: slow axis FBGs).

The highly reflective FBG was spliced to the PM active fiber with both their fast and slow axes aligned, using a PM fusion splicer (Fujikura, Model: FSM-20PM II). However the output FBG was spliced to the PM active fiber with its slow axis aligned to the fast axis of the PM active fiber. Thus, the highly reflective FBG at fast axis formed a cavity with the output coupler FBG at slow axis to support only one polarization for laser operation.

3.3.3 SHG Experiments

Using an APE MgO:PPLN ridge waveguides and an All-fiber linearly polarized Yb-doped fiber laser, considerable conversion efficiency can be achieved through a

simple and compact single pass QPM SHG configuration. As shown in Figure 3.11, light is coupled out from the linearly polarized fiber laser. The output fiber is mounted on a rotational stage and the polarization direction is aligned with the z-axis of the MgO:PPLN crystal. The APE MgO:PPLN ridge waveguide samples are placed on a temperature-controlled copper plate with 0.1 ℃ temperature control accuracy. Fundamental 1064 nm laser is converted into 532 nm green light after single passing through the ridge waveguide. The output light is focused by an objective lens into a power meter. The total laser power and green light power are measured without/with a green filter.

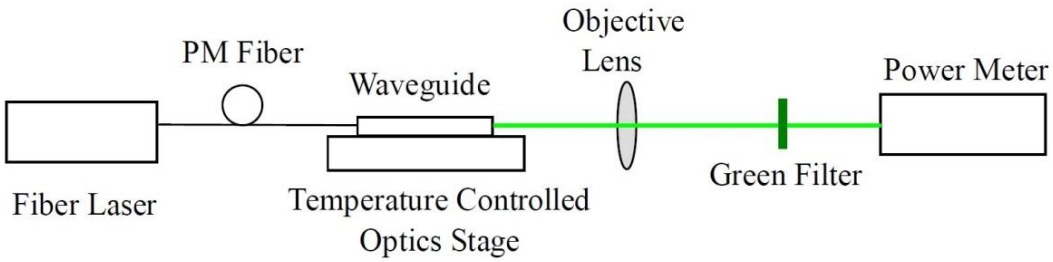

Figure 3.11. A schematic diagram of the SHG experimental setup.

Waveguides with ridge width of 6, 8, and 10 μm are employed in the experiments. The measured SHG output power and conversion efficiency of different ridge width waveguides are shown in the following figures. Power loss caused by the focusing lens and filter has already been compensated.

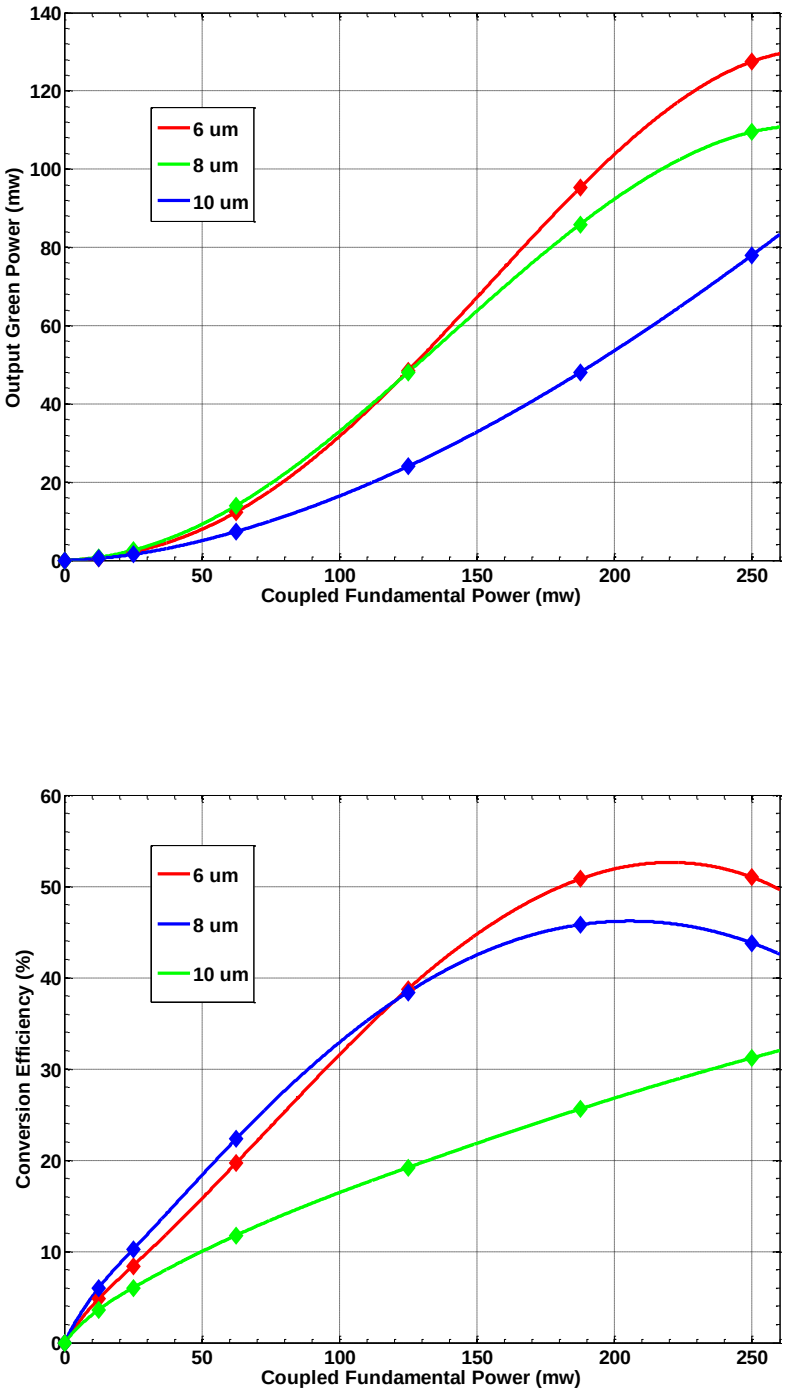

Figure 3.12. Coupled fundamental power and conversion efficiency versus SHG output power.

The 6 μm wide waveguide has demonstrated more than 125 mW green output power with the highest optical-to-optical efficiency of 53.2%. Conversion efficiency of waveguides with 4, 6, 8 μm width is significantly higher than 10 and 12 μm wide waveguides due to the higher power density and better mode overlap between fundamental light and SHG light in narrow waveguide. The waveguide output beam profile is measured by a CCD camera. In the 6 μm wide waveguide, the near-field mode profiles of fundamental 1064 nm and SHG 532 nm light are almost matched with each other.

(a-1)

(b-1)

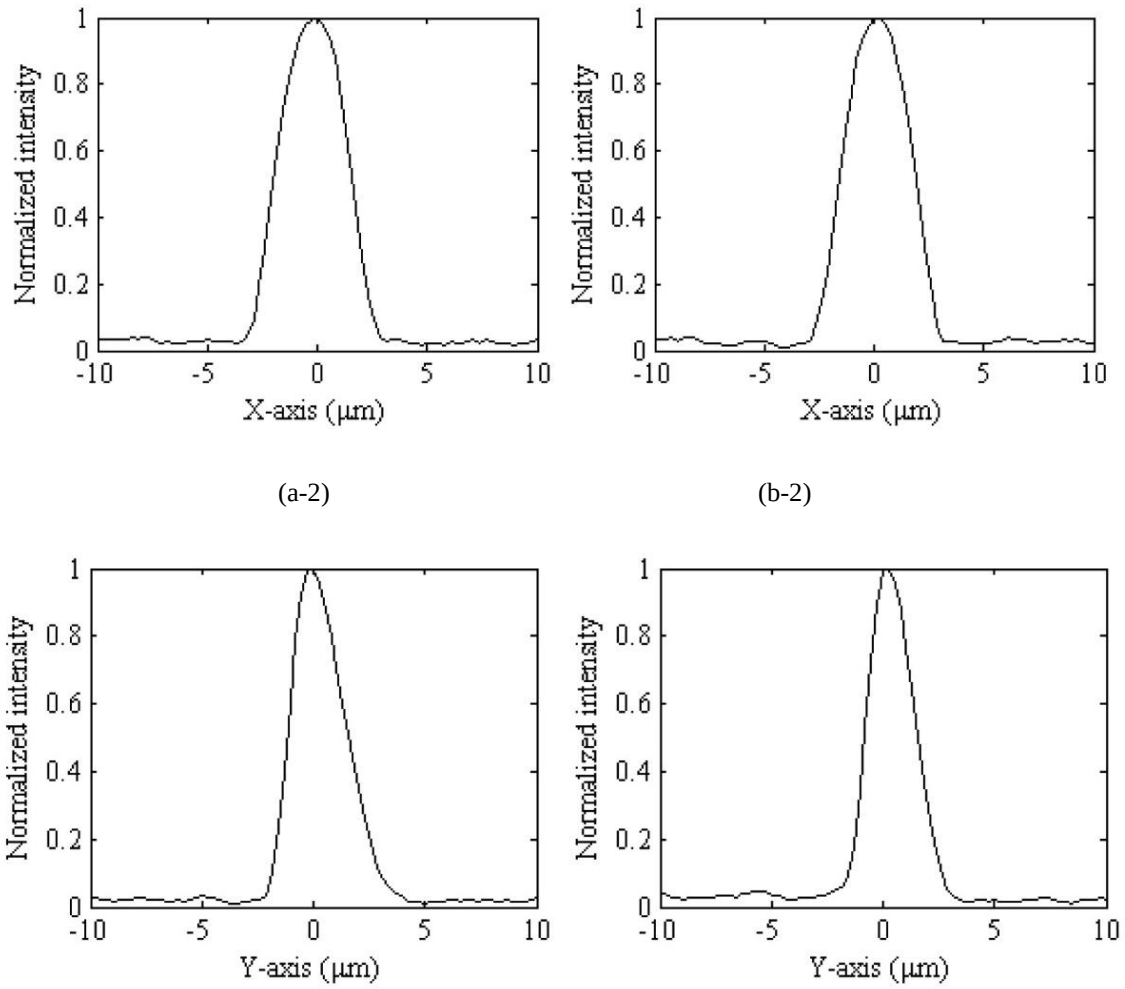

(a-2) (b-2)

(a-3) (b-2)

Figure 3.13. Mode profile of fundamental light (a) and SHG light (b) output from a 6 μm wide APE MgO:PPLN ridge waveguide.

3.3.4 Discussion and Conclusion

As shown in the output performance figures, the conversion ability for the waveguides with higher efficiency (6 and 8 μm wide) begins to cease under pumping power higher than 150 mW, and the green output power significant decreased with more

than 200 mW pumping. We conclude this phenomenon is mainly due to the heat generation insider the waveguide under high pumping power. The power density inside a 6 μm APE ridge waveguide is more than 0.6 MW/cm^2 with 200 mW total laser power. Since the thermal conductivity of $LiNbO_3$ is less than 4 W/mK, heat dissipation becomes very difficult. The APE ridge waveguide height is only several microns, but it is built on a 500 μm thick crystal. The temperature controller cannot precisely adjust the temperature inside the waveguide through a medium 100 times thicker from the bottom side. From the top side, although natural convection can take away a large quantity of heat, but it easily caused non-uniform temperature distribution over the long waveguide. Improving temperature uniformity across the whole chip and cutting down thermal resistance between waveguide and controller are proper measures to achieve better performance.

In conclusion, over 120 mW green laser output with 53.2% conversion efficiency is achieved by a simply and compact single-pass SHG configuration including a novel APE $LiNbO_3$ ridge waveguide which is successfully fabricated by combining annealed proton-exchange and precise diamond blade dicing. An all fiber linearly polarized Yb-doped fiber laser is developed as the fundamental pump source. Higher green output and conversion efficiency can be expected by improving the thermal management of the waveguide device.

CHAPTER 4

GREEN LASERS BASED ON INTRA-CAVITY FREQUENCY DOUBLING

4.1 Introduction

Although it is the most straightforward method to convert infrared laser to visible green laser, single-pass frequency doubling has an obvious disadvantages for laser display applications: high conversion efficiency relies on either a long nonlinear crystal or using high pump power. Longer nonlinear crystals are used, the temperature and wavelength acceptance are narrowed and possibly induce a thermal de-phasing effect. While high pump power brings more complexities into the system, such as thermal management and damage consideration of optical elements and surface coating.

Laser display applications require light source to be compact, low cost and robust. At current stage, using intra-cavity frequency doubling technique with diode-pumped solid state lasers is a more practical solution. In this chapter, research efforts on building a green laser based on intra-cavity frequency doubled Nd:YVO_4/MgO:PPLN DPSS laser configurations are presents.

4.2 Compact Nd:YVO_4/MgO:PPLN Microchip Green Lasers

Microchip lasers are alignment-free monolithic solid-state lasers where the resonator mirrors are directly coated or contacted with the laser crystal [111]. Intra-cavity frequency doubled microchip lasers are the smallest and least expensive visible solid state lasers. The combination of high performance and low cost makes microchip lasers attractive for many applications including optical communications, optical storage, medicine, and laser display.

Intra-cavity frequency doubled microchip lasers consist of a laser crystal and a nonlinear crystal which are polished and optically bonded together with parallel outside surfaces to achieve the simplest structure and assembly. Nd:YAG and Nd:YVO_4 are the most commonly used gain materials in monolithic and composite microchip lasers. While the potassium titanyl phosphate (KTP), potassium niobate ($KNbO_3$) and lithium triborate (LBO) are the most popular frequency doubling crystals. Nd:YVO_4/KTP green microchip lasers have been developed for years and widely used in many low power applications such as laser pointers [112, 113]. However, commercial Nd:YVO_4/KTP green microchip lasers can only be used with an output power less than 100 mW, which mainly due to the limitation of the bonding strength between of two crystals and the low conversion efficiency of KTP crystals. Unfortunately, most laser display applications require more than 100 mW output power of green lasers. To overcome the deficiencies encountered by Nd:YVO_4/KTP microchip green lasers, Nd:YVO_4/MgO:PPLN microchip green lasers have been recently developed, in which more efficient MgO:PPLN crystals are employed

[114, 115]. The structure of Nd:YVO_4/MgO:PPLN microchip green lasers is described in this section. The green lasing performance and temperature characteristic are investigated. The existing problems of Nd:YVO_4/MgO:PPLN microchip green lasers are also discussed.

4.2.1 *Structure and Experiments setup of Microchip Green Lasers*

As shown in Figure 4.1, the miniature Nd:YVO_4/MgO:PPLN microchip employed in our experiments consists of a 3 at.% Nd-doped Nd:YVO_4 crystal and a 5% MgO doped PPLN crystal with 7 μm period. The width and thickness of the two crystals are 2.1 mm and 0.5 mm respectively, and were decided by fabrication processes. The length of Nd:YVO_4 is 1 mm as calculated by the absorption coefficient of 808-nm pump light. The MgO:PPLN crystal is also 1 mm long. The shorter the length of the QPM nonlinear crystal is, the wider the working temperature range will be, but the conversion efficiency will become lower. We designed the MgO:PPLN length of 1 mm considering the compromise of the working temperature tolerance and conversion efficiency. The coating of the input facet of the Nd:YVO_4/MgO:PPLN crystal had high reflectivity (R>99.8%) at both 1064 nm and 532 nm, and high transmission at the 808 nm pump wavelength. The output facet of the crystal had a high reflection coating for 1064 nm and anti-reflection coating for 532 nm. All these optical coating is based on multi-layer interference principle which using alternating layers of a low-index material and a higher-index material to obtain designed reflectivity. Figure 4.2 shows two photographs of Nd:YVO_4/MgO:PPLN

microchip. The microchip has a size of only 2(L)×2.2(W) ×0.5(T) mm^3 (i.e. 0.0022 c.c.). The size of green laser based on this microchip could be less than 1 c.c. at a very low cost.

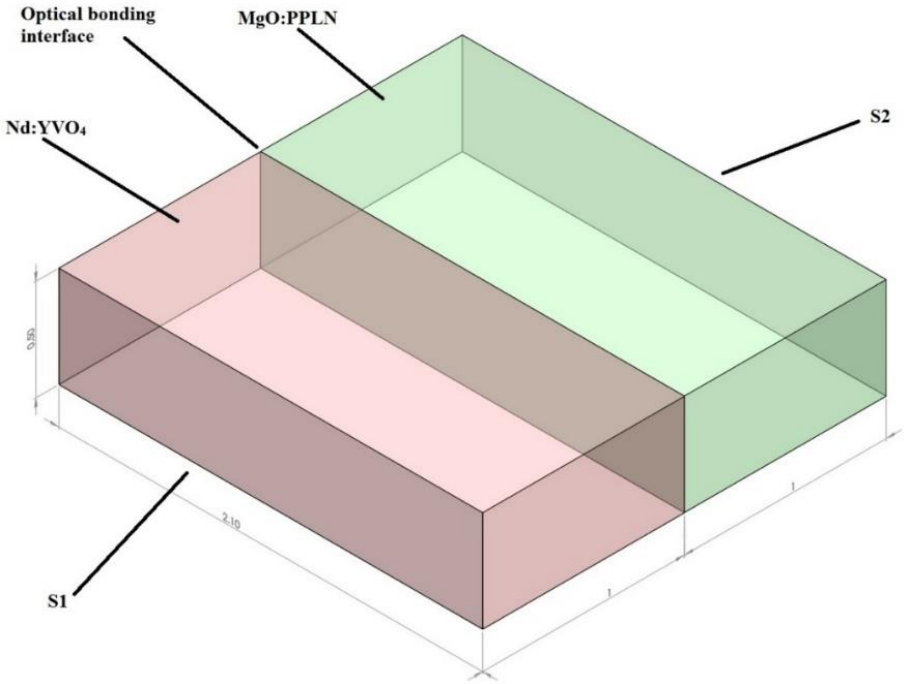

Figure 4.1. Schematic structure of the Nd:YVO_4/MgO:PPLN microchip.

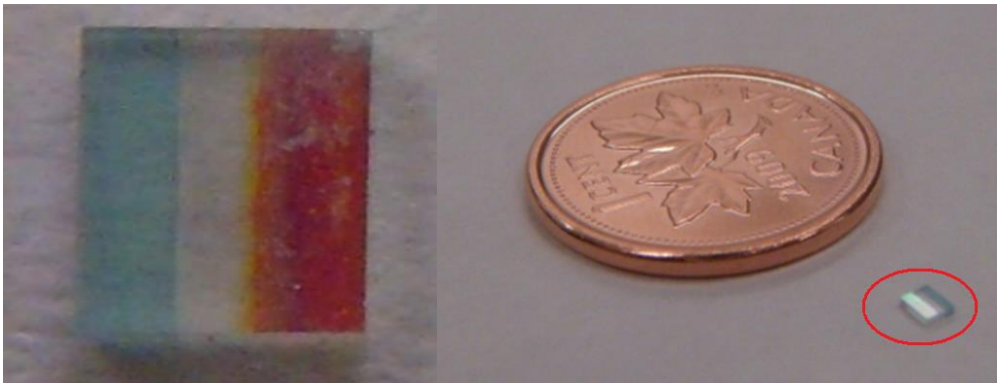

Figure 4.2. Photograph of the Nd:YVO_4/MgO:PPLN microchip.

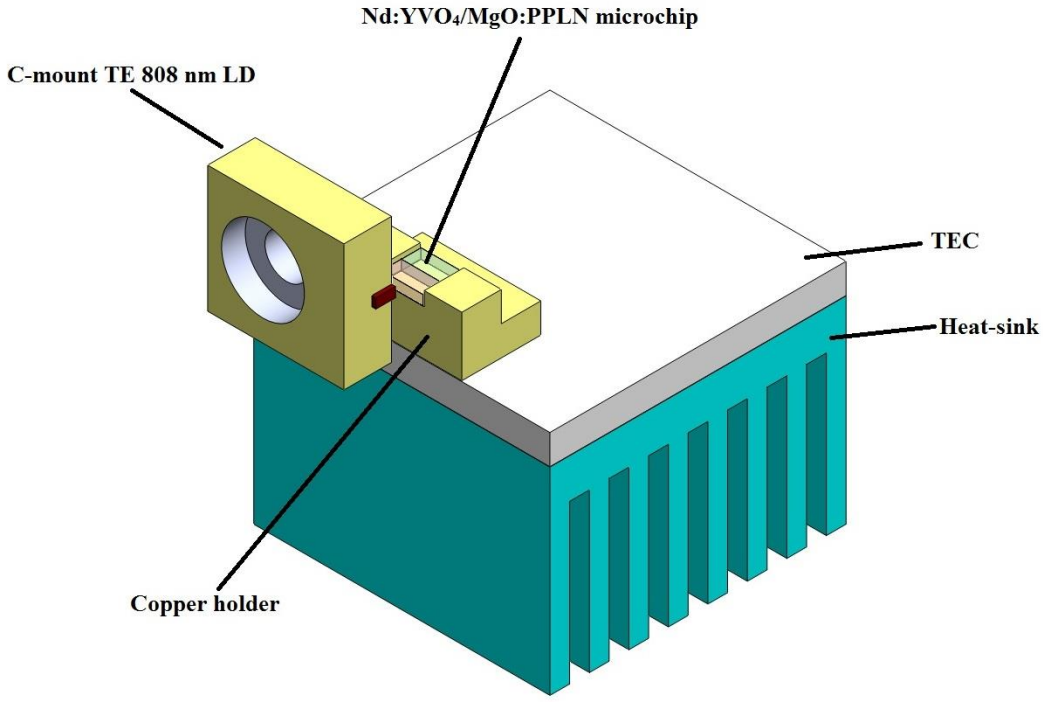

Figure 4.3. Experimental setup for the green microchip laser.

Figure 4.3 shows the experiments setup for performance evaluation. The pump source used in the experiment is a standard broad stripe TE polarized C-mount 808 nm pump LD. Since the absorption coefficients of two optical axis of Nd:YVO_4 crystals are different, to achieve the best performance of the microchip, the pump LD should be rotated by 90 º. If the LD emits TM polarized light, this rotation is not necessary. In order to obtain high efficiency and good beam quality. the pump diodes used in the experiments are all fast axis collimated (FAC) LDs. Usually a FAC-LD has a beam divergence of ~ 7 º in both vertical and horizontal direction, which can result a square shaped beam. If more complicated lens are employed for pump beam reshaping and focusing to improve the mode overlap between pump beam and intra-cavity laser beam, the performances of the

microchip can be further enhanced in terms of output power, beam quality, and conversion efficiency. Although in the microchip, the Nd:YVO_4 crystal and the MgO:PPLN crystal are pre-aligned during the fabrication process, the alignment between the pump LD and the microchip is still very important for performance optimization. The Nd:YVO_4/MgO:PPLN microchip is placed in a copper holder which mounted on a small TEC to control the temperature of crystals. Good thermal contract between the microchip and the holder is essential to eliminate of pump heating effects.

4.2.2 *Results and Discussion*

The initial target of Nd:YVO_4/MgO:PPLN microchip experiments is to achieve over 100 mW output power. The pump source used during experiments is a standard broad-stripe 2-W LD. The microchip samples are placed on the copper holder. A standard thermal compound grease filled the gap between the microchip and copper holder to improve the thermal conductivity during experiments.

Figure 4.4 shows the lasing performance of the microchip in one of our experiments. Up to 120 mW of green power was measured with 560 mW pump power at CW operation mode. A clear circular shaped beam is obtained as well. But when further increase pump power, the output green power trends to saturate and then significant decreases. We conclude this phenomenon is mainly due to the heat dissipation of the optical bonded structure is not superior to the traditional separated structure. Much heat generated in the Nd:YVO_4 (about 40% - 50% of the pump power) could not be extracted

out efficiently and quickly at high pump power, and then the heat is transferred to the bonded MgO:PPLN crystal. This will deteriorate the QPM condition greatly. An elliptical multimode output beam is observed with increasing pump power because of the uniaxial nature of the crystal and the unequal thermal coefficients in two directions perpendicular to the axis of the microchip.

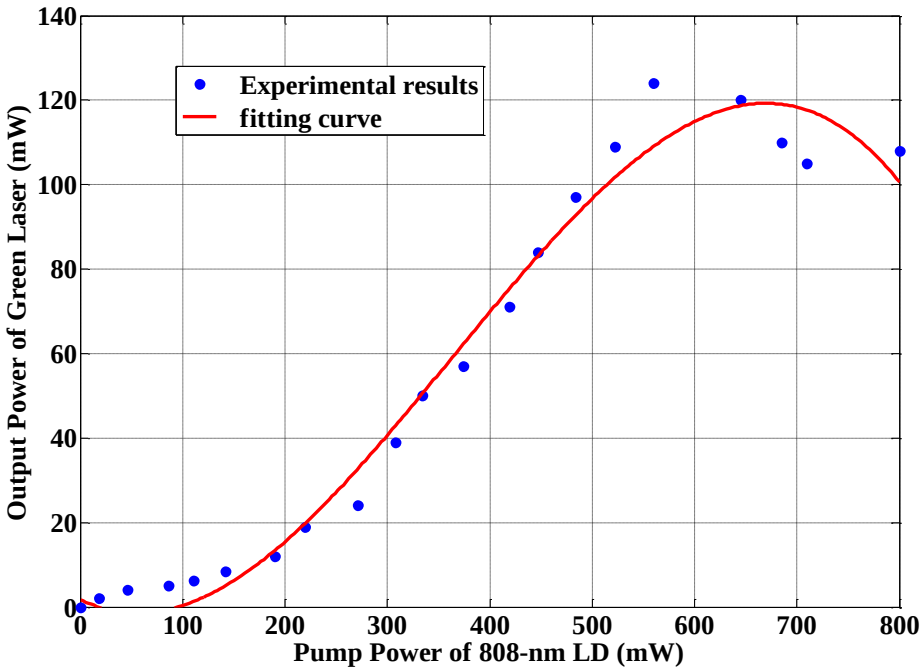

Figure 4.4. CW performance of the microchip green laser.

In order to improve device performance under high pump power, a better and more uniform thermal conductivity is necessary. As shown in shown in Figure 4.5 (a), the perfomance curve shown in Figure 4.4 was achieved by simply attaching the device with the copper holder with thermal compound. Then, in order to improve the uniformity of

thermal conducitity, as shown in Figure 4.4 (b) the microchip is wrapped with indium foil and clampped by the copper holder. A copper cover is mounted on the upside of the device.

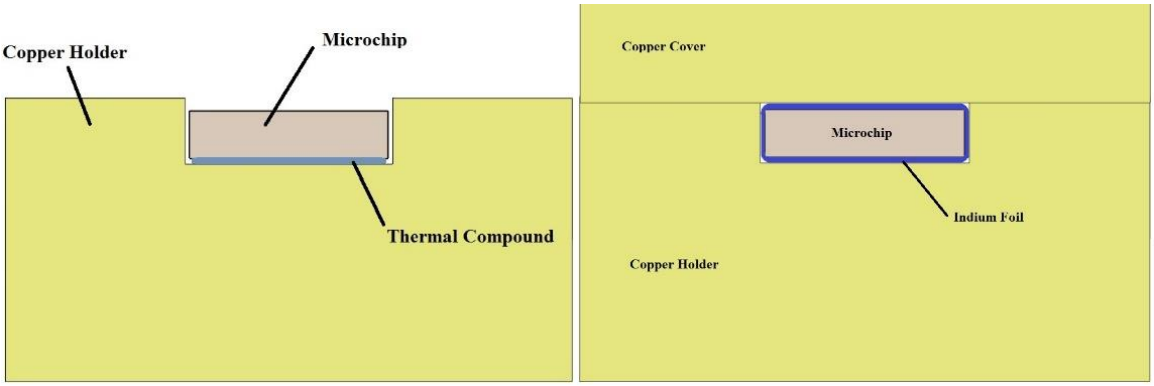

(a) (b)

Figure 4.5. Packaging evolution of the microchip green laser.

A finite element simuation is empolyed to investigate the difference between above two type package. As shown in Figure 4.6 (a), for the original packaging structure, the thermal distribution in the microchip is asymmetric. A lot of heat in the upper side of the Nd:YVO_4 crystal can not be extracted quickly and start to transfer to the MgO:PPLN crystal. In contrast, as shown in Figure 4.6 (b), using modified packaging structure, the heat in the laser crystal distributes more uniform and less of them is transferred into the nonlinear crystal.

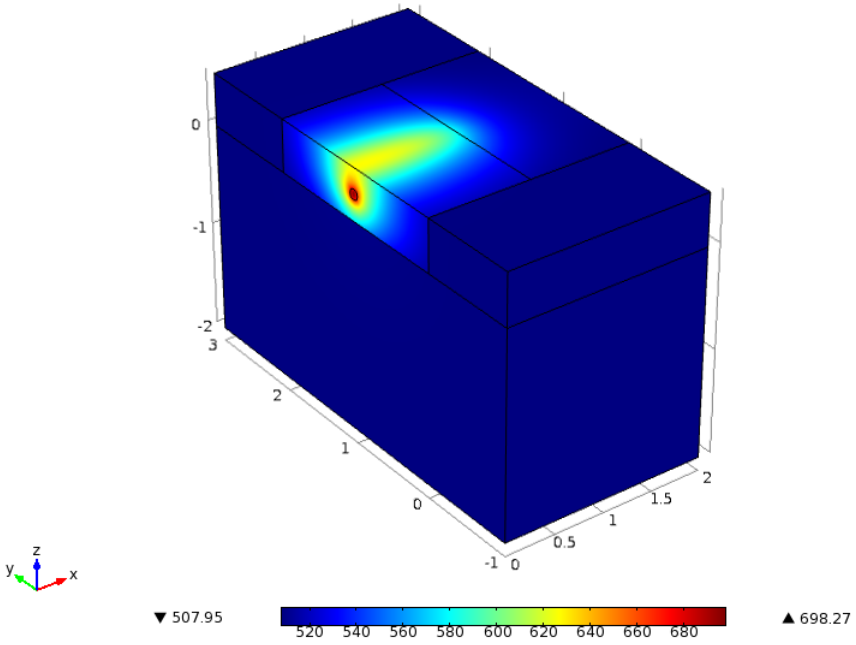

(a)

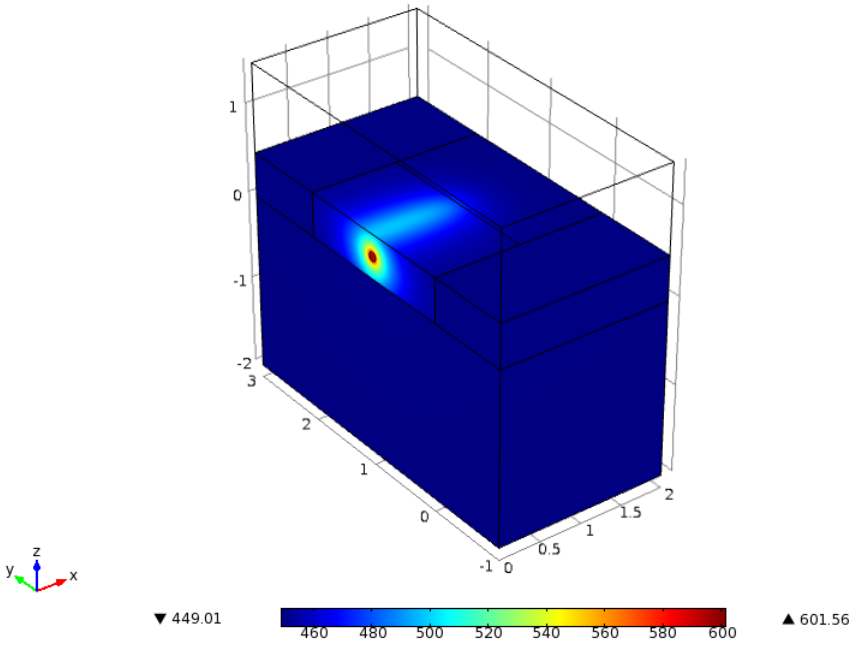

(b)

Figure 4.6. Finite element simuation of heat distribution in two packages.

The lasing performance of the microchip with modified package is shown in Figure 4.7. The improvement is obvious. The output power increases along with the increasing of pump power until 1.5 W. The beam shape keeps circular. Maximum 290 mW green power is achieved at 1.5 W pump power with an optical-to-optical efficiency of 19.3%. But the saturation appears when pump power goes higher which indicated the capacity of the microchip with this packaging method.

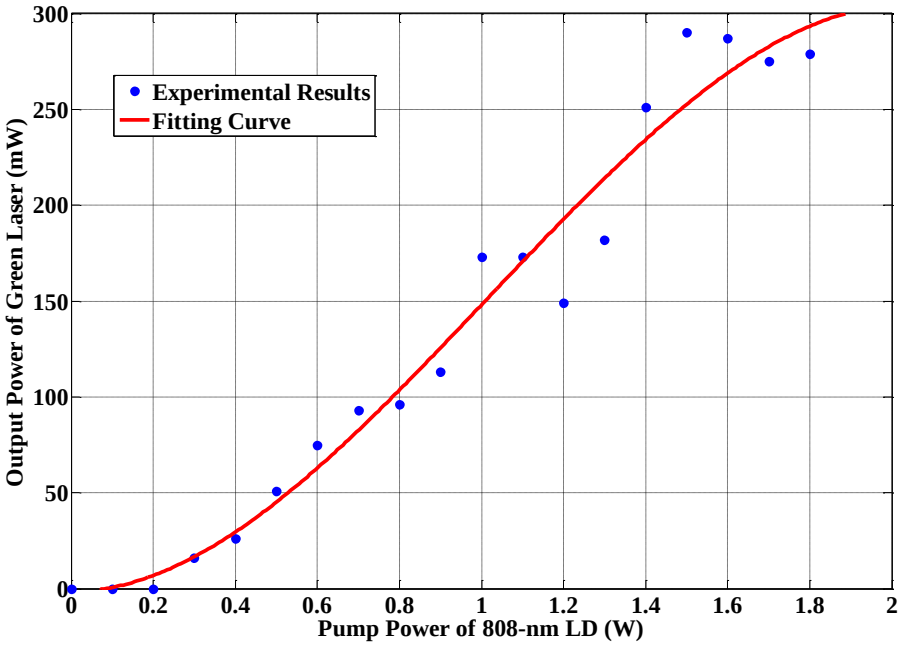

Figure 4.7. Lasing performance of the microchip in improved package.

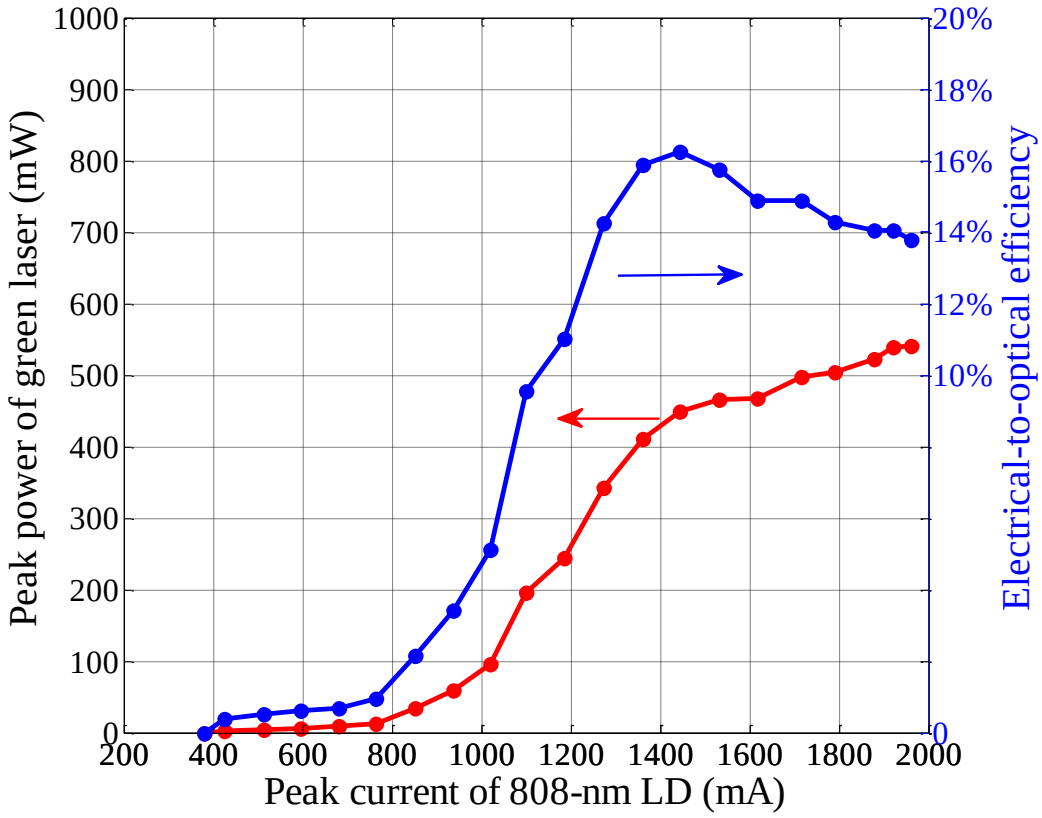

Figure 4.8. Peak power of green laser and Electrical-to optical efficiency.

For most laser-based LCoS and DLP projection display applications, the RGB light sources work in field-sequential operation mode. Therefore, the three RGB lasers are sequentially turn ON and OFF in the modulated mode. Thus the performance of modulated microchips are studied. The microchips are packaged as shown as Figure 4.5. (b). As shown in Figure 4.8, a maximum peak power of 540 mW is obtained at 1.96 A peak current of the pump LD. The output peak is limited by the maximum current of the pump LD which is 2 A according to experiments. The optical-to-optical efficiency is 33.5% with respect to the incident pump power. The maximum electrical-to-optical

efficiency is 16.25% when the pump peak current is set at 1.44 A. The increase of conversion efficiency is fast from 0.8 A to 1.45 A, but becomes saturated beyond 1.45 A due to the thermal effects.

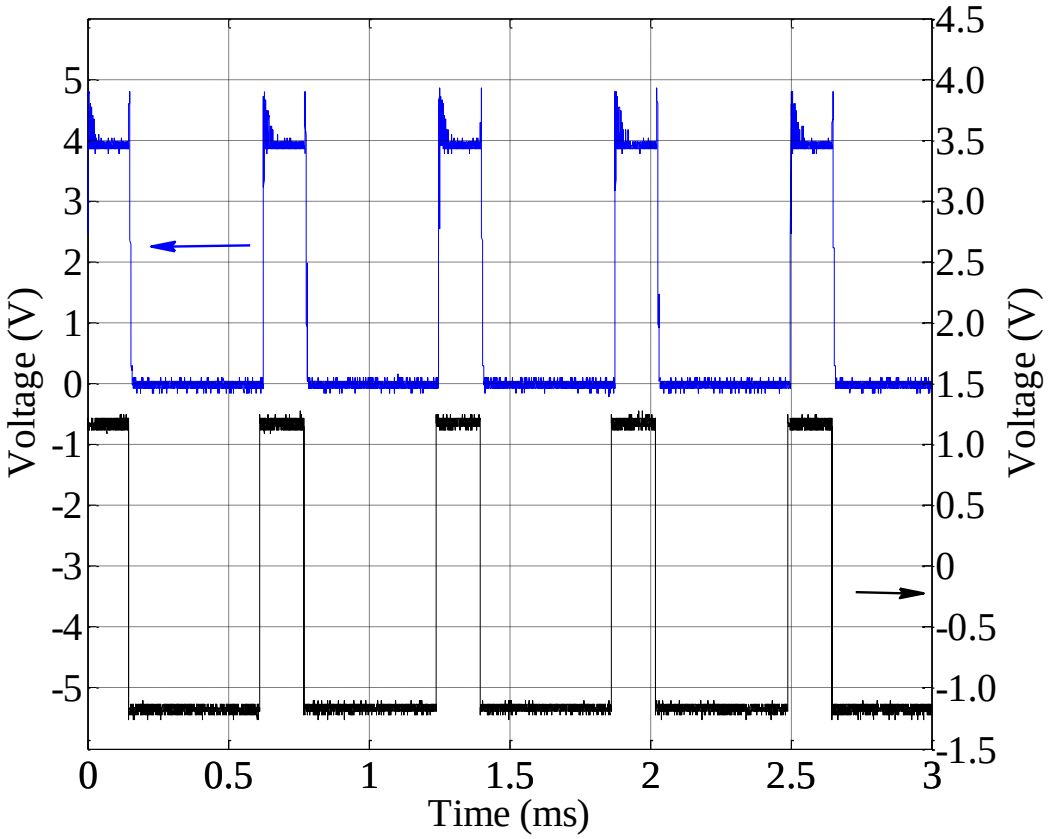

Figure 4.9. Detected modulation of green laser pulse and modulation signal.

For modulated laser display devices, modulation frequencies within the range from 60 Hz to 2 kHz with duty cycles from 25% to 33% are the best choices for the color balance optimization. Within these ranges, the average output power of the green laser increases with the repetition rate and the peak power decreases with the duty cycle. In this

case, by optimizing the modulation condition, the duty cycle and the repetition rate are 25% and 1.6 kHz, respectively, found from the experiments. Generally, the conversion efficiency increased with the increase of repetition rate. The upper waveform in Figure 4.9 is the output pulse sequence of the green laser which was measured at the maximum peak power of 541.5 mW, while the lower waveform is the modulation signal. The pulse sequence of the modulated optical-bonded Nd:YVO_4/MgO:PPLN microchip has good performance despite the small noise on the rising edge, which is related to the pump source. A DPSS green laser cannot be directly modulated at high speed (less than 10 KHz) due to the long fluorescence lifetime of the solid-state gain material (100 μs for 1% doped Nd:YVO_4).

4.3 Watt-Level Plane-Parallel Cavity DPSS Green Lasers

As the experimental results and discussion presented in the last section, an Nd:YVO_4/MgO:PPLN microchip can achieve 500 mW green laser with a considerable conversion efficiency. It is a potential good solution for pico and mobile laser display equipment. However, larger screen laser-based projection display systems usually require Watt-level low-cost and efficient green lasers. The microchip structure cannot achieve this output power level due to the limitation of the large heat dissipation of the optical bonded structure – normally not an issue in the discrete Nd:YVO_4 and MgO:PPLN structures. So conventional intra-cavity frequency doubled DPSS lasers with discrete gain mediums and nonlinear crystals are studied.

4.3.1 *Experiments and Results*

To meet the size and cost requirements of laser display applications, we have used a plane-parallel structure instead of conventional plane-concave structure. Compared with the plane-concave cavity, the plane-parallel cavity is more compact, has lower cost, and is robust from an ease-of fabrication point of view.

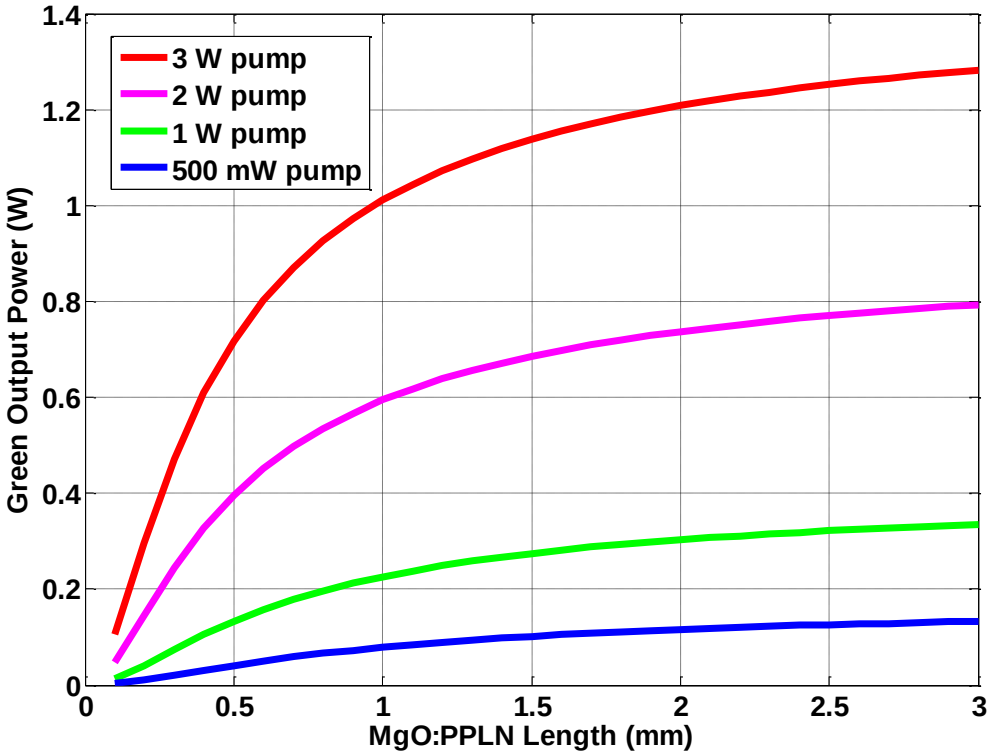

Figure 4.10. Calculated result of green output power of the IC-SHG DPSS laser as a function of the MgO:PPLN length under various pump powers.

In our design, the gain medium is an a-cut 2 mm long Nd:YVO_4 crystal with 1% neodymium dopant concentration. The length of the laser crystal is chosen to ensure completely absorption of 808-nm pump laser power. The intra-cavity frequency doubling theory mode in Chapter 2 is used to determine the length of the nonlinear crystal. Figure 4.10 shows the simulated result of the green output power of an intra-cavity frequency doubled DPSS laser as a function of the MgO:PPLN length under various pump powers. In order to achieve Watt-level green output power, a 1.6 mm long MgO:PPLN is employed in experiments.

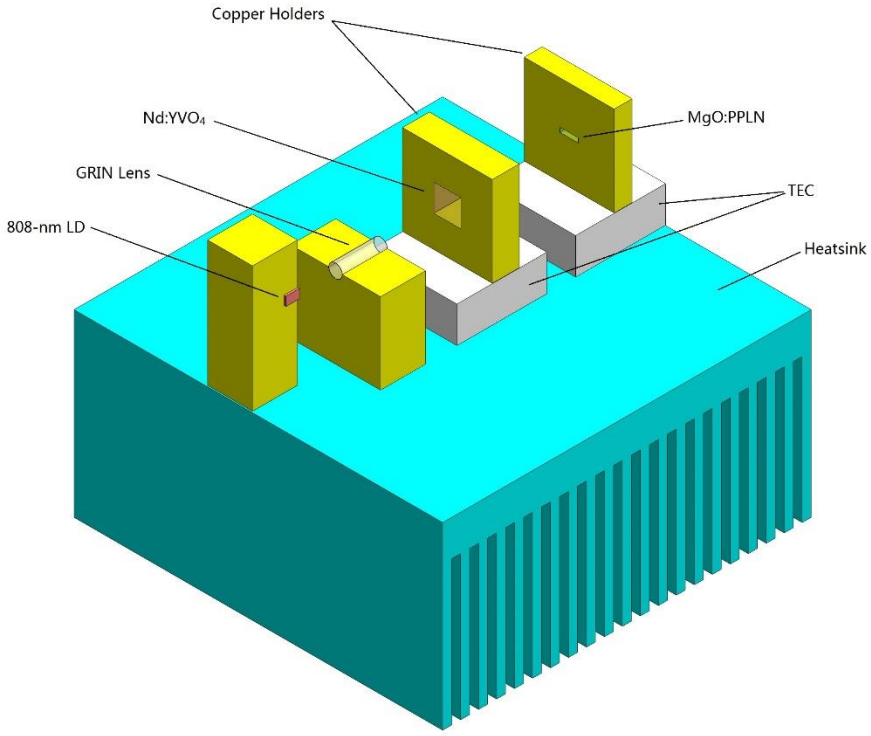

Figure 4.11. Schematic structure of the green laser.

A schematic diagram of our compact laser structure is shown in Figure 4.11. The pumping source is a standard broad-stripe fast-axis collimated 3 W laser diode with a central wavelength of 809 nm at room temperature. A 5 mm long 808 nm anti-reflection coated graded index (GRIN) lens is used to focus the pump light into the Nd:YVO_4 laser crystal with a beam waist around 60 μm. A thermally stabilized plane-parallel cavity is formed by the input facet of Nd:YVO_4 crystal and the output facet of MgO:PPLN crystal. These two surfaces are coated for high-reflectivity (R>99.8%) at 1064 nm fundamental wave to make the intra-cavity fundamental laser power high, thus the high conversion efficiency is achieved. The input facet of Nd:YVO_4 crystal is also coated for high-transparency at 808 nm and high-reflectivity at 532 nm to reduce the pumping loss and reflect the green to output direction. The right facet of Nd:YVO_4 crystal and left facet of MgO:PPLN crystal are both coated for anti-reflectivity at both 1064 nm and 532 nm to reduce the intra-cavity loss. The output facet of MgO:PPLN crystal are also coated for anti-reflectivity at 532 nm to achieve the highest green light output. The total length of the laser, including the pump diode, is about 18 mm and the total volume of the laser package is less than 4 cm^3.

The MgO:PPLN crystal is wrapped with indium foil and mounted in a copper holder which attached on a small TEC. This TEC is used to maintain the temperature of the nonlinear crystal at designed QPM temperature. The optimized temperature of MgO:PPLN chip we used in our setup is 22 ℃. The pumped laser diode, GRIN lens and Nd:YVO_4 crystal are simultaneously temperature stabilized to 25 °C by another bigger TEC. The plane-parallel cavity is on the limit of cavity stability. The predominant guiding

mechanism is a distributed thermal lens, thus the temperature of cavity elements should be fixed for certain operation power. This is the reason why we employ two TEC elements in the design.

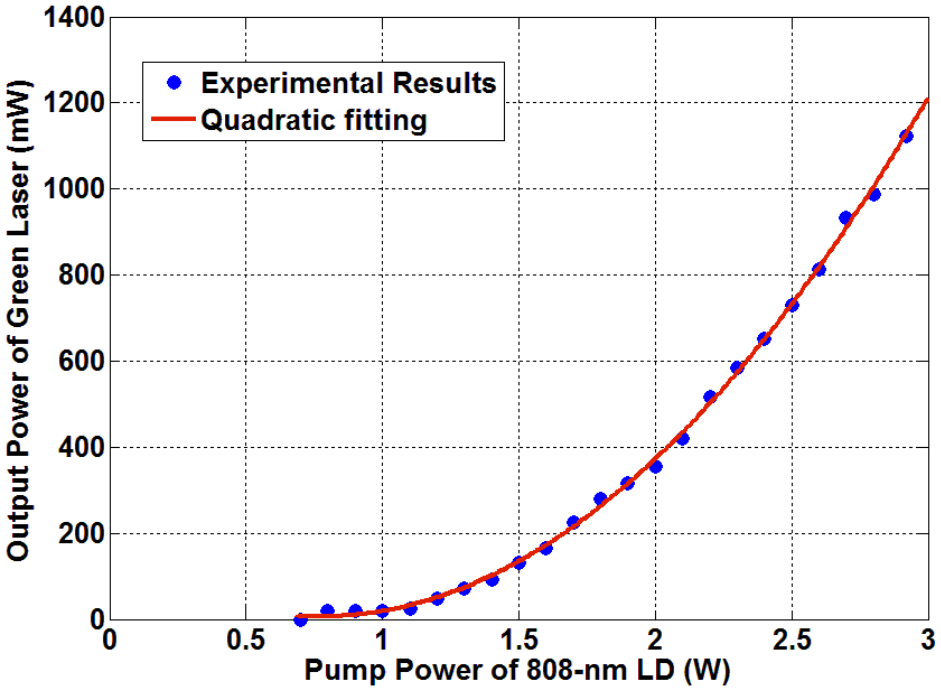

Figure 4.12. Output power of green laser as a function of pump power.

Figure 4.12 shows the output performance of the green laser. For the CW operation mode, the maximum output power of 1.12 Watt is achieved with 2.9 Watt pump power. The optical-to-optical efficiency is 38.6% with respect to the incident pump power. Although this efficiency was similar to the results by using other crystals in our previous experiments and other published literatures [116, 117], using MgO:PPLN crystal in our parallel-plane cavity has simpler alignment and shorter cavity length.

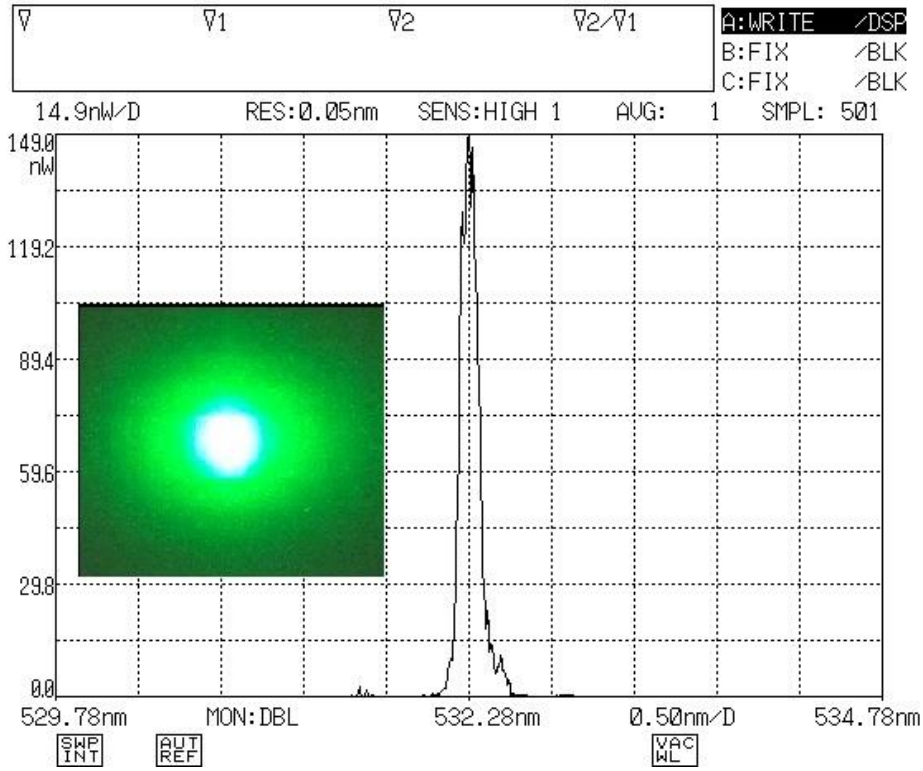

Figure 4.13. The spectrum properties of the output green light and a beam photo.

As shown in Figure 4.13, the wavelength of output green light is 532.28 nm with FWHM bandwidth less than 0.2 nm. Narrow bandwidth at exact green wavelength is the main reason that the projection display system using this kind of laser sources is superior to those using traditional light sources in image quality and energy consumption point of view. Moreover, the linearly polarized output green light is another advantage for DPSS green laser based on MgO:PPLN crystals for the polarization-based 3D projection display. The insert picture shows the output green beam profile measured by a CCD camera. Low étendue value due to the near diffraction limited output beam is another

major advantage of a laser over light sources based on LED or lamps. Because the étendue value of a light source cannot be reduced. The typical étendue value for a lamp (4π emission) is about 10 to 15 mm^2 sr while for a LED (1 mm^2) is about 7 mm^2 sr. The étendue value for an ideal single transvers mode is closed to zero. Although a practical laser source cannot has an ideal diffraction limited output beam, the étendue value of most solid state lasers is lower than LED sources. Thus, even LEDs have similar electro-optical efficiency as lasers, optical engines based on LEDs either have lower efficiency or more complex optical lens system.

The long-term output stability is also measured by a computer-recorded power meter. As shown in Figure 4.14, in 4 hours, the fluctuation is less than 4%, which is acceptable for laser-based projection display applications

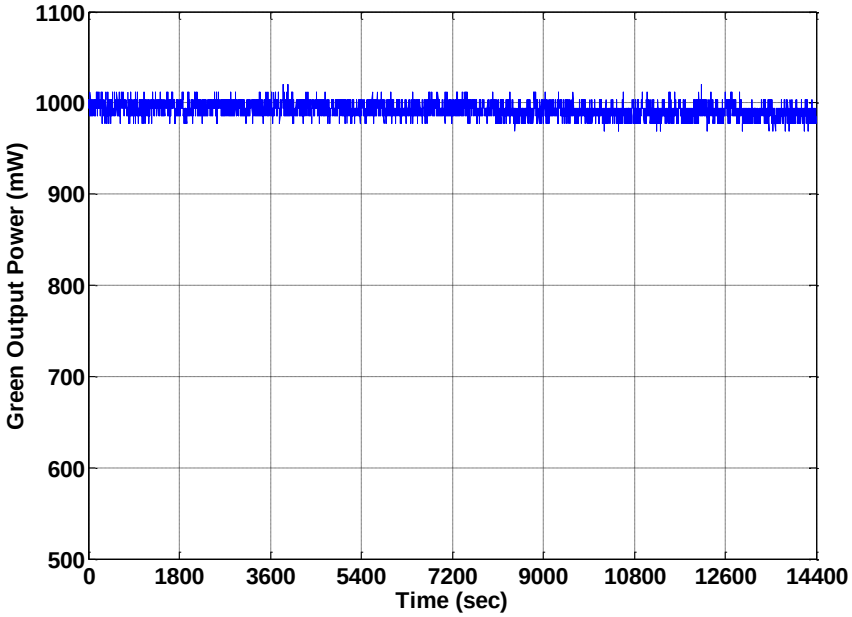

Figure 4.14. Long-term stability of the green output power.

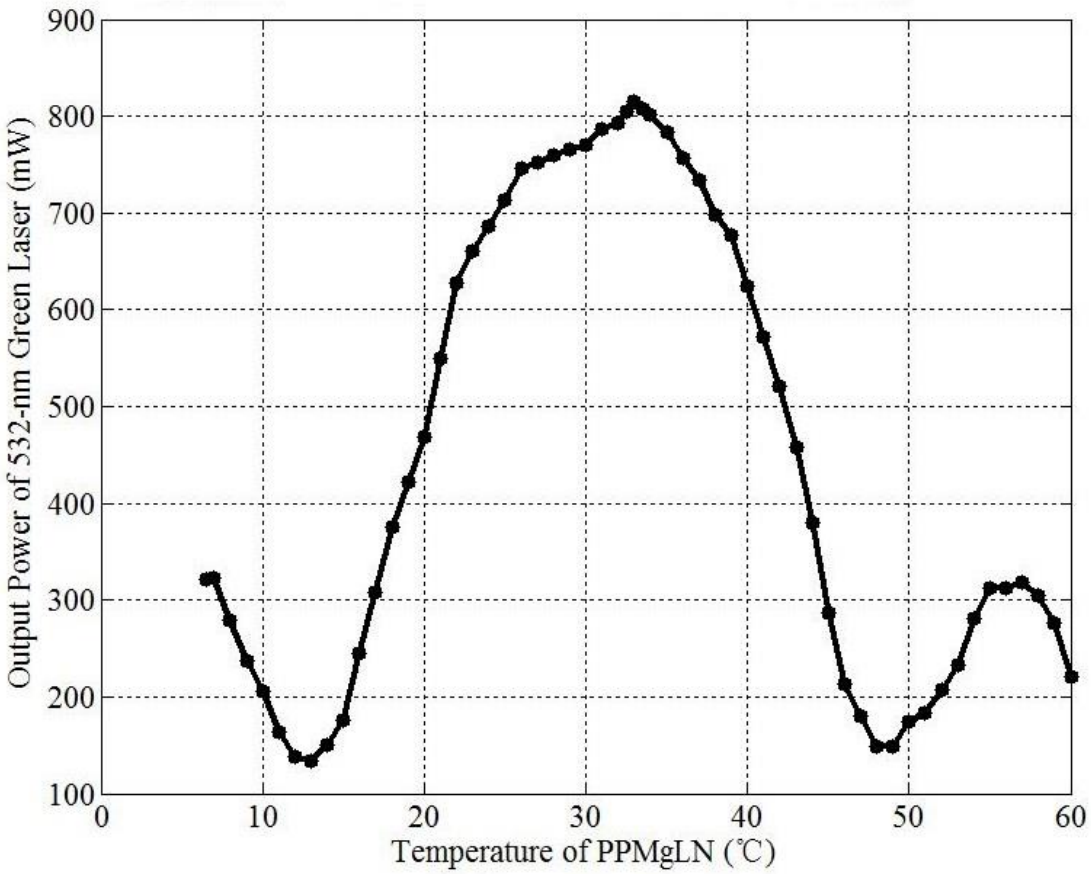

Figure 4.15. Temperature tuning curve of the MgO:PPLN crystal.

The temperature tuning curve of MgO:PPLN is measured and shown in Figure 4.15. The temperature tolerance of the MgO:PPLN chip is more than 20 ℃ (FWHM).

In Figure 4.12, no power saturation is observed in the experiments, implying that higher power can be achieved with the proposed configuration. As shown in Figure 4.16, another experiment setup is built to achieve a multi-Watt green laser.

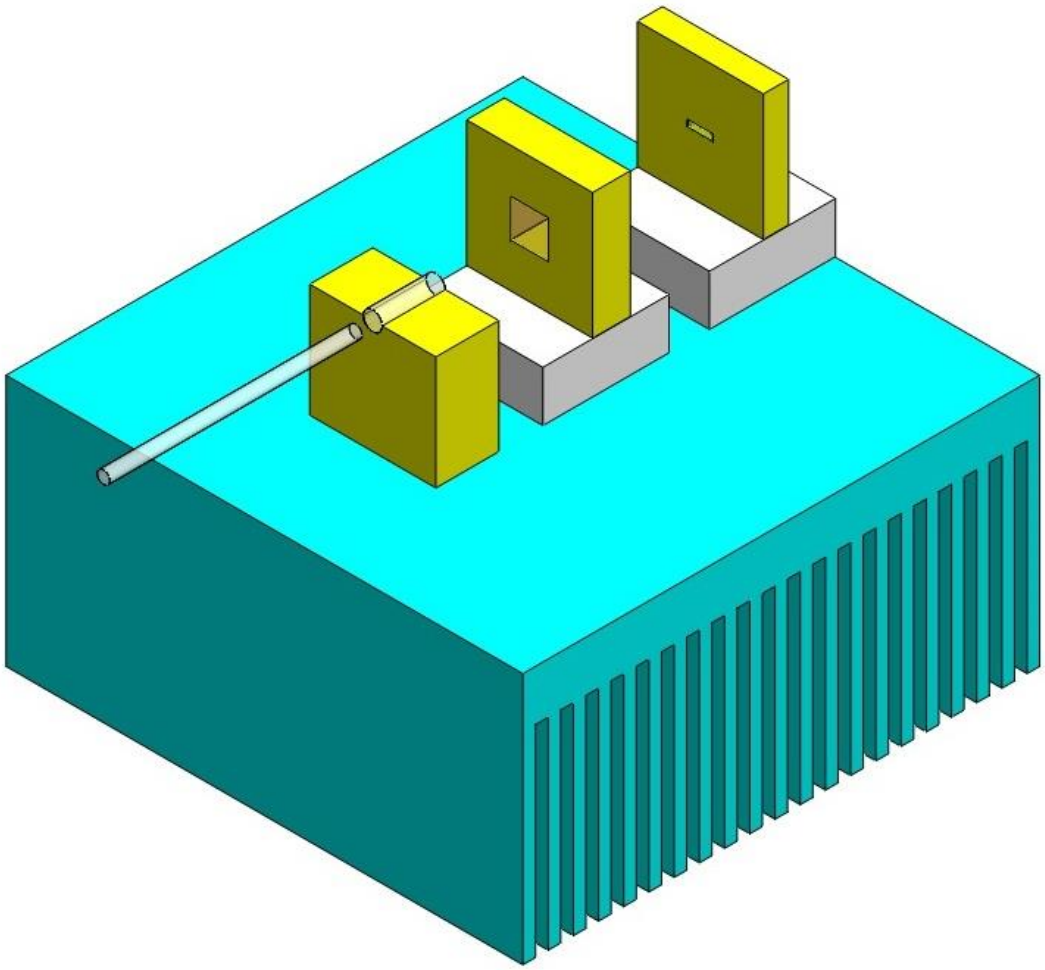

Figure 4.16. Fiber pumped Nd:YVO_4/MgO:PPLN green laser setup.

Compared with the setup shown in Figure 4.11, the pump source is changed to a fiber coupled 10 W 808 nm laser diode. The output fiber is a 400 μm core diameter multi-mode fiber. The rest components are the same as before. The Nd:YVO_4 crystal is stabilized at 25 ℃ by the TEC and the MgO:PPLN crystal is maintained at optimized QPM temperature.

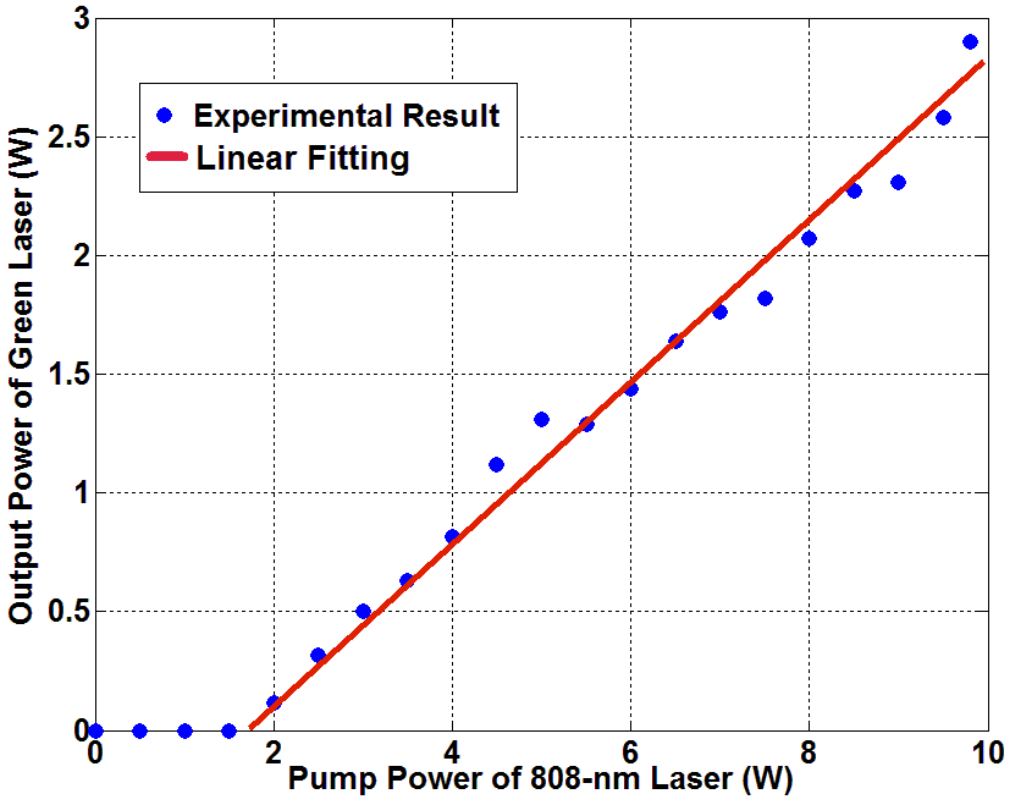

Figure 4.17. Power of green laser versus pump power of 808-nm LD.

Figure 4.17 shows the green output power versus the pump power from the 808 nm LD. A maximum output power of 2.9 W is achieved with 9.8 W of pump power, which corresponds to an optical-to-optical efficiency of 29.6%. The lasing threshold of this curve is larger than Figure 4.12, which is because of the different pump sources used in two different experiments. The fiber coupled 808-nm LD used in this experiment emits a random polarized 808-nm laser which will decrease the performance of Nd:YVO_4/MgO:PPLN lasers at low pumping level due to the polarization depended absorption and emission of Nd:YVO_4 crystal. Thus the lasing threshold for the setup

shown in Figure 4.16 is larger than using a linear polarized pump LD. Power saturation still do not appear from the experimental results, which means that higher green power can be obtained simply by increasing pump power. Due to the limitations of the experimental conditions, we do not push to even higher power.

4.4 Compact Integrated Green Laser Module

The previous two sections demonstrate intra-cavity frequency doubled green lasers based on Nd:YVO_4/MgO:PPLN microchip devices and separated Nd:YVO_4/MgO:PPLN plane-parallel structures, respectively. Form the laser display applications' point of view, advantages and disadvantages exist in both two solutions.

The microchips are extremely compact so it is very easy to embed them into mobile laser display devices. They also have potential to be manufactured in mass production at a very low cost. But from our experiments we can find that Nd:YVO_4/MgO:PPLN microchips are only suitable for low power (< 300 mW, CW mode) applications due to thermal transfer between two bonded crystals. While separated Nd:YVO_4/MgO:PPLN structures can be used to generate multi-Watt level green laser. Although plane-parallel cavity design is used to reduce complicity, there are still at least three components (a pump LD, a laser crystal, and a nonlinear crystal) in the system. The alignment between these elements seriously affects the lasing performances. Therefore, green lasers based on this structure still do not match the cost and mass production requirements of laser display industry.

In order to further reduce the cost and simplify the packaging process, a novel compact Nd:YVO_4/MgO:PPLN integrated module (namely mGreen module) has been developed [118]. The structure design, performance evaluation, and optimization of this integrated module are presented in following sub-sections

4.4.1 *Structure Design*

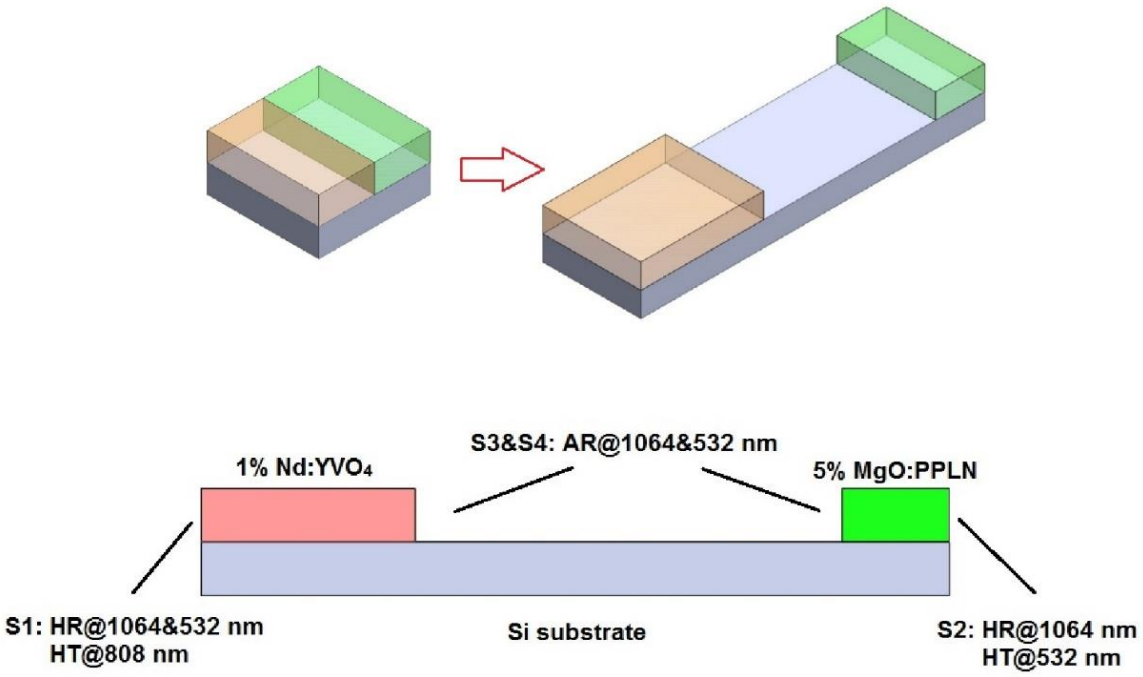

Figure 4.18. Schematic structure of the integrated Nd:YVO_4/MgO:PPLN module.

As shown in Figure 4.18, in order to combine the advantages of the microchip structure and the separated plane-parallel structure, an mGreen module integrates a laser crystal and a nonlinear optical crystal together on a silicon substrate. The two crystals are

precisely aligned to from an alignment-free plane-parallel cavity. The input facet of the laser crystal is coated for high transmission at 808 nm pump wavelength, and high reflection at both 1064 nm and 532 nm wavelength. The output facet of the nonlinear crystal had a high reflection coating for 1064 nm and high transmission coating for 532 nm light. The two internal facets are coated for anti-reflection at both 1064 nm and 532 nm.

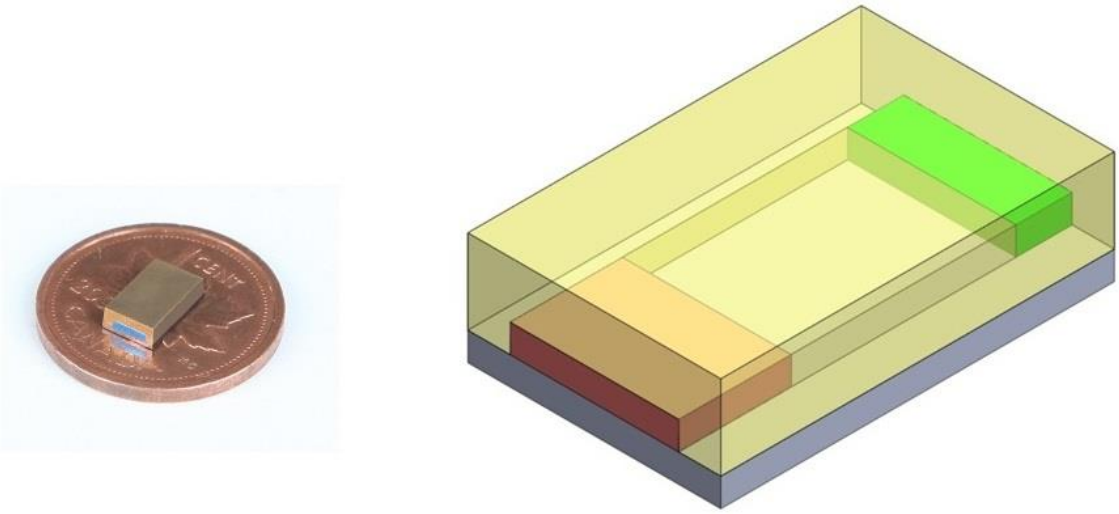

Figure 4.19. A photograph and 3D schematic diagram of the mGreen module.

As shown in Figure 4.19., in order to achieve uniform thermal conductivity and protect the cavity from dust pollution, a copper cap is placed on the top to cover the two crystals. The length of Nd:YVO_4 and MgO:PPLN crystals are 2 mm and 1 mm, respectively, which as same as used in previous experiments. The gap between two crystals is initial set to 4 mm, which is also optimized by previous separated plane-

parallel cavity experiments. Thus, the mGreen module has a size of only 7(L) × 4.5(W) × 2(H) mm^3 (i.e. 0.063 c.c.). Therefore, compact green lasers based on mGreen module can be mass produced at a very low cost to meet the strict performance/cost requirement of commercial laser projectors.

4.4.2 *Performance Evaluation and Optimization*

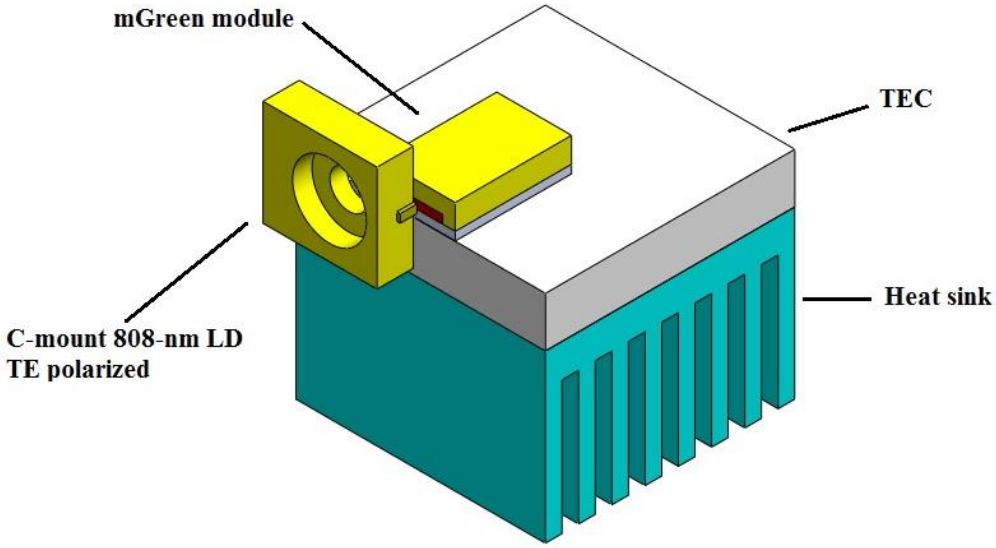

Figure 4.20. Experimental configuration of an mGreen module based green laser.

A green laser structure based on the mGreen module is shown in Fig. 4.20, which basically consists of only two components, i.e. one 808-nm pump laser diode and an mGreen module. Since the mGreen module has already integrated the laser crystal and the frequency doubling crystal together, we only need combine a pump source with an

mGreen module to form a laser. To achieve the highest frequency doubling efficiency, the polarization direction of the fundamental light should be in parallel with the z-axis of the MgO:PPLN crystal. Therefore, in our experiments, a standard broad-stripe 5 W TM polarized 808 nm LD is rotated by 90 °when it is used as the pump source. The distance between the LD emitting facet and mGreen input facet is set to 0.3 mm.

Figure 4.21 shows the output power of green laser as a function of 808 nm LD pump power. The maximum output power of 1.28 Watt is achieved at 4.4 W pump power, which corresponds to an optical-to-optical conversion efficiency of 29.1%. The trend of the curve does not show any saturation, implying that the green output power can be further increased by using a higher pump source. As shown in figure, the output green power is almost independent on the usage of a focusing lens between the 808 nm pump laser diode and the mGreen module, implying that the green laser can be easily packaged. In order to achieve high quality output beam, the 808 nm pump laser diode used in the experiments is fast-axis collimated.

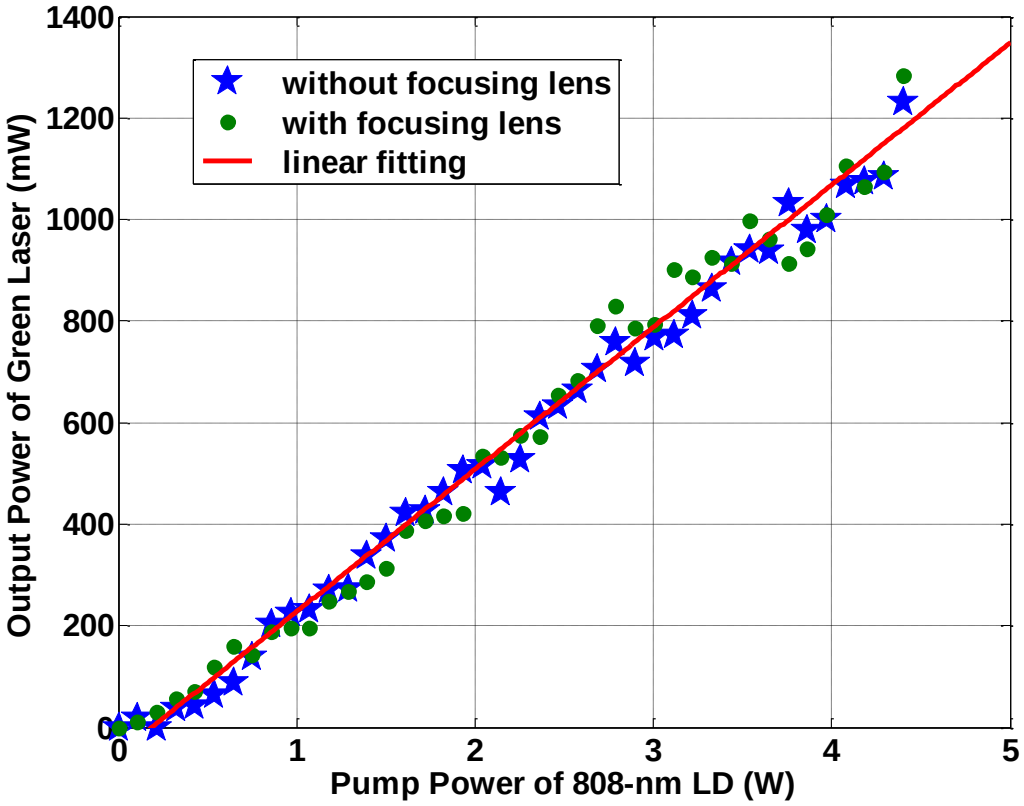

Figure 4.21. Output power of green laser versus pump power of 808-nm LD.

The temperature dependence of the mGreen module was also studied. As shown in Figure 4.22, the highest output power is reached at 18 ℃. Although the green power is measured only in a range from 15 ℃ to 50 ℃ due to the limitation of the temperature controller used in the experiments, it is found that the temperature tuning curve can be fitted with a sinc^2 function. In the measurements, a MgO:PPLN with a QPM temperature of 33 ℃ is used. The shift of the optimal temperature from 33 ℃ to 18 ℃ indicates that the heat generated in Nd:YVO_4 has been transferred to MgO:PPLN and there exists a thermal resistance between MgO:PPLN and Si substrate.

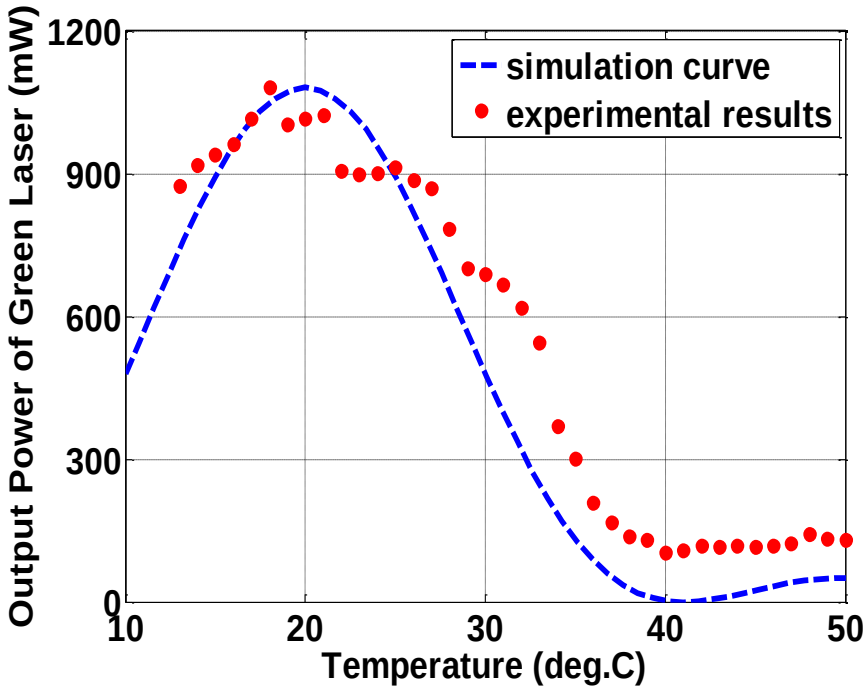

Figure 4.22. Temperature tuning curve of the mGreen module.

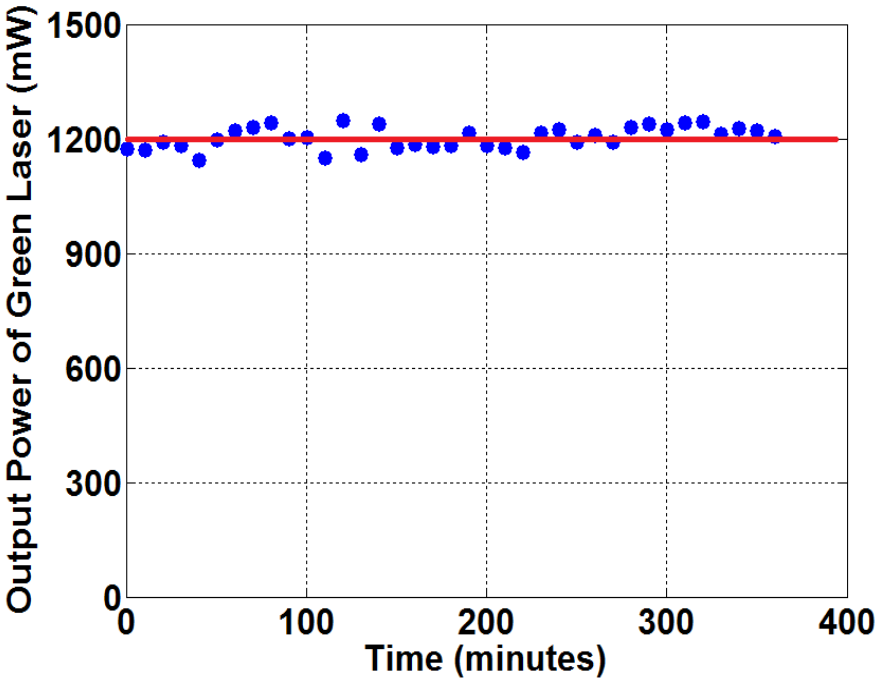

Figure 4.23. Green output power as a function of time.

Figure 4.23 shows green output power from an mGreen module as a function of time. Over six hours, green power fluctuation is within 5%, implying that the mGreen module has very good power stability for laser display applications.

The optimization of mGreen has two main targets: higher efficiency and higher operation temperature. Compared with the previous results of separated structure, the conversion efficiency achieved by the mGreen module seems to be a little bit lower. And optimized working temperature of 18 ℃ is also lower for laser display applications.

Review the structure shown in Figure 4.18, we found that one important factor for performance improvement is the facet coating. If we put a high reflection of 532 nm coating on the internal facet of MgO:PPLN crystal, we could prevent green laser from coming into the Nd:YVO_4 crystal to avoid the green light absorption in gain medium. Thus the internal cavity loss was reduced and the efficiency dramatically enhanced.

Increasing the working temperature relies on two aspects: MgO:PPLN with high QPM temperature and suitable cavity length. A series of experiments was designed to investigate the relationship between working temperature and cavity length. As shown in Figure 4.24, when laser crystal is working at higher temperature, a longer cavity is more suitable to achieve high output power. This phenomenon is due to the more serious thermal lens effect under high working temperature. Increase the cavity length will compensate partial thermal lens effect and maintain the cavity on optimal working condition. Based on this experimental results, we increased cavity length from 7 mm to 9 mm for design a mGreen module working at around 30 ℃.

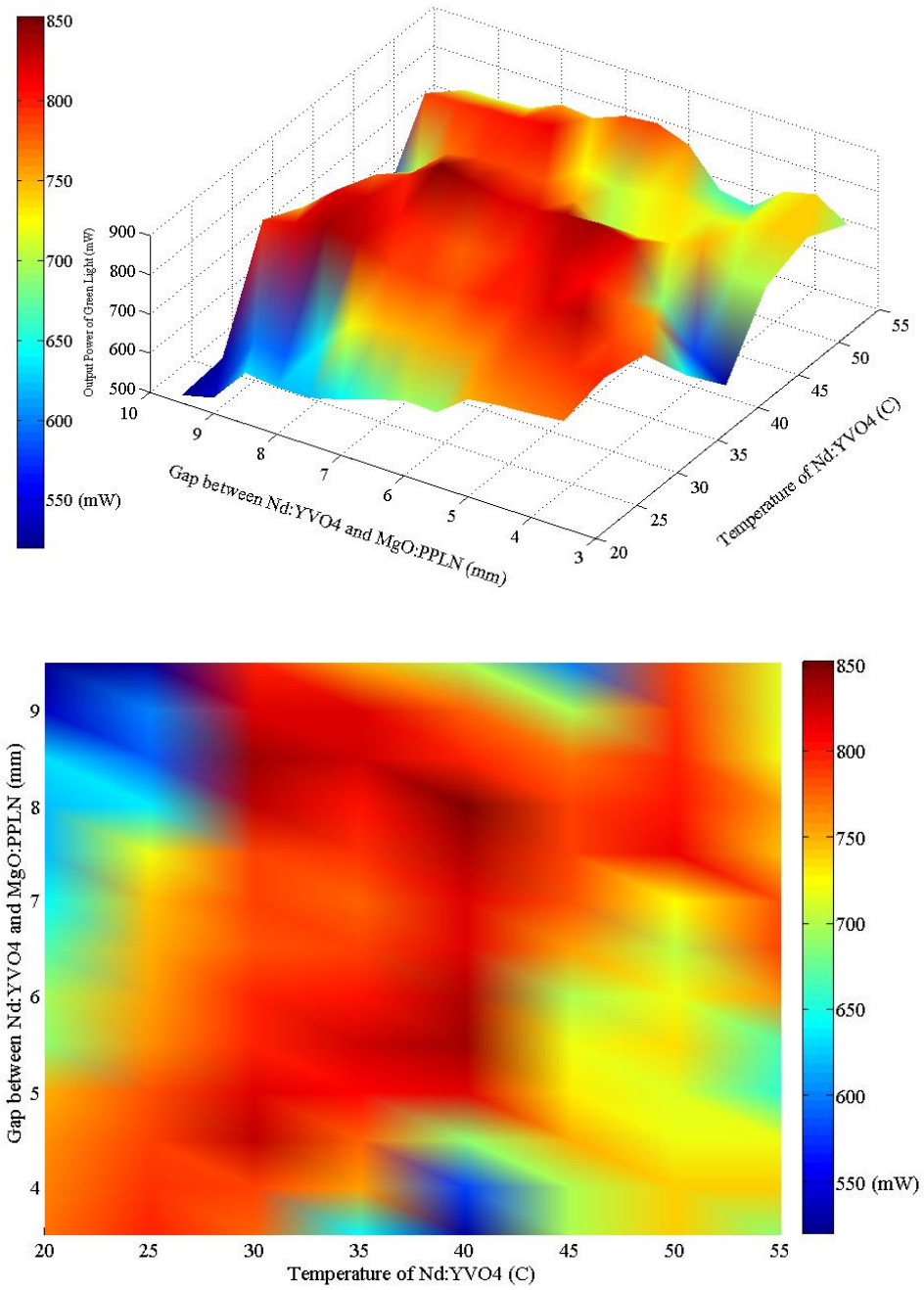

Figure 4.24. 3D and 2D distribution of output power versus gap and temperature of Nd:YVO_4.

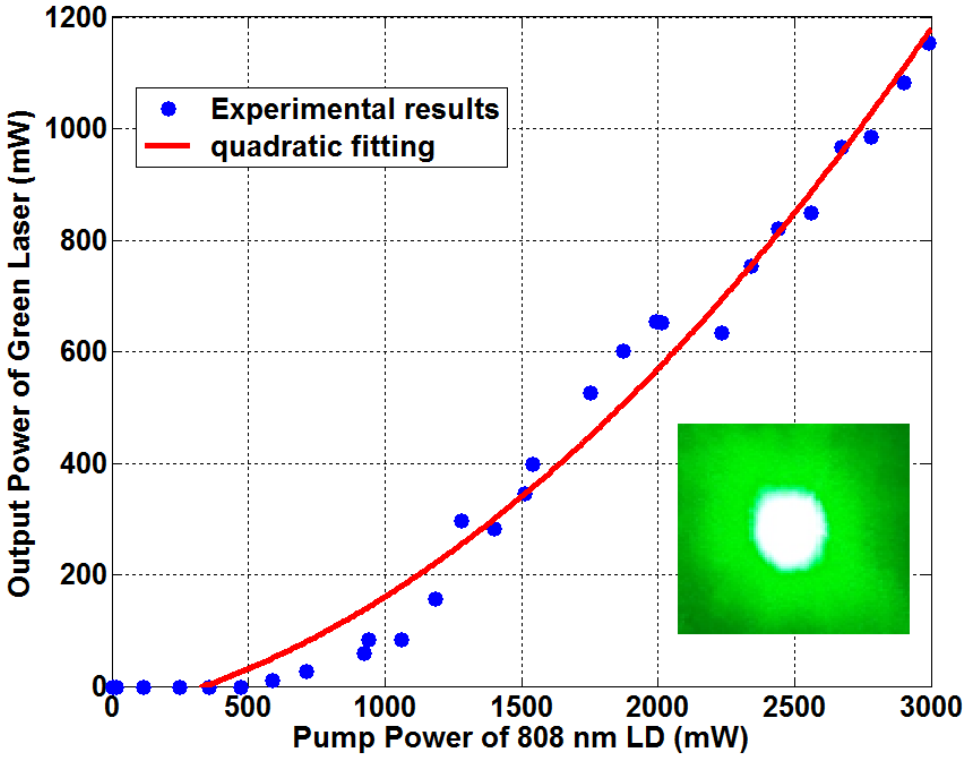

Figure 4.25. Output power of green laser versus pump power of 808-nm LD.

Figure 4.25 shows the green output power as a function of 808 nm LD power for optimized mGreen module. Maximum output green laser power of 1.15 watt is achieved at 3 watt pump power, which corresponds to an optical-to-optical conversion efficiency of 38.5%. Compared with the previous 29% efficiency, more than 10% efficiency enhancement is achieved by the optimized structure. Non-saturated curve indicates that much higher green power can be obtained by simply increasing pump power. The beam profile of the green laser is also shown in Figure 4.25. It is Gaussian shaped and linearly polarized, which satisfies the requirement of laser display systems.

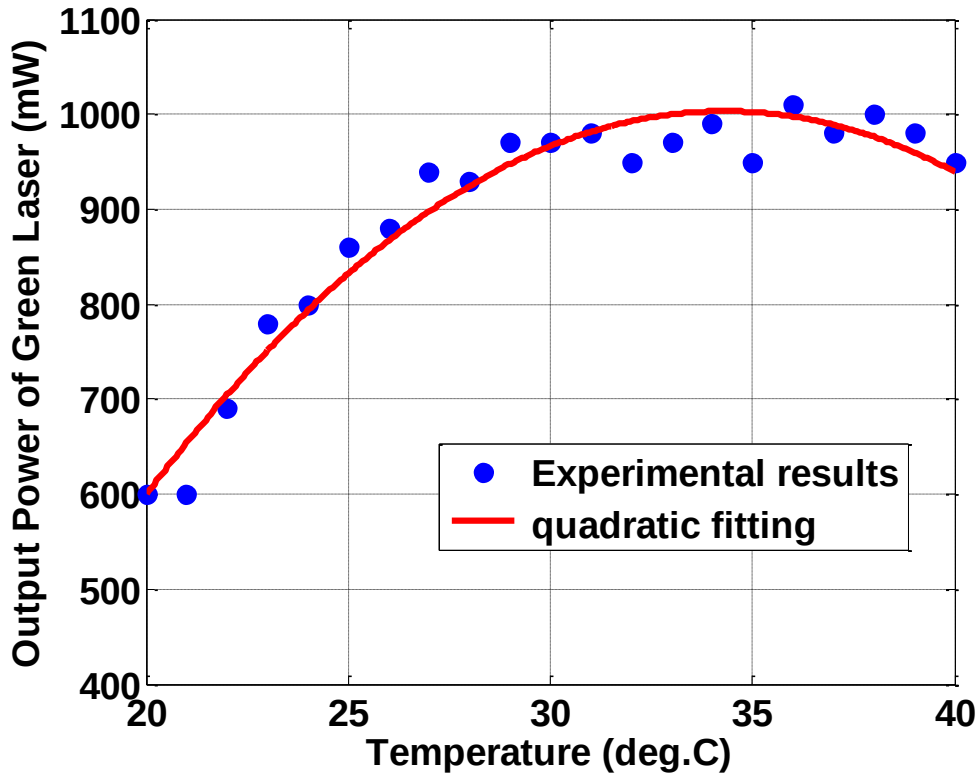

Figure 4.26. Temperature tuning curve of optimized mGreen module.

Another obvious improvement of the optimized structure is the increasing of operation temperature. The optimal temperature of initial mGreen module is only 18 ℃, which is too low for practical applications. By employment of a MgO:PPLN crystal with higher QPM temperature and a longer cavity length, we successfully achieved a mGreen module that can work at around 30 ℃. Figure 4.26 shows the temperature dependence of the optimized mGreen module. Even if the measured temperature range from 20 ℃ to 40 ℃ is limited by our temperature controller, the trend of the curve can be easily predicted. Operation temperature is enhanced by nearly 20 ℃ based on the new mGreen design. The

FWHM (Full Width at Half Maximum) temperature tolerance of the mGreen module is more than 30 ℃.

4.4.3 Power Scaling

Different laser display applications require different power level of light source. As a high end and high profit display market, larger screen front projection usually requires an output of several watts of visible laser or even higher. Thus, the power scalability of the mGreen module is a valuable research point.

Since no power saturation is observed in Figure 4.25, the most straightforward direction to achieve higher green laser is just increasing the pump power. The 10 W fiber coupled 808 nm laser diode used in previous experiments was adopted to pump an optimized mGreen module. The 400 μm diameter pump beam was focused by a GRIN lens into the mGreen module. Figure 4.27 shows the output power of green laser as a function of the pump power.

Although output power of green laser can reach 2.6 W, the saturation is obvious when the pump power is higher than 8.5 W. Moreover, the working temperature is decreased to 14 ℃ at this moment,which means the thermal loading of the mGreen module cannot satisfy a single pump beam larger than 8.5 W.

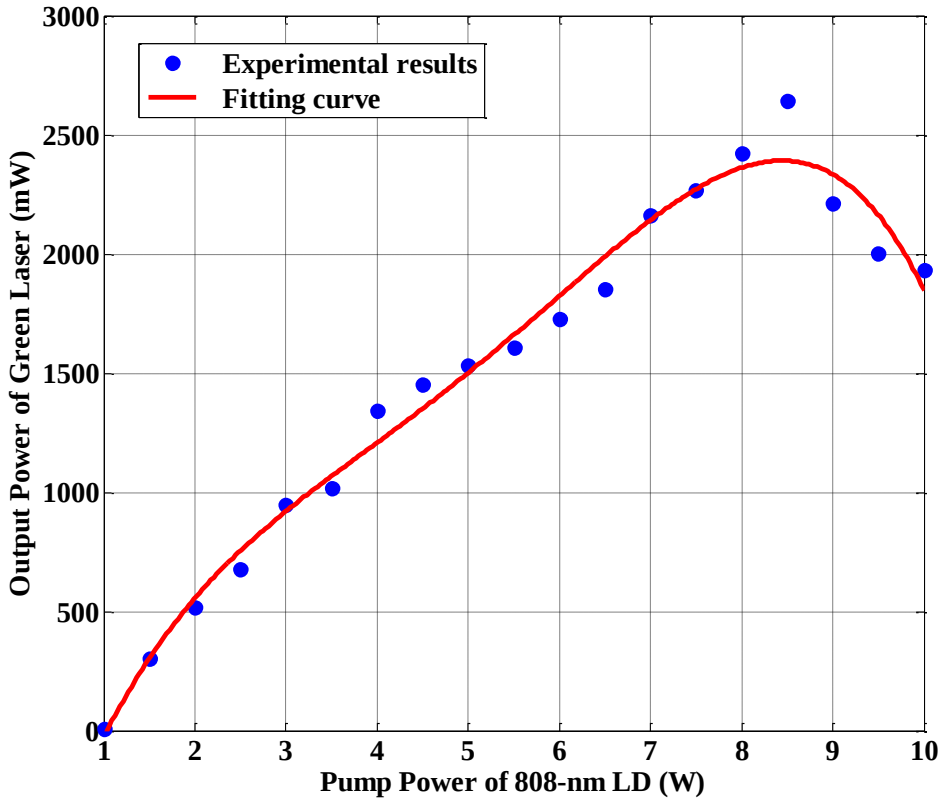

Figure 4.27. Output power of green laser versus pump power of 808-nm LD.

Since mGreen module is based on the plane-parallel cavity design, array configuration is an alternative solution when single beam structure cannot overcome the thermal management issue. As shown in Figure 4.28, to build the mGreen module based array structure, we just need an 808-nm pump LD array and a wider mGreen module. In the design shown in Figure 4.28, the most important parameter is the gap between each pump emitter. If the gap is two narrow, the two neighboring pump beams will be partially overlapped, thus the laser beam in the cavity will merge together due to the thermal coupling. On the other hand, wider gap leads large volume of the green laser and

increases the cost. So before ordering the 808-nm pump LD array, we need find out the suitable emitter gap first.

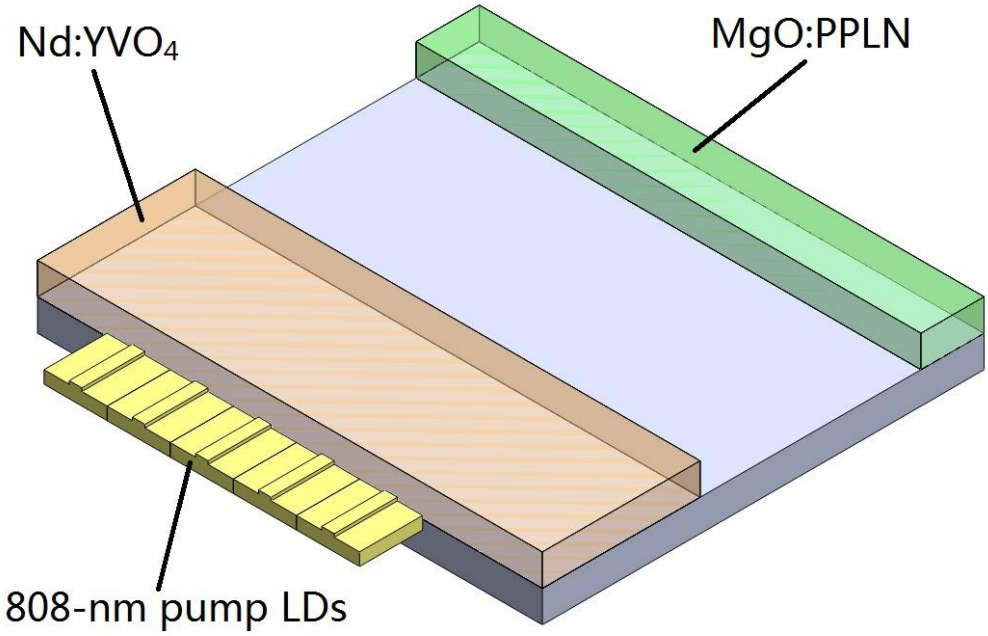

Figure 4.28. Schematic of array configuration design.

The finite element simulation was used to investigate the pump gap dependence of array configuration mGreen module. We assume an mGreen module is pumped by three circular beams with a 200 um diameter. The gap between each pump beam is set to 0.2 mm, 0.3 mm, 0.4 mm, 0.5 mm, 0.75 mm, and 1 mm, respectively. Figure 4.29 shows the simulation results by a commercial finite element analysis software. Form these figures we can see that the thermal interference between the neighboring laser beams is serious when the gap less than 0.75 mm.

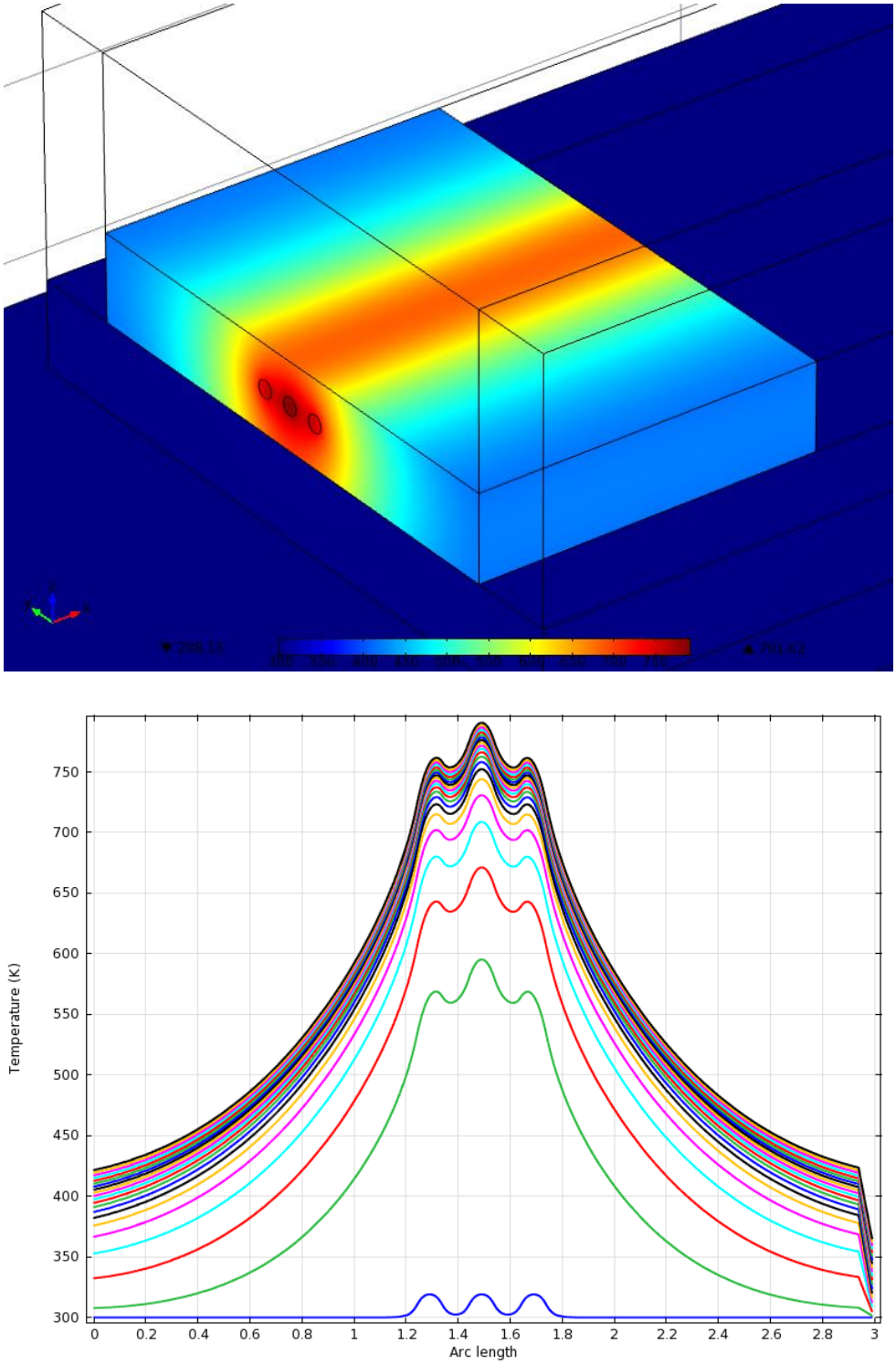

Figure 4.29. (a) Simulated thermal distribution in mGreen module (0.2-mm gap)

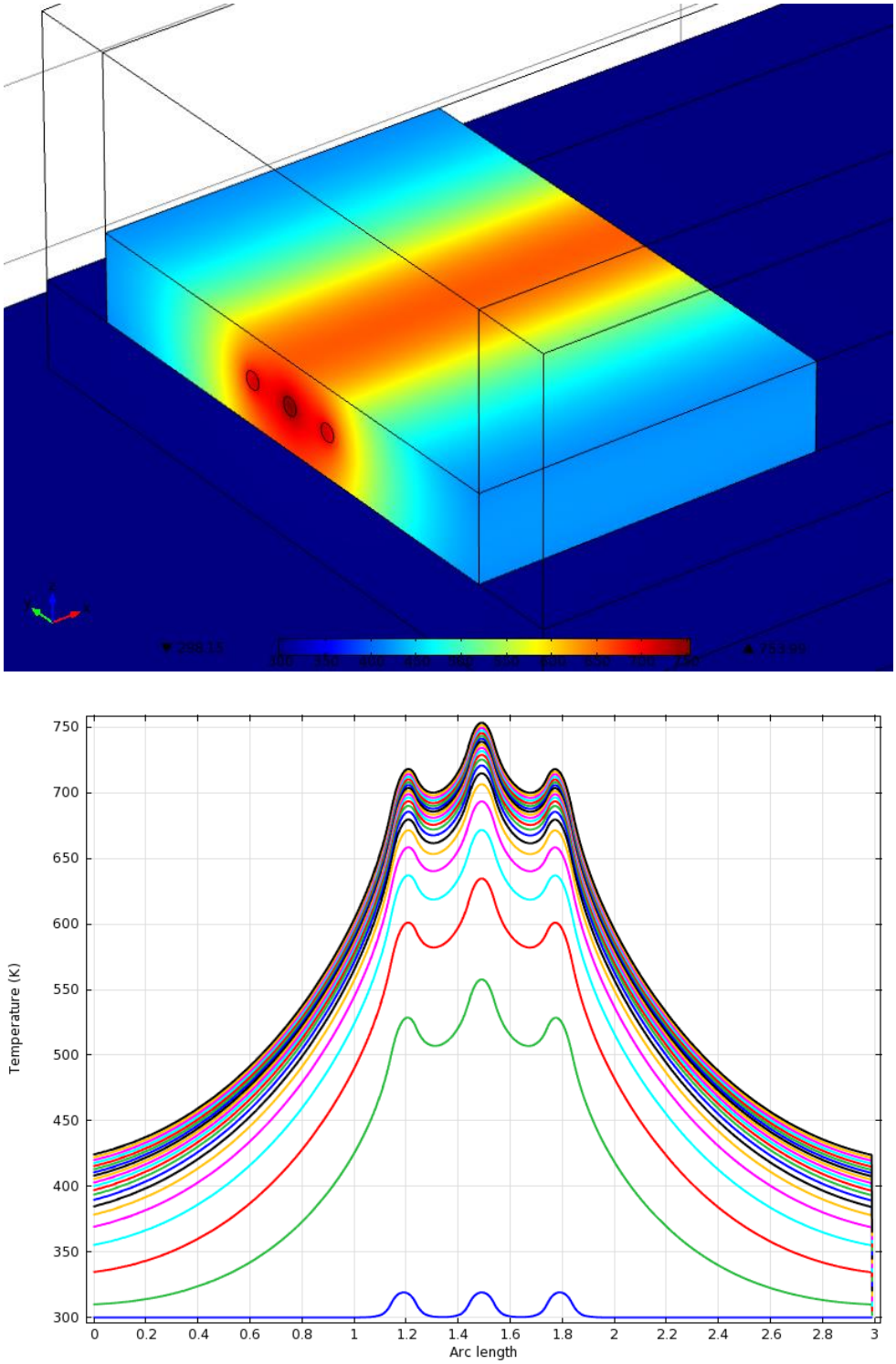

Figure 4.29. (b) Simulated thermal distribution in mGreen module (0.3-mm gap)

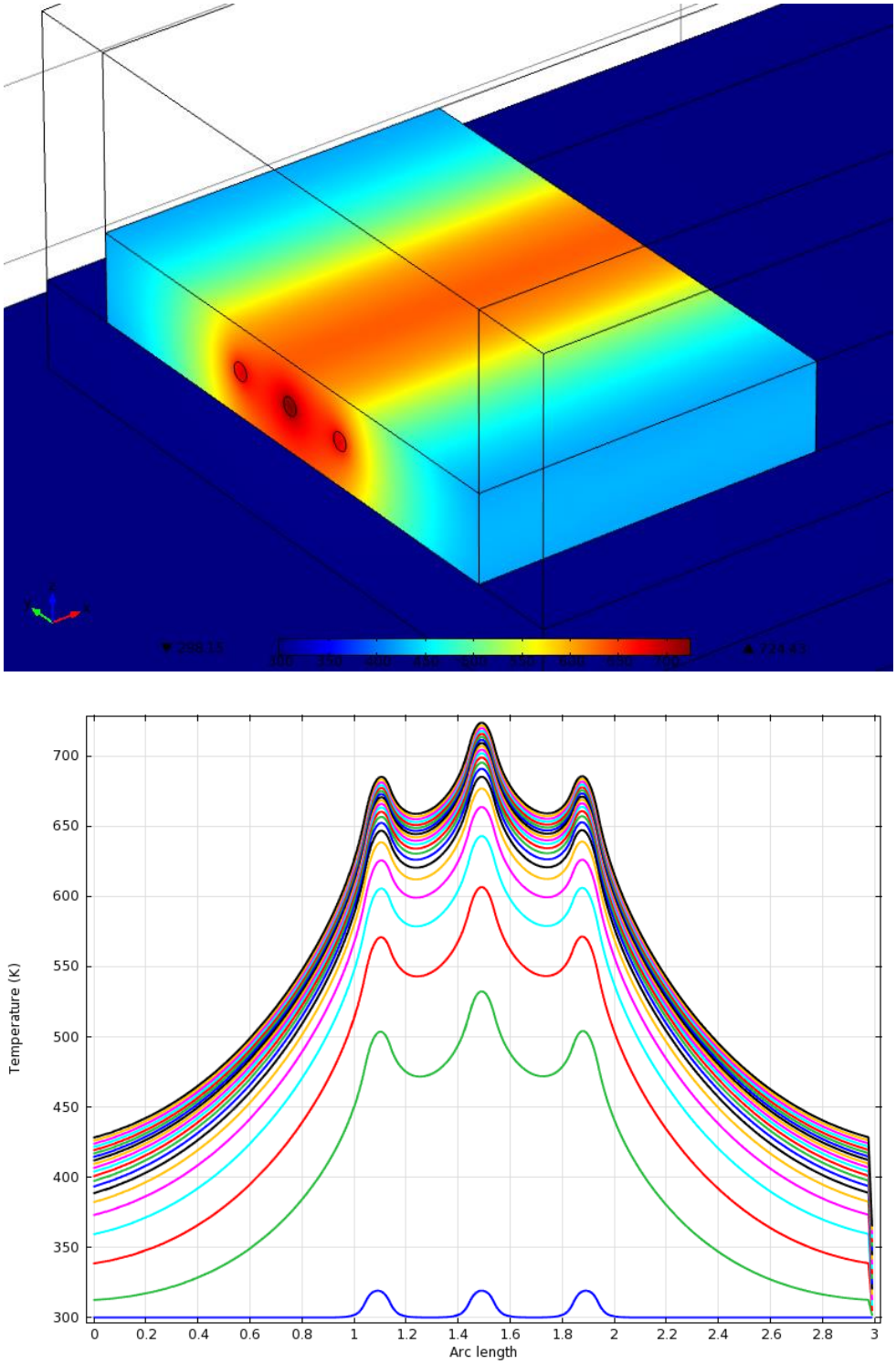

Figure 4.29. (c) Simulated thermal distribution in mGreen module (0.4-mm gap)

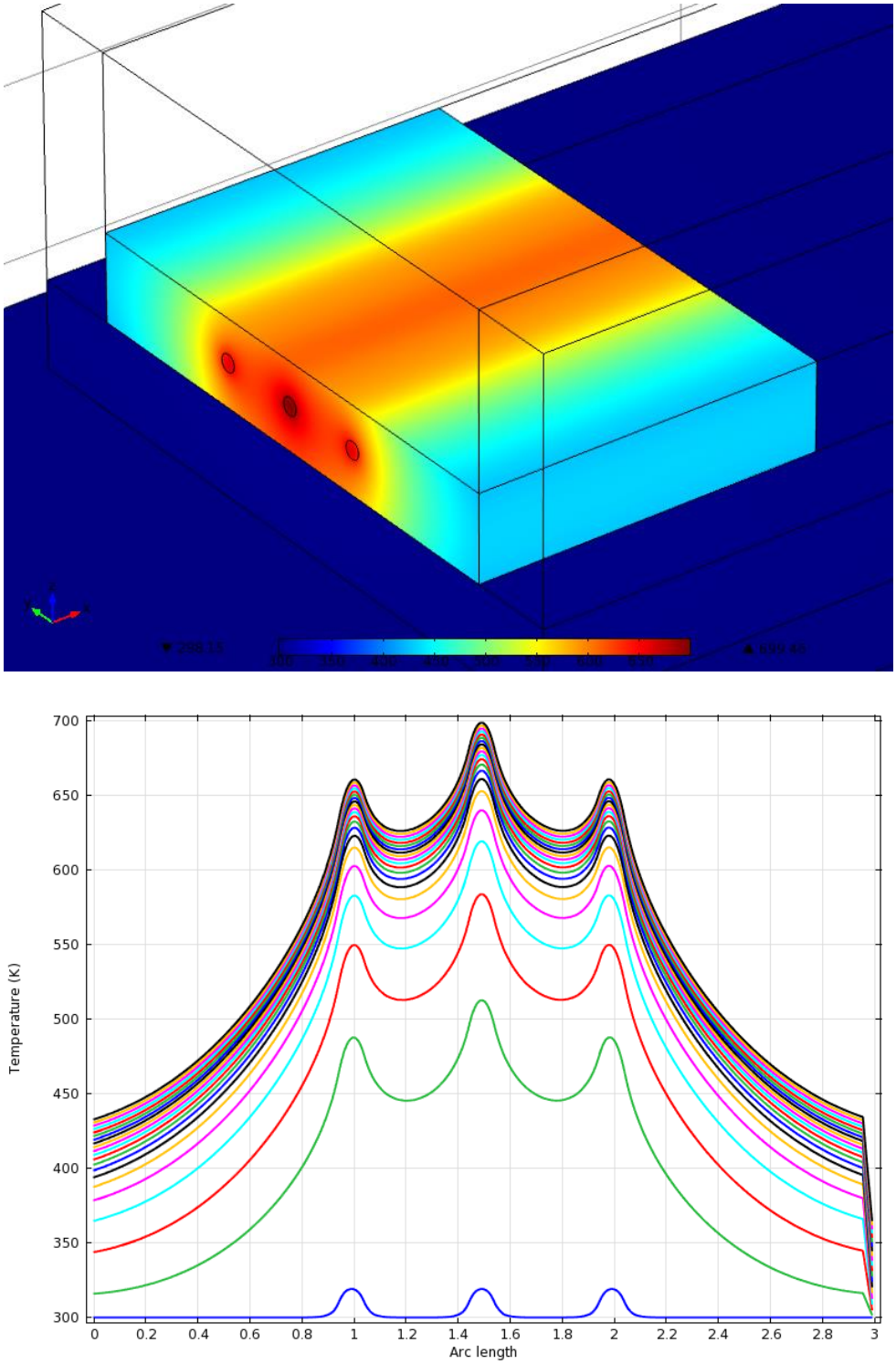

Figure 4.29. (d) Simulated thermal distribution in mGreen module (0.5-mm gap)

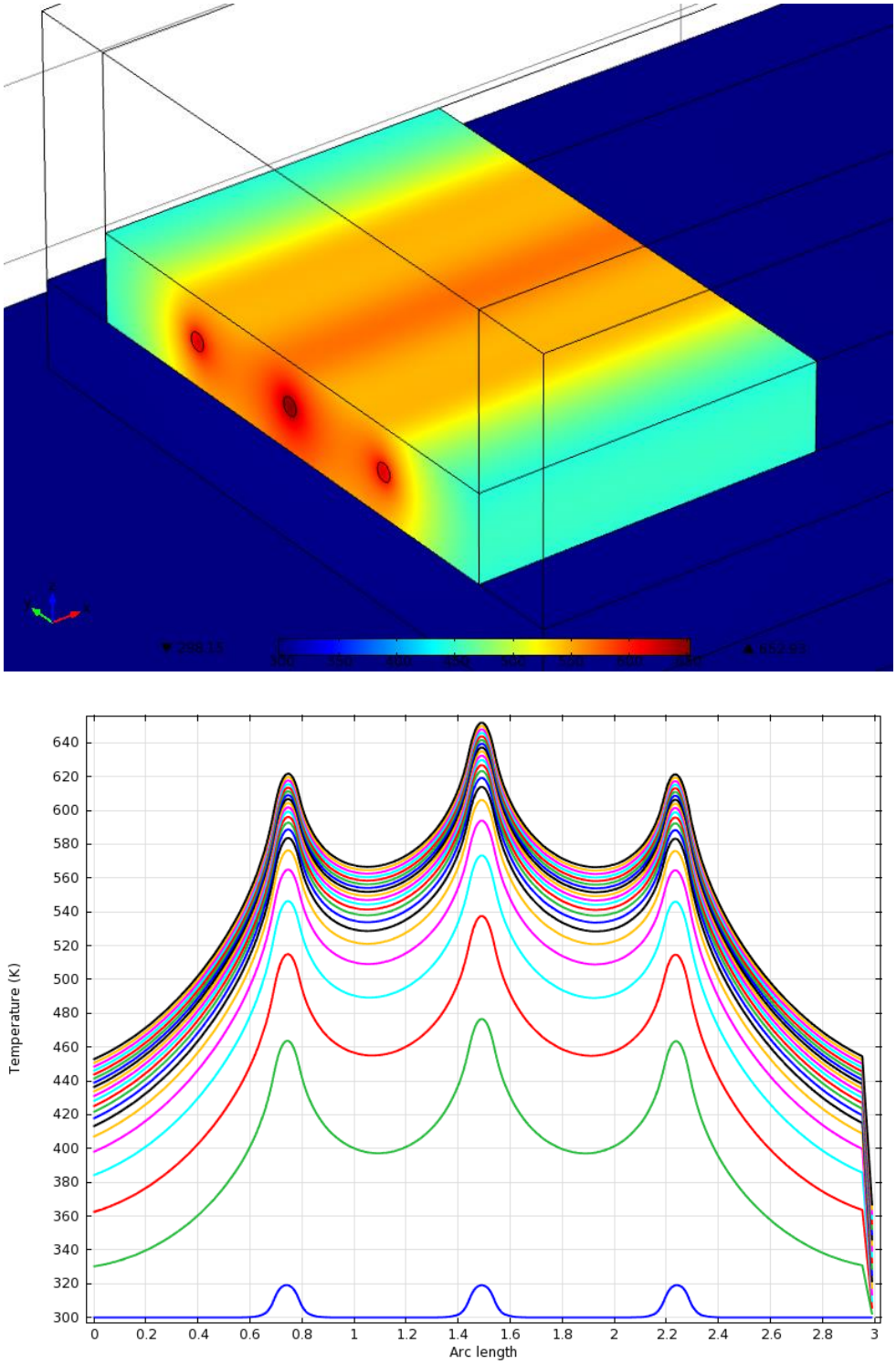

Figure 4.29. (e) Simulated thermal distribution in mGreen module (0.75-mm gap)

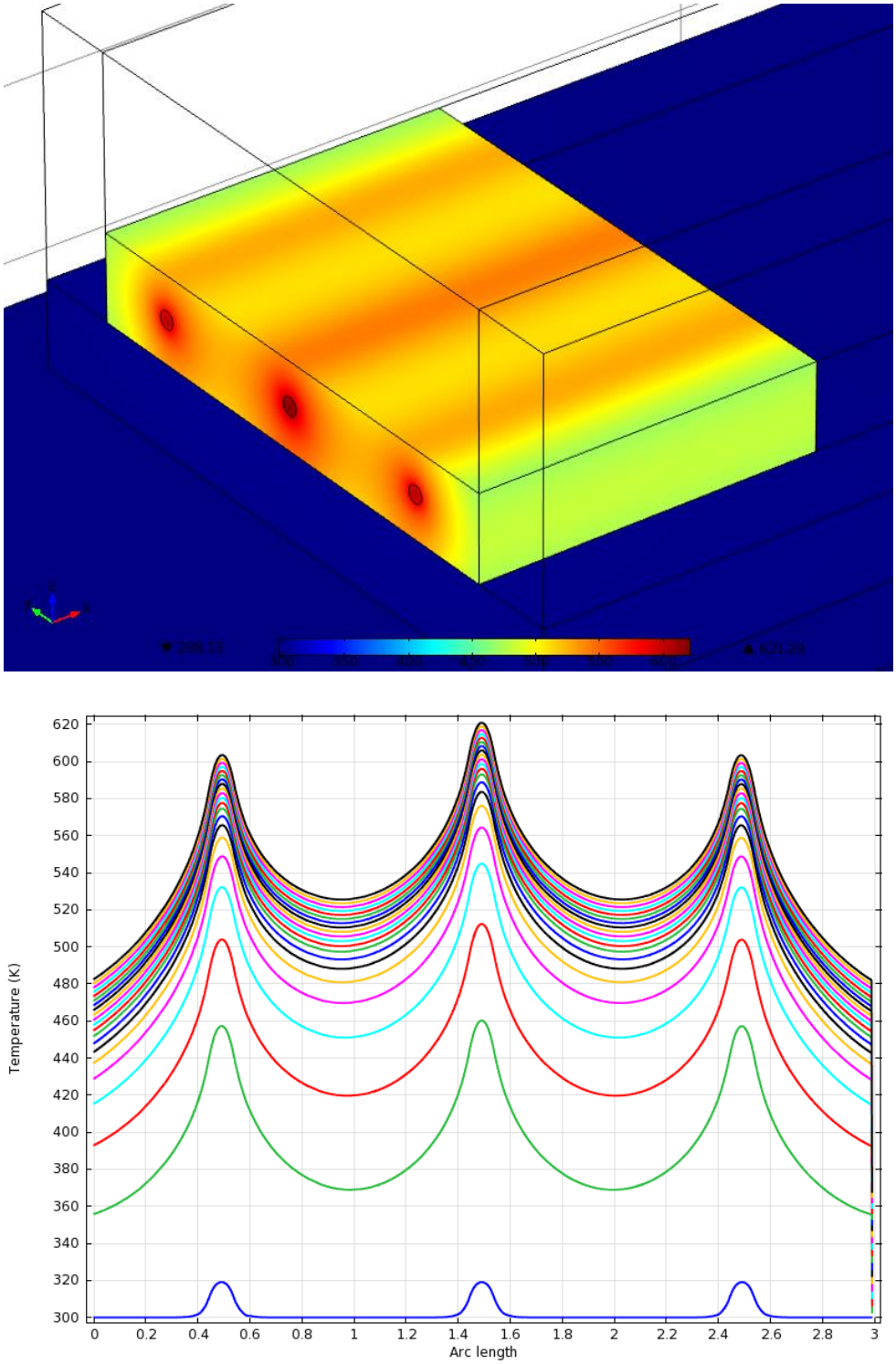

Figure 4.29. (f) Simulated thermal distribution in mGreen module (1-mm gap)

To experimental investigate this gap dependence, a setup of an mGreen module pumped by two fibers was designed as shown in Figure 4.30. Two fiber-coupled 2.5 W 808-nm is used as the pump source. The output fibers is mounted on a silicon substrate with two v-grooves. The gap between two v-grooves was set to different values.

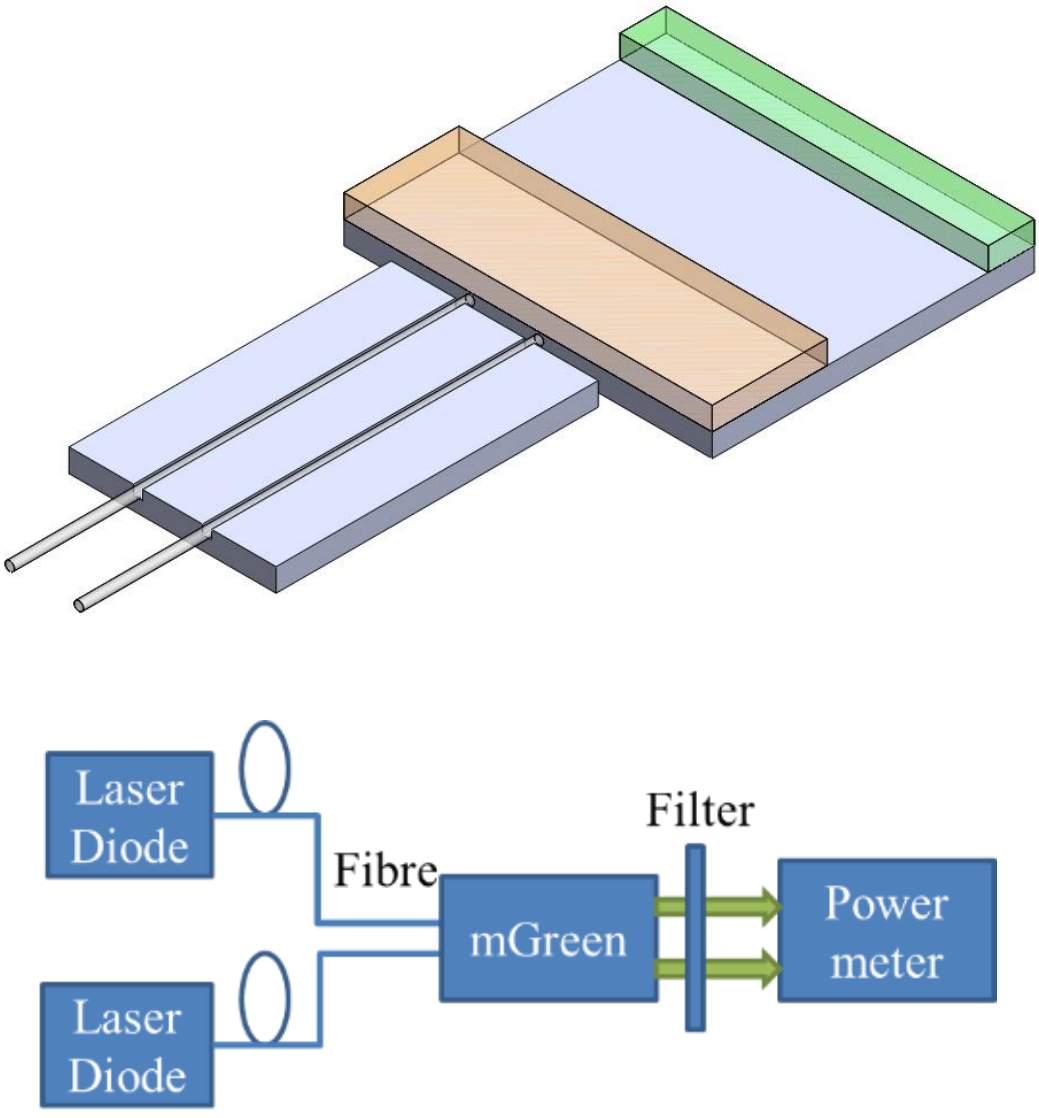

Figure 4.30. Experimental setup of array configuration.

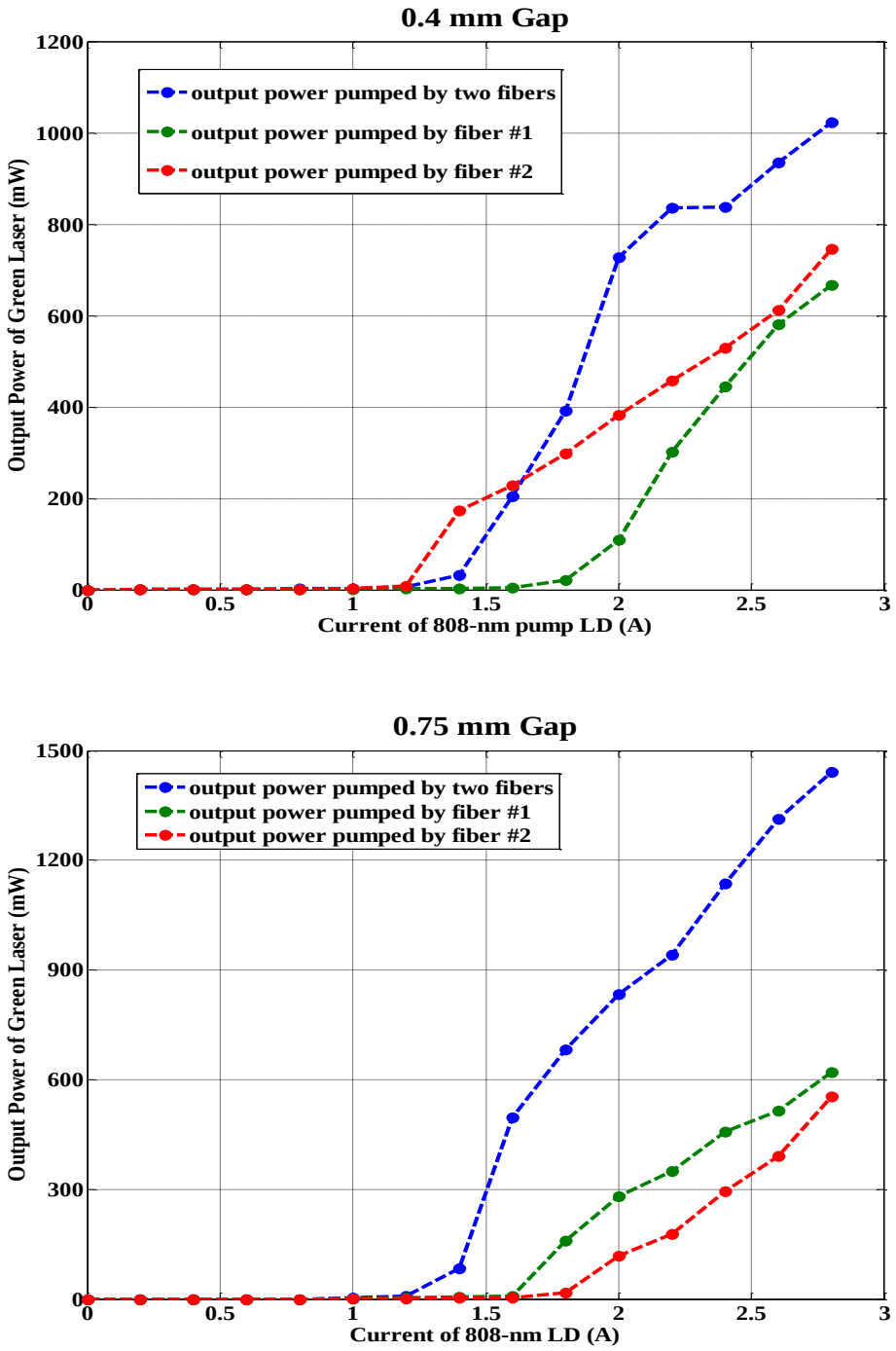

Figure 4.31. Measured green laser output with 0.4-mm and 0.75-mm gap between two pump beams.

Each fiber-coupled 808-nm LD was able to provide 2.4 W pump power at 2.8 A current. The mGreen module was mounted on a fan-cooled Peltier temperature controller. We experimented with 0.3 mm to 1 mm gap between two fibers and the green output performance of 0.4 mm gap and 0.75 mm gap are shown in Figure 4.31. We found that below 0.75 mm separation, only one green light beam was generated, which is agreed with the thermal simulation results presented above. When gap is less than 0.75 mm, the temperature distribution profile caused by each pump beam would merge and produce a strong thermal lens that brought two lasing modes together. While at 0.75 mm separation and above, two pump beams did not couple significantly each other, and two independent green laser beams were generated, as shown in Figure 4.32.

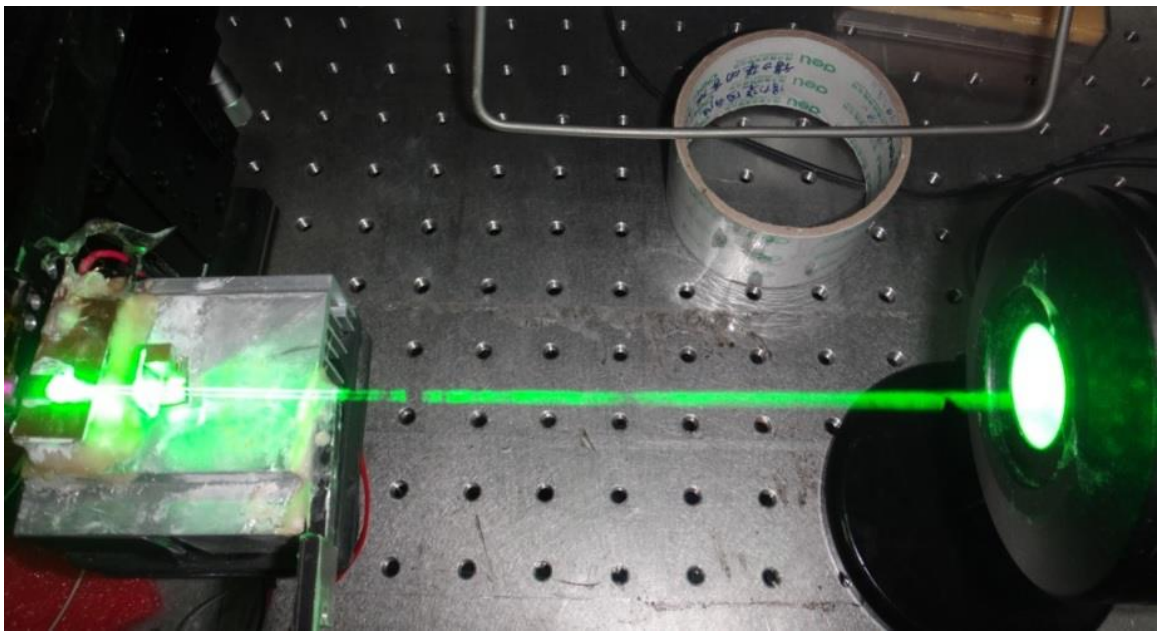

Figure 4.32. A photograph of two green beams from the mGreen module.

Near 1.5 W green laser output was obtained at 0.75 mm separation. The optical-to-optical conversion efficiency was 31.6%. The array output power was greater than the combination of output when each pump LD worked alone and the oscillation threshold was also lower than each single beam.

According to our study, the mGreen green laser module can be further scaled up by multiple pumps with 0.75 mm separation in between. The Nd:YVO_4/PPLN plane- parallel laser cavity can provide an output power density of approximately 1 W/mm . The green laser array provides a compact low cost solution, which is sufficient for most laser display applications.

CHAPTER 5

CONCLUSION

5.1 Summary of Accomplishments

The current thesis presents a study on solid state green lasers based on MgO:PPLN crystals. The achievements of this research are described in Chapters 2 – 4, and the main results are summarized below.

This thesis briefly reviews theories regarding nonlinear frequency conversion and solid state lasers. A numerical model has been built to simulate and optimize the intra-cavity frequency doubling configuration design. The thermal effect analysis has also been introduced.

The experimental studies have been conducted, starting from the single-pass SHG configuration. As the most straightforward method to generate green light by nonlinear crystals, efficient single-pass frequency doubling relies on two important factors: pumping power and mode field overlapping of the fundamental and SHG light. Two experimental schemes have been investigated: one uses a Q-switched fiber laser as the pump source and another is based on an APE MgO:PPLN ridge waveguide device. Using a novel all-fiber Q-switched Yb-doped fiber laser and a 15 mm long MgO:PPLN crystal, green laser with a peak power of 153 mW has been obtained at room temperature. The nonlinear conversion efficiency is about 3.1%/W/cm which agrees well with the theoretical value. The conversion efficiency will be higher if higher peak pump power can

be provided. On the other hand, over 120 mW green laser with 53.2% conversion efficiency has been achieved from a novel APE MgO:PPLN ridge waveguide device and an all-fiber linearly polarized Yb-doped fiber laser. It has been found that the conversion efficiency of the waveguide device saturates under higher pumping power, which is mainly due to the non-uniform heat generation over the long waveguide under high pump power density.

Our experiments show that the single-pass configuration is not very suitable for a practical compact green laser, especially from industrial point of view (i.e. cost, mass production, and stability). My research moves forward to the intra-cavity frequency doubling technique based on diode pumped solid state lasers. The alignment-free Nd:YVO_4/MgO:PPLN microchips have been first investigated for several hundred mW green output power applications. Nearly 300 mW green laser has been achieved at 1.5 W CW pump power with an optical-to-optical efficiency of 19.3%. Under the modulated operation mode, due to better thermal extraction, 540 mW peak green power has been obtained with 28% optical-to-optical efficiency. Since the microchip structure is limited to low green power levels applications due to the large heat dissipation of the optically bonded structure, in order to reach Watt level output green power, conversional intra-cavity frequency doubled DPSS lasers with discrete gain mediums and nonlinear crystals have been studied. Maximum 2.9 W green laser has been achieved with 9.8 W pump power from a plane-parallel cavity structure, which corresponds to an optical-to-optical efficiency of 29.6%. Higher green power can be expected by increasing pump power since no saturation is observed in the experiments. In addition, a novel monolithic

Nd:YVO_4/MgO:PPLN integrated module (namely mGreen module) which combines the advantages of the microchip and the separated plane-parallel cavity has been studied for Watt-level applications. Maximum 1.28 Watt green power is obtained with an optical-to-optical conversion efficiency of 29.1%. Through structure optimization, a conversion efficiency as high as 38.5% has been achieved. Power scaling based on this monolithic green laser module by employing the array concept has also been investigated. 1.44 Watt green power is achieved when mGreen module is pumped by two 2.4 Watt fiber-pigtailed 808-nm LDs. The influence of beam gap has been studied both theoretically and experimentally.

5.2 Suggestions for Future Work

Despite the achievements of this research, many things remain to be done to further improve the performance of solid state green lasers based on MgO:PPLN crystals.

On theoretical aspect, the thermal effect in intra-cavity frequency doubled DPSS lasers, especially in the mGreen monolithic module should be more carefully investigated. A more precise thermal-optical coupled model should be built for dynamic analysis of green solid state lasers.

On the experimental side, based on the preliminary results on the array structure, optimized pump LD array should be used to build a compact and high power multi beam green laser using mGreen module. Moreover, advanced QPM structure, such as

aperiodical PPLN, can be designed and used in intra-cavity frequency doubled DPSS lasers to improve the temperature tolerance.

Intra-cavity frequency doubling of a fiber laser is also worth to study. Compared with solid state lasers, fiber lasers have many advantages in terms of power capability, stability, reliability, beam quality, and cost.

References

1. H. Okumura, T. Uchida, S. Kaneko, Y. Shimodaira, H. Uchike, R. Hattori, Y. Nakanishi, E. Yamazaki, M. Nakamoto, "40-years history of display technologies and the vision for future displays," IEICE Transactions on Electronics, v J92-C, n 8, p 433-53, Aug. 2009.

2. D. Bayon, "The science of Retina displays," PC Pro, n 216, p 44-7, Oct. 2012.

3. C. E. Baker, "Laser display technology," IEEE Spectrum, v 5, n 12, p 39-50, Dec. 1968.

4. K. V. Chellappan, E. Erden, H. Urey, "Laser-based displays: a review," Applied Optics, v 49, n 25, p F79-F98, Sept. 2010.

5. Broadbent, D. Arthur, "A critical review of the development of the CIE1931 RGB color-matching functions," Color Research and Application, v 29, n 4, p 267-272, August 2004.

6. P. Janssens, K. Malfait, "Future prospects of high-end laser projectors," Proceedings of the SPIE - The International Society for Optical Engineering, v 7232, p 72320Y (12 pp.), 2009.

7. Mr. Matthew, S. Brennesholtz, H. S. Edward, "Projection Displays," Second Edition, John Wiley & Sons, Ltd., Sept. 2008.

8. E. Kato, H. Noguchi, M. Nagai, H. Okuyama, S. Kijima, and A. Ishibashi, "Significant progress in II-VI blue-green laser diode lifetime," Electron. Lett., vol. 34, no. 3, 1998.

9. M. Jansen,B.D.Cantos, G. P.Carey, R.Dato,G.Giaretta, S.Hallstein, W. R. Hitchens, D. Lee, A.Mooradian, R. F. Nabiev, G. Niven, A. V. Shchegrov, A. Umbrasas, and J. P. Watson, "Visible laser and laser array sources for projection displays," in Proc. SPIE, 2006, vol. 6135, p. 61350T.

10. A. Agnesi, A. Guandalini, G. Reali, "Laser diodes and diode-pumped solid-state laser systems: Advantages, limits and application fields," Proceedings of SPIE, v 5131, p 9-14, 2002.

11. Y. Suematsu and K. Iga, "Semiconductor lasers in photonics," J. Lightwave Technol. 26, 1132–1144 (2008).

12. M. Ikeda, Y. Mori, H. Sato, K. Kaneko, and N. Watanabe, "Room temperature continuous wave operation of an AlGaInP double heterostructure laser grown by atmospheric pressure metal–organic chemical vapor deposition," Appl. Phys. Lett., vol. 47, no. 10, pp. 1027–1028, Nov. 1985.

13. B. Qiu, O.P. Kowalski, S. McDougall, B. Schmidt, and J.H. Marsh, "High-Performance Visible Semiconductor Lasers Operating at 630 nm," IEEE Photonics Journal, vol.2, no.4, pp.563-570, Aug. 2010.

14. N. Shimada, K. Shibata, Y. Hanamaki, T. Hamaguchi and T. Yagi, "12W CW operation of 640nm-band laser diode array," Proc. of SPIE, 6876, 68760L, 2008.

15. S. Nakamura, "InGaN-based blue laser diodes," IEEE J. Sel. Topics Quantum Electron., vol. 3, no. 3, pp. 712–718, Jun. 1997.

16. R. N. Hall, G. E. Fenner, J. D. Kingsley, T. J. Soltys, and R. O. Carlson, "Coherent light emission from GaAs junctions," Phys. Rev. Lett. 9, 366–368 (1962).

17. M. I. Nathan, W. P. Dumke, G. Burns, F. H. Dill, Jr., and G. Lasher, "Stimulated emission of radiation from GaAs p-n junctions," Appl. Phys. Lett. 1, 62–64 (1962).

18. T.Kozaki, H.Matsumura, Y. Sugimoto, S.-I. Nagahama, and T. Mukai, "High-power and wide wavelength range GaN-based laser diodes," in Proc. SPIE, vol. 6133, pp. 613306-1–613306-12.

19. S. Nakamura, N. Iwasa, M. Senoh and T. Mukai, "Hole Compensation Mechanism of P-Type GaN Films," Jpn. J. Appl. Phys, vol. 31, pp. 1258-1266, 1992.

20. T. Miyoshi, T. Kozaki, T. Yanamoto, S. Nagahama, T. Mukai, "GaN-based 1-W continuous-wave blue-laser diodes," SID 2008 Digest, 63.3, pp.966-968, 2008.

21. D. Sizov, R. Bhat, C. Zah, "Gallium Indium Nitride-Based Green Lasers," Journal of Lightwave Technology, Vol. 30, Issue 5, pp. 679-699 (2012).

22. T. Miyoshi, S. Masui, T. Okada, T. Yanamoto, T. Kozaki, S.-I. Nagahama, and T. Mukai, "InGaN-based 518 and 488 nm laser diodes on c-plane GaN substrate," Phys. Stat. Sol. (a), vol. 207, pp. 1389–1392, 2010.

23. T. Miyoshi, S. Masui, T. Okada, T. Yanamoto, T. Kozaki, S.-I. Nagahama, and T. Mukai, "510–515 nm InGaN-based green laser diodes on c-plane GaN substrate," Appl. Phys. Exp., vol. 2, p. 062201, 2009.

24. D. Queren, A. Avramescu, G. Bruderl, A. Breidenassel, M. Schillgalies, S. Lutgen, and U. Strauss, "500 nm electrically driven InGaN based laser diodes," Appl. Phys. Lett., vol. 94, p. 081119, 2009.

25. S. Lutgen, A. Avramescu, T. Lermer, M. Schillgalies, D. Queren, J. Muller, D. Dini, A. Breidenassel, and U. Strauss, “Progress of blue and green InGaN laser diodes,” in Proc. SPIE, 2010, vol. 7616, p. 76160G.

26. A. Avramescu, T. Lermer, J. Müller, C. Eichler, G. Bruederl, M. Sabathil, S. Lutgen, and U. Strauss, “True green laser diodes at 524 nm With 50 mW continuous wave output power on -plane GaN,” Appl. Phys. Exp., vol. 3, p. 061003, 2010.

27. Y. Enya, Y. Yoshizumi, T. Kyono, K. Akita, M. Ueno, M. Adachi, T. Sumitomo, S. Tokuyama, T. Ikegami, K. Koji, and T. Nakamura, “531 nm green lasing of InGaN based laser diodes on semi-polar {20-21} free-standing GaN substrates,” Appl. Phys. Exp., vol. 2, p. 082101, 2009.

28. M. Adachi, Y. Yoshizumi, Y. Enya, T. Kyono, T. Sumitomo, S. Tokuyama, S. Takagi, K. Sumiyoshi, N. Saga, T. Ikegami, M. Ueno, K. Katayama, and T. Nakamura, “Low threshold current density InGaN based 520–530 nm green laser diodes on semi-polar (20–21), “free-standing GaN substrates”,” Appl. Phys. Exp., vol. 3, p. 121001, 2010.

29. M. Ueno, Y. Yoshizumi, Y. Enya, T. Kyono, M. Adachi, S. Takagi, S. Tokuyama, T. Sumitomo, K. Sumiyoshi, N. Saga, T. Ikegami, K. Katayama, and T. Nakamura, “InGaN-based true green laser diodes on novel semi-polar GaN substrates,” J. Cryst. Growth, vol. 315, pp. 258–262, 2011.

30. D. S. Sizov, R. Bhat, J. Napierala, J. Xi, D. E. Allen, C. S. Gallinat, and C. Zah, “Lasing and optical gain around 500 nm from optically pumped lasers grown on c-plane GaN substrates,” Opt. Lett., vol. 34, pp. 328–330, 2009.

31. J. W. Raring, M. C. Schmidt, C. Poblenz, B. Li, Y.-C. Chang, M. J. Mondry, Y.-D. Lin, M. R. Krames, R. Craig, J. S. Speck, S. P. DenBaars, and S. Nakamura, “High-performance blue and green laser diodes based on nonpolar/semipolar bulk GaN substrates,” in Proc SPIE, 2011, vol. 7939, pp. 79390Y-1–79390Y-7.

32. Y.-D. Lin, S. Yamamoto, C.-Y. Huang, C.-L. Hsiung, F. Wu, K. Fujito, H. Ohta, J. S. Speck, S. P. DenBaars, and S. Nakamura, “High quality InGaN/AlGaN multiple quantum wells for semipolar InGaN green laser diodes,” Appl. Phys. Exp., vol. 3, p. 082001, 2010.

33. P.A. Franken A. E. Hill, C. W. Peters, and G. Weinreich, “Generation of optical harmonics,” Phys. Rev. Lett., vol.7, p. 118 Aug. 1961.

34. R. G. Smith, “Theory of intracavity optical second harmonic generation,” IEEE J. Quantum Electron., vol.6, no.4, pp. 215-130, Apr. 1970.

35. A.Jechow, R. Menzel, K. Paschke, and G. Erbert, “Blue-green light generation using high brilliance edge emitting diode lasers,” Laser Photon. Rev., vol. 4, no. 5, pp. 633–655, 2010.

36. G. D. Miller, R. G. Batchko, W. M. Tulloch, D. R. Weise, M. M. Fejer, and R. L. Byer, "42%-efficient single-pass cw second-harmonic generation in periodically poled lithium niobate," Opt. Lett. 22, 1834-1836 (1997).

37. F. J. Kontur, I. Dajani, Yalin Lu, and R. J. Knize, "Frequency-doubling of a CW fiber laser using PPKTP, PPMgSLT, and PPMgLN," Opt. Express 15, 12882-12889 (2007).

38. G. K. Samanta, S. C. Kumar, K. Devi, and M. Ebrahim-Zadeh, "55%-Efficient, 13-W, Single-Pass SHG of a CW Yb-Fiber Laser in a Double-Crystal Scheme," in Conference on Lasers and Electro-Optics, OSA Technical Digest (CD) (Optical Society of America, 2010), paper CWQ7.

39. T. P. Pearsall, S. Chiang, and R. V. Schmidt, “Study of titanium diffusion in lithium-niobate low-loss optical waveguides by x-ray photoelectron spectroscopy,” J. Appl. Phys. vol.47, 4794-4797 (1976).

40. J. L. Jackel, C. E. Rice, and J. J. Veselka, “Proton-exchange for high-index waveguides in LiNbO3,” Appl. Phys. Lett. vol.41, 607-608 (1982).

41. R. V. Schmidt and I. P. Kaminow, “Metal-diffused optical waveguides in $LiNbO_3$,” Appl. Phys. Lett. vol.25, 458-460 (1974).

42. W. M. Young, M. M. Fejer, M. J. F. Digonnet, A. F. Marshall, and R. S. Feigelson, "Fabrication, Characterization, and Index Profile Modelling of High Damage Resistance Zn-diffused Waveguides in Congruent and MgO:Lithium Niobate", J. Lightwave. Technol. 10, 1238-1246 (1992).

43. N. Hamelin and Y. T. Chow, “Guided-type second harmonic generation in ion implanted MgO:$LiNbO_3$,” J. Mod. Opt. vol.45, 2125 (1998).

44. K. Sakai, Y. Koyata, S. Itakura, and Y. Hirano, "High-Power, Highly Efficient Second-Harmonic Generation in a Periodically Poled MgO:$LiNbO_3$ Planar Waveguide," J. Lightwave Technol. 27, 590-596 (2009).

45. H. Hu et al., “Etching of Lithium Niobate: From Ridge Waveguides to Photonic Crystal Structures,” Proc. of ECIO’08, pp.75-78, 2008.

46. H. Hu, R. Ricken, W. Sohler, and R. B. We hrspohn, “Lithium Niobate Ridge Waveguides Fabricated by Wet Etching,” Photonics Technology Letters Vol.19, No.6 (2007).

47. H. Hu et al., “Plasma etching of proton-exchanged lithium niobate”, J. Vac. Sci. Technol. A, vol. 24, pp. 1012–1015, (2006).

48. H. K. Nguyen, M. H. Hu, Y. Li, K. Song, N. J. Visovsky, S. Coleman, and C. Zah, “304 mW green light emission by frequency doubling of a high-power 1060-nm DBR semiconductor laser diode,” in Proc. SPIE, 2008, vol. 6890, pp. 68900I1–68900I6.

49. V. Bhatia, S. J. Gregorski, D. Pikula, S. C. Chaparala, D. A. S. Loeber, J. Gollier, Y. Ozeki, Y. Hata, K. Shibatani, F. Nagai, Y. Nakabayashi, N. Mitsugi, and S. Nakano, “63.2: Efficient and compact green laser incorporating adaptive optics for wide operating temperature range,” in SID Symposium Digest of Technical Papers (Society for Information Display, 2008), Vol. 39, pp. 962–965.

50. Y. Hirano, T. Sasagawa, T. Yanagisawa, S. Yamamoto, A. Nakamura, T. Yagi, and H. Sugiura, "Solid-State SHG Green Laser for Laser TV," in Conference on Lasers and Electro-Optics/International Quantum Electronics Conference, OSA Technical Digest (CD) (Optical Society of America, 2009), paper PThA3.

51. Panasonic, "Announcing the release of “ the 1W green laser unit smallest in the world” " http://panasonic.net/id/news/20120925_1.html.

52. H. Soda, K.-I. Iga, C. Kitahara, and Y. Suematsu, “GaInAsP/InP surface emitting injection lasers,” Jpn. J. Appl. Phys. 18, 2329–2330 (1979).

53. M. Jansen ; G. P. Carey ; R. Carico ; R. Dato ; A. M. Earman ; M. J. Finander ; G. Giaretta ; S. Hallstein ; H. Hofler ; C. P. Kocot ; S. Lim ; J. Krueger ; A. Mooradian ; G. Niven ; Y. Okuno ; F. G. Patterson ; A. Tandon ; A. Umbrasas; "Visible laser sources for projection displays," Proc. SPIE 6489, Projection Displays XII, 648908 (February 06, 2007).

54. Greg Niven, Arm Mooradin, "Trends in laser light sources for projection displays," 13th International Display Workshops (IDW '06) Otsu, Japan December 6-8, 2006.

55. S. Lutgen, T. Albrecht, P. Brick,W. Reill, J. Luft, andW. Späth, "8W high-efficiency continuous-wave semiconductor disk laser at 1000 nm," Appl. Phys. Lett. 82, 3620–3622 (2003).

56. L.E. Hunziker, C. Ihli, D.S. Steingrube, "Miniaturization and Power Scaling of Fundamental Mode Optically Pumped Semiconductor Lasers," IEEE Selected Top. in Quantum Electron., vol.13, no.3, pp.610-618, May-june 2007.

57. J. Lee , S. Lee , T. Kim and Y. Park "7 W high-efficiency continuous-wave green light generation by intracavity frequency doubling of an end-pumped vertical external-cavity surface emitting semiconductor laser", Appl. Phys. Lett., vol. 89, pp. 241107 2006.

58. M. Fallahi, F. Li Y. Kaneda, C. Hessenius, J. Hader, Li H. J.V. Moloney, B. Kunert, W. Stolz, S.W. Koch, J. Murray, and R. Bedford, "5-W Yellow Laser by Intracavity Frequency Doubling of High-Power Vertical-External-Cavity Surface-Emitting Laser," IEEE Photon. Technol. Lett., vol.20, no.20, pp.1700-1702, Oct.15, 2008.

59. U. Steegmuller, M. Kuhnelt, H. Unold, T. Schwarz, R. Schulz, S. Illek, I. Pietzonka, H. Lindberg, M. Schmitt, and U. Strauss, "Green laser modules to fit laser projection out of your pocket," Proc. SPIE 6871, 687117 (2008).

60. Coherent, Genesis Lasers, http://www.coherent.com/products/?1679/Genesis-Lasers.

61. A. Masters, C. Seaton, "Laser-based displays will deliver superior images," Laser Focus World, 42, S9–S11.

62. W.P. Risk, T. R.Gosnell, and A. V. Nurmikko, "Compact blue-green lasers," Cambridge University Press, 2003.

63. J. P. Remeika and A. A. Ballman, "Flux Growth, CZOCHRALSKI Growth, and Hydrothermal Synthesis of Lithium Metagallate Single Crystals," Appl. Phys. Lett. 5, 180 (1964).

64. L. Arizmendi, "Photonic applications of lithium niobate crystals," Physica Status Solidi C, vol. 2, p a253-83, 2004.

65. K.K. Wong, ed., Properties of Lithium Niobate, INSPEC, Inc., 2002.

66. E. Kaldis, ed., "Current topics in materials science," vol.1, 1978.

67. T. Y. Fan, "Diode pumped solid state lasers," The Lincoln Lab. J. 3(3):413-425, 1990.

68. G. Huber, C. Kränkel, and K. Petermann, "Solid-state lasers: status and future", J. Opt. Soc. Am. B 27 (11), B93 (2010)

69. W. Koechner, "Solid-State Laser Engineering", 1st edition, Springer Verlag.

70. G. H. Dieke and H. M. Crosswhite, “The spectra of the doubly and triply ionized rare earth”, Appl. Opt. 2 (7), 675 (1963)

71. D. Vivien, "Recent advances in solid-state laser materials: An introdcution" Annales de Chimie Science des Materiaux, 28 (6) 1-3 (November-December 2003).

72. L. Gao, H. Tan, "Compact 600 mW blue laser with a composite Nd:YAG," Optics & Laser Technology, 35, 575 - 578, (2003)

73. C. Li, Y. Cao, “Review on the Nd-doped laser crystals,” Laser and Infrared, v 25, n 6, p 16-20, Dec 1995.

74. A. J. Kenyon, “Recent developments in rare-earth doped materials for optoelectronics”, Prog. Quantum Electron. 26, 225 (2002).

75. N. Hodgson et al., “High power TEM00 mode operation of diode-pumped solid-state lasers”, Proc. SPIE 3611, 119 (1999).

76. M. J. F. Digonnet, Rare-Earth-Doped Fiber Lasers and Amplifiers, 2nd edn., CRC Press, Boca Raton, FL (2001)

77. M. Tsunekane, N. Taguchi, T. Kasamatsu, H. Inaba, “Analytical and experimental studies on the characteristics of composite solid-state laser rods in diode-end-pumped geometry,” IEEE Journal on Selected Topics in Quantum Electronics, v 3, n 1, p 9-18, Feb 1997.

78. N. Hodgson and H. Weber, Laser Resonators and Beam Propagation, 2nd edn., Springer, Berlin (2005).

79. J. Sotor, G. Dudzk, A. Antonczak, K. Abrmski, “Single-longitudinal mode, monolithic, green solid-state laser,” Applied Physics B: Lasers and Optics, v 103, n 1, p 67-74, April 2011.

80. M. G. Galushkin, V. A. Karasev, K. V. Mitin, “Nonlinear thermal lens in an active medium of the single-mode solid-state laser,” Bulletin of the Russian Academy of Sciences. Physics, v 63, n 10, p 1492-4, 1999.

81. A. E. Siegman, Lasers, University Science Books, Mill Valley, CA (1986).

82. D. Kouznetsov, J. F. Bisson, K. Takaichi, K. Ueda, “High-power single-mode solid-state laser with a short, wide unstable cavity,” Journal of the Optical Society of America B: Optical Physics, v 22, n 8, p 1605-1619, August 2005.

83. S. De Silvestri, V. Magni, O. Svelto, P. Laporta, “Optimized cavities for single-transverse-mode solid state lasers,” CONFERENCE ON LASERS AND ELECTRO-0PTICS, p 224, 1989.

84. R. Weber, B. Neuenschwander, H. P. Weber, "Thermal effects in solid-state laser materials," Opt. Mater. 11 (1999) 245-254.

85. Y. Zheng, L. Zhang, L. Jia, J. Kang, “Thermal effect of Nd:YVO_4 crystal by laser diode end-pumped,” Proceedings of the SPIE, v 7156, p 71562F (8 pp.), 2008.

86. M. E. Innocenzi, H. T. Yura, C. L. Fincher, R. A. Fields, "Thermal modeling of continouse-wave end-pumped solid-state lasers," Appl. Phys. Lett. 9, 1831-1833 (1990).

87. R. W. Boyd, “Nonlinear Optics, Academic Press”, 2nd ed, CRC Press, Boca Raton, FL (2003).

88. R. L. Sutherland, “Handbook of Nonlinear Optics”, 2nd ed, Marcel Dekker, New York (2003).

89. J.A. Armstrong, N. Bloembergen, J. Ducuing, P.S. Pershan,“Interactions between light waves in a nonlinear dielectric,” Phys. Rev., vol. 127, p 1918-1939, 1962.

90. R.L. Byer, “Quasi-phasematched nonlinear interactions and devices,” Journal of Nonlinear Optical Physics and Materials, vol. 6, p 549-92, 1997.

91. D.S. Hum, M.M. Fejer, “Quasi-phasematching,” Comptes Rendus, Physique, vol. 8, p 180-98, 2007.

92. F. J. Kontur, I. Dajani, Y. Lu, and R. J. Knize, “Frequency-doubling of a CW fiber laser using PPKTP, PPMgSLT, and PPMgLN”, Optics Express, Vol. 15, No. 20, p 12882, 2007.

93. H. Furuya, A. Morikawa, K. Mizuuchi, and K. Yamamoto, “High-beam-quality continous wave 3 W green-light generation in bulk periodically poled MgO: $LiNbO_3$”, Japanese Journal of Applied Physics, Vol. 45, No.8 B, p 6704, 2006.

94. S. V. Tovstonog, S. Kurimura, and K. Kitamura, “High power continuous-wave green light generation by quasiphase matching in Mg stoichiometric lithium niobate”, Applied Physics, Vol. 90, No.5, p 51115-1-3, 2007.

95. M. Leigh, W. Shi, J. Zong, J. Wang, and S. Jiang, “Compact, single-frequency all fiber Q-switched laser at 1 μm”, Optics Letters, Vol. 32, No. 8, p. 897, 2007.

96. Y. Wang and C. Q. Xu, “Modeling and optimization of Q-switched double-clad fiber lasers”, Appl. Opt. Vol. 45 p. 2058, 2006.

97. Y. Kaneda, Y. Hu, C. Spiegelberg, J. Geng, and S. Jiang, “Single-frequency, all fiber Q-switched laser at 1550 nm”, OSA TOPS Vol. 94, Advanced Solid-State Photonics, p.126, 2004.

98. J. Y. Huang, H. C. Liang, K. W. Su, and Y. F. Chen, “High power passively Q-switched ytterbium fiber laser with Cr4+: YAG as saturable absorber”, Optics Express Vol. 15, No.2, p. 473, 2007.

99. V. V. Dvoyrin, V. M. Mashinsky, and E. M. Dianov, “Yb-Bi pulsed fiber lasers”, Optics Letters, Vol. 32, No.5, p.451, 2007.

100. A. A. Fotiadi, A. S. Kurkov, and I. M. Razdobreev, “Dynamics of all Fiber Self-Q-switched Ytterbium/Samarium Laser”, in Laser and Electro-Optics / Quantum Electronics and Laser Science Conference, Baltimore, Maryland, USA, May 6-11, 2007, Paper CMC4.

101. X. J. Gu and Y. Liu, “The efficient light coupling in a twin-core fiber waveguide,” IEEE Photon. Technol. Lett. 17, 2125-2127 (2005).

102. B. Wu and P. L. Chu, “Fast optical switching in Sm3+-doped fiber”, IEEE, Photon. Technol. Lett., 8, (2), pp230-232, 1996.

103. P. G. Suchoski, T. K. Findakly, and F. J. Leonberger, “Stable low-loss proton-exchanged $LiNbO_3$ waveguide devices with no electro-optic degradation”, Opt. Lett. 13, 1050 (1988).

104. K. Mizuuchi, T. Sugita, K. Yamamoto, T. Kawaguchi, T. Yoshino, and M. Imaeda, “Efficient 340-nm light generation by a ridge-type waveguide in a first-order periodically poled MgO:LiNbO3”, Opt. Lett. 28, 1344 (2003)

105. Tadanaga, T. Yanagawa, Y. Nishida, H. Miyazawa, K. Magari, M. Asobe, and H. Suzuki, "Efficient 3-μm difference frequency generation using direct-bonded quasi-phase-matched LiNbO3 ridge waveguides", Appl. Phys. Lett. 88, 061101 (2006).

106. D. T. Walton et. al., "High Power, linearly Polarized Yb-doped Fiber Laser", in OSA Tops Vol. 94, "Advanced Solid-State Photonics", edited by Gregory J. Quarles, pp 104 -107 (2004).

107. Chi-Hung Liu, et.al. "High-power, single polarization, transverse mode fiber laser with all fiber cavity and fiber grating stabilized spectrum", Opt. Lett. 31, 17 (2006).

108. A. Shirakawa, et.al. "Characteristic of linearly polarized Yb doped fiber laser in an all fiber configuration", IEEE Photon. Technol. Lett., 19, 1664 (2007).

109. V.M. Paramonov, et. al. "Single polarization cladding-pumped Yb doped fiber laser", Laser Phys. Lett. 4, 740 (2007).

110. D.Xue, A.R. El-Damak and X.Gu, "All-fiber single polarized Yb-doped fiber laser with a high extinction ratio", Opt. Comm. 283, 1059-1061 (2010).

111. J. J. Zayhowski, "Microchip Lasers," Lincoln Laboratory Journal, v 3, n 3, p 427-46, Fall 1990.

112. C. Jung, B.-A. Yu, I.-S. Kim, Y. L. Lee, N. E. Yu, and D.-K. Ko, "A linearly-polarized Nd:YVO_4/KTP microchip green laser," Opt. Express 17(22), 19611–19616, (2009).

113. B. –A. Yu, C. Jung, N. E. Yu, Y. L. Lee, I. S. Kim, D. –K. Ko, "Small-packaged temperature-controlled Nd:YVO_4/KTP microchip green laser," 2009 Conference on

Lasers & Electro Optics & The Pacific Rim Conference on Lasers and Electro-Optics (CLEO/PACIFIC RIM), p 2 pp., 2009.

114. Yang Lu, Qingyang Xu, Yi Gan, and Changqing Xu, "Field-Sequential Operation of Laser Diode Pumped Nd :YVO_4/PPMgLN Microchip Green Laser," IEEE Photon. Electron. Lett., vol. 22, no. 13, pp. 990-993 ,July 2010.

115. Yang Lu, Qingyang Xu, Yi Gan, Changqing Xu, "Over 500 mW Laser-Diode Pumped Green Laser Using Optical Contact Nd:YVO_4/Periodically Poled MgO:LiNbO3 Crystal," CLEO/QELS 2010, JTuD110, 2010.

116. T. Yokoyama, K. Mizuuchi, K. Nakayama, A. Kurozuka, T. Sugita, A. Morikawa, K. Yamamoto, "Compact intracavity green light source with wide operation temperature range using periodically poled Mg:$LiNbO_3$," Japanese Journal of Applied Physics, v 47, n 8, pt.2, p 6787-9, Aug. 2008.

117. S. Chu, Y. Zhang, B. Wang, Y. Bi, "High-Efficiency Intracavity Continuous-Wave Green-Light Generation by Quasiphase Matching in a Bulk Periodically Poled MgO:$LiNbO_3$ Crystal," Advances in OptoElectronics, p 151487 (4 pp.), 2008.

118. C. Xu, Y. Gan, J. Sun, "MgO:PPLN frequency doubling optical chips for green light generation: From lab research to mass production," Proceedings of SPIE, v 8280, 2012, Advances in Display Technologies II.